CHARGE STATES OF LOW ENERGY IO...

FROM THE SUN

by

Richard Kevin Sciambi

Technical Report No. 76-092
Physics Publication 76-176

December 1975

UNIVERSITY OF MARYLAND
DEPARTMENT OF PHYSICS AND ASTRONOMY
COLLEGE PARK, MARYLAND

CHARGE STATES OF LOW ENERGY IONS FROM THE SUN

by

Richard Kevin Sciambi

Technical Report No.

Physics Paper

December 1975

CHARGE STATES OF LOW ENERGY IONS FROM THE SUN

by

Richard Kevin Sciambi

Dissertation submitted to the Faculty of the Graduate School
of the University of Maryland in partial fulfillment
of the requirements for the degree of
Doctor of Philosophy
1975

ABSTRACT

Title of Dissertation: Charge States of Low Energy Ions from the Sun

Richard Kevin Sciambi, Doctor of Philosophy, 1975

Dissertation directed by: Dr. George Gloeckler
Associate Professor, Department of Physics and Astronomy

Measurements of the ionization states and energy spectra of carbon, oxygen, and (in one event) iron accelerated in ten solar flare particle events are reported, for energies between 15 keV per nucleon and 600 keV per nucleon. These observations were made using the University of Maryland Electrostatic Energy-Charge Analyzer aboard the IMP-8 earth-orbiting spacecraft. The ionization states are found to be remarkably constant from flare to flare, despite great variations in other event parameters (such as He/[C+N+O] abundance ratio). The mean ionization state for carbon is 5.7, for oxygen 6.2, and for iron 11.7, values which are similar to the respective ionization states in the solar wind. The time profile of the He/[C+N+O] ratio is examined, and it is found that the ratio is small early in the event, and increases with time. The energy spectra of the medium ions show a flattening below 100 keV per nucleon, which is highly correlated with event size as measured by the "event averaged" flux of 130-220 keV protons.

The atomic charge states are shown to be consistent with charge equilibrium established with an electron gas at a temperature of

1.5×10^6 °K - the temperature of the quiet corona. In order to reconcile the observed ionization states with conditions currently believed to prevail at the particle acceleration site, it is shown that some form of particle trapping in regions of quiet coronal temperatures is required after acceleration. The effect of ionization energy loss on the particle spectra during this trapping is discussed, and it is found that a spectral "kink" is expected. It is demonstrated that the observed spectral flattening is consistent with adiabatic deceleration of such "kinked" spectra. The required value of the interplanetary diffusion coefficient is computed, and is shown to be consistent with the observations. Finally, it is shown that both the time profile of the He/(CNO) abundance ratio and its variation from event to event may be explained by the model of Nakada [1969] in terms of variable source region enrichment due to coronal thermal gradients.

To Ann,

Without her understanding and encouragement, this work would not have been possible.

ACKNOWLEDGEMENTS

I should like to thank my advisor, Dr. George Gloeckler, for his support and guidance throughout my graduate career.

I also express my gratitude to the co-experimenters of the University of Maryland/Max-Planck-Institut experiments on the IMP spacecraft, Drs. C. Y. Fan and Dieter Hovestadt. Dr. Hovestadt kindly made his ULET data for elemental abundances available.

The programming for routine data processing was performed by John Dalton and Keith Hope. Dave Isaksen wrote the special programs to extract ULET abundances from the data tapes.

The mechanical design and construction of the IMP experiments was done by John Cain and Bob Cates. The electronics were designed by Ed Tums. The solid state detectors were made by Joe Gigante and Bob Lundgren. Last minute detector changes and electronics modifications were performed by Maurice Pairel.

Janet Schenck cheerfully typed several drafts and the final version of this thesis.

Finally, I acknowledge many conversations with Dr. Fred Ipavich. Throughout, Fred treated me as a colleague and a friend.

This research was supported by the National Aeronautics and Space Administration under contract NAS-5-11063. Computer time was provided in part by the University of Maryland Computer Science Center.

TABLE OF CONTENTS

LIST OF TABLES

LIST OF FIGURES

I. INTRODUCTION

The first evidence of the presence of nuclei heavier than helium in solar cosmic rays was found by Fichtel and Guss [1961] in the 3 September 1960 solar particle event. The observation was made with a nuclear emulsion track detector, lifted to a high altitude by a sounding rocket as part of the SPICE (Solar Particle Intensity and Composition Experiment) program. The first evidence of iron group nuclei did not come until the 2 September 1966 event [Bertsch, Fichtel, and Reames, 1969].

The detectors used in these experiments were track detectors flown on rockets or balloons, and hence were hampered by short exposure times (typically 5 minutes), low time resolution, and high threshold energies. In spite of these drawbacks, however, the experimental results provided interesting constraints on the acceleration and propagation process at high energies. These first measurements showed, for example, that the relative abundances of the energetic solar cosmic ray medium and heavy nuclei at the same nuclear charge to mass ratio, particularly helium, carbon, and oxygen, were approximately constant from event to event [Biswas and Fichtel, 1965]. In spite of the extreme variations from one event to another of the proton to helium ratio, which showed changes of over an order of magnitude among events (from 10 to 100 MeV per nucleon) [Sakurai, 1974], the constancy of the abundances of heavier elements was not unexpected, because of the similar rigidities of helium and fully stripped heavies. The differential energy per

nucleon spectral shape of the medium-group ($6 \leq Z \leq 10$) nuclei was found to be the same as that of helium, within uncertainties, above 10 MeV per nucleon [Biswas and Fichtel, 1964].

In addition, the abundances of the nuclear charge 6-26 group seemed to mirror the solar photospheric abundances as determined by spectroscopic measurements. It is believed that these medium and heavy nuclei in the solar cosmic particles are a good sample of the relative abundances at the sun, and therefore are a more direct means of sampling these abundances than is otherwise available. In fact, Bertsch et al [1972] and Crawford et al [1975] have suggested revisions in the relative solar abundances of neon, argon, and sulfur, based on their measurements of these nuclei in solar radiation above 15 MeV per nucleon. Another important consequence of this work has been the determination of the relative abundance of helium, which cannot be measured spectroscopically [Aller, 1971]. The problem of medium and heavy nuclei in solar cosmic radiation thus seems to be well understood at energies greater than about 10 MeV per nucleon.

Recently, the measurements of medium and heavy group nuclei in solar flares have been extended to lower energies (less than 10 MeV per nucleon) by several groups, using both passive detector systems (i.e., track detectors and nuclear emulsions) and active systems (telescopes, etc.) on balloons, rockets, and satellites. The most interesting result of these low energy measurements is the indication of an enhancement, over photospheric values, of the medium

and heavy nuclei relative to helium--an enhancement which is variable from flare to flare.

Armstrong and Krimigis [1971] summarized the He/CNO data for thirty-five events during the period 1967-1968, and were the first to show that the composition at low energies (0.5-2.5 MeV per nucleon) was different from that at higher energies. Armstrong et al [1972] compared their satellite data for this ratio with the SPICE emulsion results from 1960-1969. The satellite data have an average He/CNO ratio of 27 ± 9 while the rocket data average 58 ± 5 for the energy range 12 to 100 MeV per nucleon. Both energy and event variations seem likely. Teegarden et al [1973] reported He/O ratios at 13.5-47 MeV/nucleon which differ significantly between the April 1971 and September 1971 events. For the latter event they obtained a He/CNO ratio of 26 ± 2. They also observe Fe/O ratios for these two events which differ by a factor of six, but which are statistically consistent with a constant value. Mogro-Campero and Simpson [1972], however, derived Fe/O ratios above 5 MeV per nucleon for seven events and showed significant variability--as much as a factor of 20. Their results were obtained by integrating over the major portion of each event, and using the data from IMP-4 and IMP-5 to extrapolate their OGO-5 data for oxygen from 14 MeV per nucleon down to 5 MeV per nucleon. The overall averages from all seven events indicated that solar species above silicon were preferentially enhanced relative to the photospheric values. The enhancement factor for iron is between 10 and 20.

Crawford et al [1972] found no evidence of composition variations between the January and September 1971 events, using plastic detectors aboard SPICE rockets. They did observe, however, that the Fe/Si ratio decreased with energy over the range 1.5-50 MeV per nucleon. The overall change is by about a factor of 4.

Price et al [1971] analyzed tracks left in the Surveyor 3 TV camera filter, which was exposed on the moon for about 2.6 years. They compared the iron spectrum to a helium spectrum obtained from satellite data integrated over the same time period, in the energy range 6-10 MeV per nucleon. The He/Fe ratio inferred from their results ranges from about 230 at 6 MeV per nucleon to about 560 at 10 MeV per nucleon. The latter value agrees well with that obtained at higher energies.

Van Allen et al [1974] have recently reported results which indicate that the He/medium ratio increases with time over the course of a single flare. The implication is that the medium group nuclei from a flare arrive at the earth before the helium.

Many attempts have been made at explaining the observed composition enhancements [Price et al, 1971; Cartwright and Mogro-Campero, 1972; Van Allen et al,1974]. Most of these mechanisms involve incomplete stripping of the heavy ion's electrons, followed by some form of Fermi acceleration. Thus, when the particles reach the acceleration region, the partially ionized heavy nuclei are preferentially accelerated, since more of these have a rigidity greater than the cut-off rigidity for acceleration [Wentzel, 1965] at a given energy per nucleon.

The ionization states are also a sensitive measure of the temperature at which a particle has been accelerated or stored, the amount of matter it has travelled through, and its rigidity (since rigidity varies as mass/ionic charge - e.g. at 100 keV per nucleon, Fe^{+12} has a rigidity of 64 MV, while Fe^{+26} has rigidity of 30 MV and He^{+2} has 27 MV).

In view of the importance of the role of a particle's rigidity, in particular, in acceleration and propagation processes, it seems essential to measure the ionic charge states of solar particles and obtain accurate values for their charge to mass ratios as a function of energy. Indirect measurements have been made in the past. Sullivan and Price [1973], using observed spectral turn-downs on a rocket flight, reported charge states for iron at 2 MeV per nucleon of 22^{+4}_{-1}, based on calculated cut-off rigidities. Braddy et al [1973] have presented evidence, based on spectral shapes, that iron should be completely stripped while being accelerated.

The University of Maryland electrostatic energy-charge analyzer experiments on board the earth-orbiting satellites of IMP-7 and IMP-8 are the first devices designed to measure the ionic charge states of low energy particles, down to less than 40 keV per charge. Results from these experiments, which have been presented earlier, indicated that low energy carbon and oxygen are nearly fully stripped [Gloeckler et al, 1973; Gloeckler et al, 1974; Sciambi et al, 1974; Gloeckler et al, 1975a]. This work represents an attempt at a systematic, statistical study of the charge states, energy spectra, and abundances of low energy carbon and oxygen from the sun.

Chapter 2 of this work, supplemented by Appendix A, gives a complete description of the IMP-8 experiment.

In Chapter 3, data from ten solar particle events observed by the IMP-8 experiment are presented. These data contain several new features. The ionic charge states of carbon and oxygen are found to be remarkably consistent from event to event, in spite of wide variations in other event characteristics such as alpha/CNO ratios, event size, etc. Spectral index data from the lowest energy CNO channels indicate a spectral "turn-down" not attributable to velocity dispersion which is highly correlated with the low energy proton flux. A time variation of the alpha/CNO ratio throughout an event is found which is consistent with the observations of Van Allen et al [1974]. Measurements of the ionic charge states of iron at less than 10 keV per nucleon are made for the "iron-rich" event reported by Gloeckler et al [1975b], which indicate that the mean ionic charge state for low energy iron is about 10 to 12.

In Chapter 4 the charge state results for carbon, oxygen, and iron are shown to be consistent with ionization state equilibrium established in the quiet corona, at an electron temperature of 1.5 x 10^6 ^oK. If the particles are accelerated in regions of high coronal temperatures ($T \geq 10^7$ ^oK) [Cartwright and Mogro-Campero, 1972, McGuire et al, 1975] or stripped during acceleration, then some form of post-acceleration trapping is required. It is demonstrated that this trapping, combined with adiabatic deceleration, can account for the features observed in the heavy ion spectra.

II. INSTRUMENTATION

The University of Maryland experiment on board the IMP-8 spacecraft is fully described in Appendix A. The characteristics are briefly repeated here for the convenience of the reader. The experiment is an electrostatic deflection sensor. An ion entering the instrument has its entrance trajectory defined by a collimator (see figure A-1). The particle then enters one of three electrostatic field regions where its path is deflected by an amount inversely proportional to its kinetic energy per charge. On exit from the deflection cavity, the ion strikes one of an array of rectangular solid state detectors, each of which covers a well-defined deflection, and hence energy per charge, range. Pulse-height analysis of the detector signal allows a direct measurement of the particle's total kinetic energy, from which its charge may be determined. In addition, by using multiple energy thresholds on signals of several detectors, counting rates having well-defined energy limits and hence charge responses are generated with time resolutions as short as five seconds. Several of these rates are sectored into four directional quandrants in the ecliptic plane, providing data on particle anisotropies. A plastic scintillator anticoincidence cup and an array of solid-state anticoincidence detectors placed behind the detector array prevent analysis of penetrating particles.

Background correction of a detector's pulse-height histogram is performed by subtracting a normalized histogram obtained from

the same detector during quiet times, when the counting rates are at their lowest values. During these quiet times, analysis of pulse-height histograms indicates that the detectors respond primarily to the secondary electron background produced in the spacecraft.

The relative abundance of individual charge states may be determined by fitting computed instrument response curves to the observed pulse-height distributions, as described in Appendix C. A full description of the instrument response characteristics is given in Appendix B. The sensor is capable of fully resolving ionic charge states 1 to 4 for elements up to oxygen. In addition, charge states 5 to 8 are separated sufficiently so that, by means of a simple iteration procedure, abundances of these individual states may also be determined. (For example, the charge-state resolution of detector P3 is plotted in figure 2-1.) Complete charge state identification for carbon and oxygen down to about 40 keV per charge is thus obtained. Of course, the individual elements may not be resolved in this manner since only the ionic charge (as opposed to nuclear charge) is determined. In many cases, however, the ions may be completely identified (i.e., ionic charge and nuclear charge) by using the simultaneous nuclear abundance information provided by the Ultra Low Energy Telescope (ULET) [Hovestadt and Vollmer, 1971] of the Maryland/Max-Planck-Institut experiment at somewhat higher energies.

ULET is dE/dx vs total energy telescope with a geometrical factor of .53 cm^2 sterad. The sensor is pictured in figure 2-2. The front, ΔE element (D1) is a thin-window flow-through proportional counter, with a total mass of ∿ 300 $\mu gm/cm^2$. The rear, E element (D2) is a silicon surface barrier detector. A plastic scintillator anticoincidence cup (A) surrounds the detector assembly. The low mass of the ΔE element allows two parameter analysis of incoming particles down to < 100 keV per nucleon for iron. Different elemental tracks can be reliably (i.e., automatically) separated down to about 600 keV per nucleon. Every three hours ULET changes its analysis threshold, so that it alternately analyzes all incoming particles, and only those particles heavier than helium. ULET shares the electrostatic energy-charge analyzer's pulse height analyzers and telemetry on a $\frac{3}{4} - \frac{1}{4}$ basis, and both instruments are contained in the same spacecraft module.

IMP-8 (Explorer 50) was launched from Cape Canaveral, Florida on 1973 October 26 at 0226 GMT. The spacecraft achieved an elliptical orbit(shown infigure 2-3) with a mean apogee of about 45 earth radii and a perigee of ∿ 28 RE, inclined 29° to the ecliptic. The University of Maryland experiment was turned on on October 30 and has operated normally since that time.

III. OBSERVATIONS

The majority of the ten events used for the study were of small or moderate size. The reason for this selection is that during periods of large high-energy proton fluxes, the shape of the background histogram for a detector changes, making correction of the histogram for background difficult. In addition, in an attempt to exclude from the analysis particles of magnetospheric origin [Fan et al, 1975], only events observed when the spacecraft was outside the earth's bowshock-magnetotail region (SEV angles 240° - 120° in Figure 2-3) were used. Characteristics of the events analyzed are shown in Table 3-I.

The PHA Data

For each event, pulse-height histograms were accumulated over the major portion of the active period. Each histogram was corrected for background contributions by subtracting a suitably normalized quiet time histogram from the same detector (see Appendix C). Figure 3-1a shows a typical uncorrected pulse-height spectrum (histogram) obtained during the solar flare particle event of 1974 June 22. The measured, smoothed background distribution is shown as a dashed curve, and the histogram after background correction is shown in Figure 3-1b. This histogram was obtained from IMP-8 detector P3, which responds to ions in the energy range 130 to 220 keV per charge. The triple-peaked shape of the histogram is characteristic of every event studied to date. The two left-hand peaks are produced by protons and alpha particles respectively, while the right-hand peak is due to particles having ionic charges 5-8 for carbon and oxygen, and $8 \leq Q \leq 12$ for iron. The large dip

between the alpha peak and the Q=5-8 peak is statistically consistent with a complete absence of ionic charges 3 and 4. In none of the events examined has there ever been any evidence for the presence of these two charge states. At this point, computed instrument response curves for ions of various charges were fit to the data in order to determine ionic abundances. The first stage of the fitting of charge states to the PHA data was to determine the abundances of ions of charge 5, 6, 7, and 8, regardless of nuclear charge. In order to do this, all ions with charge states 5 and 6 were assumed to be carbon and all ions with charge states 7 and 8 were assumed to be oxygen. (Some assumption of the nuclear charge is necessary to correct for the nuclear defect [Lin and Campbell, 1973; see Appendix B].) Next, to determine the amount of oxygen present with an ionic charge of 6, elemental abundance data for the same time period were obtained from ULET at $\geq$ 600 keV per nucleon for the ratio of carbon to oxygen. This ratio was assumed to remain constant down to energies appropriate for the deflection sensor, and was used as an input to the program MSPCT (see Appendix C) in order to determine the relative abundances of C^{+6} and O^{+6}. After analysis of the iron rich 1974 May 14 event, it was found necessary to correct the charge state data from most other events for iron contamination.

The Ionic Charge States of Iron

The 1974 May 14 event is part of the "iron rich" event reported by Gloeckler et al [1975b]. They find during this time period a sustained emission of particles with a composition richer in iron

than in oxygen. The small event on May 13 produced sufficient fluxes for charge state analyses to be performed. During the time period for which PHA histograms were accumulated, ULET data at 600 keV per nucleon indicate that the iron/oxygen ratio is about 2.5, and that the medium-group spectral index is about 2. If the composition remains so enriched down to the energies seen by the deflection sensor, then most of the heavier ions seen by the electrostatic sensor should be iron. The solid histogram in Figures 3-2a and 3-2b shows the observed pulse-height distribution from detector P3 during this period. Note the presence of a large peak due to heavy ions centered at about 1 MeV. By using the ULET abundance data for C/O and Fe/O, it is possible to generate predicted response histograms based on various ionic charges for iron. For example, if iron were fully stripped, i.e., all iron was Fe^{+26}, the observed histogram should have taken the form of the dashed curve in Figure 3-2b. Clearly the required Fe^{+26} peak (the rightmost dashed peak) is not present in the observations, and the measured oxygen flux is above the predicted value. Thus it must be concluded that iron is only partially stripped at 150 keV per charge; in order for Fe ions to appear in the 1 MeV peak, the mean ionic charge must be about 10. In the dashed curve of Figure 3-2a, iron charge states of 8 to 12 have been fit to the data. The measured charge state distribution then is similar to that of the solar wind [Holzer and Axford, 1970]; our measured relative abundances of the +10, +11, +12, and +13 ionization states for iron are 15%, 35%, 30%, and 20% respectively. The fit to the data in this case is extremely good. Using these measured charge states, it is found that the agreement between the deflection sensor and ULET for the iron fluxes is excellent (Figure 3-3). So by requiring that the spectra

from the electrostatic sensor and the ULET join smoothly, the first direct measurement of the charge states of low energy iron has been made [Gloeckler et al, 1975c].

Iron Contamination of the Carbon and Oxygen Peaks

The fact that iron is present in these low charge states (i.e. overlapping the carbon and oxygen peaks) makes it necessary to correct the charge states of carbon and oxygen determined in other events, even though the measured iron abundances are small. The reason is that for a steep spectrum even a small abundance of partially stripped iron can make a large contribution to the carbon-oxygen peak.

The deflection sensor measures the kinetic energy per charge of an incident ion. Abundance ratios are usually calculated at equal energy per nucleon. Suppose that the incident ions are species 1 with charge Q_1 at kinetic energy E_1, and species 2 with charge Q_2 at kinetic energy E_2. Then in a given detector,

$$\frac{E_1}{Q_1} = \frac{E_2}{Q_2}$$

Defining the energy per nucleon $\varepsilon_n = E_n/A_n$

$$\frac{\varepsilon_1 A_1}{Q_1} = \frac{\varepsilon_2 A_2}{Q_2}$$

or,

$$\varepsilon_1 = \varepsilon_2 \left(\frac{A_2 Q_1}{A_1 Q_2}\right)$$

If the incident flux of particles is a power law in energy per nucleon,

$$F = \alpha\varepsilon^{-\gamma}$$

then the ratio of fluxes in the detector will be

$$\frac{F_1}{F_2} = \frac{\alpha_1}{\alpha_2}\left(\frac{\varepsilon_1}{\varepsilon_2}\right)^{-\gamma}$$

$$= \frac{\alpha_1}{\alpha_2}\left(\frac{Q_1 A_2}{Q_2 A_1}\right)^{-\gamma}$$

$$= \alpha_{12}\,\eta$$

where α_{12} is the abundance ratio of species 1 to species 2 at equal energy per nucleon and $\eta = \left(\frac{Q_1 A_2}{Q_2 A_1}\right)^{-\gamma}$ is a spectrum dependent abundance enhancement factor. For a spectral index of $\gamma = 3$, Fe^{+12} is apparently enhanced over its actual abundance relative to O^{+6} by a factor of 5.3. Thus, in all events with a steep spectrum (γ greater than 1) or a large iron abundance, the computed carbon and oxygen histograms must be corrected by subtracting iron in appropriate charge states. This will tend to reduce the abundance of O^{+8}, as the observed iron charge states fall at the high end of the carbon-oxygen range.

The Rate Data

The pulse-height analysis data are approximately an order of magnitude more sensitive to variations in cosmic ray intensity than the rate data. In addition, these data represent the only way to determine the ionic charge states of the incident particles. However, the pulse-height analysis is restricted by spacecraft telemetry to two

analyses every 1.28 seconds. This low rate of accumulation means that the use of PHA techniques is statistically not feasible for short time periods (i.e., less than 6-12 hours when the EECA has 3/4 of the telemetry time). Because of this limitation, the PHA data are insensitive to short term variations of event characteristics; hence the results based on PHA analysis represent an average over the event. It becomes necessary therefore to use the rate data in addition to the PHA data in order to verify event characteristics, to obtain time profiles of the helium/medium ratio, and to examine velocity dispersion, anisotropies, etc.

The counting rate data are corrected for background very simply using the P5 detector rate, which counts only background. Since the background (due to secondaries and penetrating particles which are not anticoincidenced) should be more-or-less omnidirectional, the ratio of the background counting rates in two detectors should be a function of their thresholds and the ratio of their uncollimated geometrical factors, or their active areas. Thus, a given rate R_n is corrected for background by subtracting a well-determined fraction of the P5 rate R_5.

In addition to plotting particle fluxes determined from the rate data, certain ratios of fluxes are also plotted for the events. For example, the ratio of the P2 flux to the P2" flux gives the helium/medium-group ratio. The spectral index between any two rate channels can be determined from

$$\gamma = -[\log(J_2/J_1)]/[\log(E_2/E_1)]$$

where J_n and E_n are the measured background-corrected fluxes and center point energies of the rate channels.

So, by using both the rate data and the pulse height data, a reasonably complete picture of the event emerges.

The Events

The first event analyzed was the 1974 July 4 increase. This particle event was the result of a very complicated series of flares involving three sudden commencements (abrupt increases in the earth's magnetic field due to the arrival at the bowshock of a high-speed plasma stream) at least one of which was associated with an interplanetary shock. During this event the highest fluxes of any event since the launch of the IMP-8 spacecraft were observed. Rate data for 15-600 keV per nucleon ions heavier than helium indicate a strong bend-down in the energy spectra below 100 keV per nucleon, even late in the event, which cannot be attributed to velocity dispersion. These rate data are shown for the entire event in Figure 3-4, where the fluxes at 40, 80, and 150 keV per charge, corrected for background, are plotted. The two lowest energy fluxes track each other throughout the event at the same level. Rate data for protons and helium show no such bending within the energy range of the detectors. (It should be noted however that the low energy limits for these two species are considerably higher than for CNO.) The helium/CNO ratio at 80 keV per charge is plotted in Figure 3-5. This ratio starts low at the beginning of the first particle increase on day 185. The ratio grows with time, reaching its local maximum late in the first rate peak. It then drops again as the second large increase begins, and once more grows larger with time during the particle increase.

Pulse-height analysis data support these observations, and indicate that carbon and oxygen are present only in ionic charges >5. The event averaged energy spectra for helium and CNO are shown in Figures 3-6 and 3-7 respectively. After correcting for iron contamination, we find that at 150 keV per charge the abundances of charge states 5 and 6 for carbon are 28% and 72% respectively, and that the abundances of oxygen charge states 6, 7, and 8 are 68%, 27%, and 5% respectively at the same energy. The abundances for these ions at 500 keV per charge are 25%, 75%, 70%, 24%, and 6% respectively: the differences are not statistically significant. The mean charge states of carbon and oxygen are plotted as a function of energy in Figure 3-8--we see little variation.

The PHA data were also divided into two parts, one early in the event, and the other late (the dividing time was 0900 on day 187, July 6). Comparison of ionization states derived from these two parts showed no significant differences: the ionic charge states appear to be constant throughout the event.

It is instructive to examine a simpler event--one in which local effects are not likely to be as important as in the July 4 flare. In Figure 3-9, for example, are shown proton, helium, and CNO spectra averaged over the time period 1974 June 10 0^h to 1974 June 12 0^h. This event, associated with a small flare on June 8, is typical in that the CNO spectrum flattens at lower energies. An unusual feature of this event (as compared with the others examined) is that the helium also seems to show a flattening; in fact, this is the only case in which such an effect has been seen in the alphas in the energy range of the instrument.

Charge state data from pulse-height analysis show that the relative abundances C^{+5}/C, C^{+6}/C, O^{+6}/O, O^{+7}/O, and O^{+8}/O are 17%, 83%, 82%, 16%, and <2% respectively at 150 keV per charge. Again, at high energies (500 keV per charge) there are no significant differences in these fractions. Mean charge states for carbon and oxygen are plotted vs energy in Figure 3-10.

Figure 3-11 shows the time variation of the spectral index γ ($J \sim E^{-\gamma}$) for heavy ions between 20 and 40 keV per nucleon during the June 10 event. The effect of velocity dispersion is evident up to the beginning of day 161, at which time the spectral index settles down to a low, more-or-less constant value and remains at that value to the end of the event. The bend-over in the spectrum (low spectral index γ) cannot, therefore, be attributed to simple velocity dispersion.

Using the arrival times of the low energy heavy ions of various energies, it is possible to calculate their diffusion coefficients, $\kappa_{\parallel}$, based on travel distances (along the average spiral magnetic field) of 1.2 AU for this event. The increase in P1 is seen about 37 hours after the flare, while that in P2" is seen about 4.5 hours earlier. The P6 increase is seen about 25 hours after the flare. Inserting these times into the relation for diffusive propagation

$$\kappa_{\parallel} = \frac{R^2}{6\tau}$$

values of $\kappa_{\parallel}$ of between 4×10^{20} and 6×10^{20} cm^2 per second are obtained for ions with energies between 20 and 250 keV per nucleon. The very small (<3%) residual anisotropies which are observed after correction for the Compton-Getting effect [Ipavich, 1974] are consistent with this low value of the diffusion coefficient. These values are similar to

those obtained for other events at low energies by Lin et al [1974] and Lupton and Stone [1973].

In Figure 3-12 is plotted the helium/medium ratio as a function of time for this event. Again, the ratio tends to increase as the event progresses, as though the heavier ions arrive before the alphas.

Figures 3-13 and 3-14 show proton, helium, and CNO spectra from two other events in the study, 1974 June 22 and 1974 November 8. The June event shows no turndown in the spectra, even at the lowest energies. The November event shows a large bendover in the Q=5-8 group spectrum, similar to that observed in the July 4 and June 10 events. However, rate data indicates that there may be some local effects present in this event. In both these events, as well as in all the others examined, the mean charge state of carbon is about 5.7, and of oxygen is 6.2. This constancy of the ionic charge states stands out, despite great variations in event parameters.

Ionization state composition data for all ten events are shown in Table 3-II. For each event, the relative abundances C^{+5}/C, C^{+6}/C, O^{+6}/O, O^{+7}/O, and O^{+8}/O have been averaged over energy, as there were no statistically significant variations of the charge states with energy. The abundance of each of these ions averaged over all events is shown in the last line. We note once more the remarkable consistency of the ionic charge states from event to event. Also included in Table 3-II are measured ion abundances in the solar wind, and the expected charge state abundances in the solar corona.

Table 3-III summarizes the spectrum data for the ten particle events, all of which were associated with solar flares on the western disc of the

sun. Four of these events show an "unusually low" spectral index ($\gamma < 1$) at low energies for CNO, while, with the exception of the June 10 event, none show a clear alpha turndown. We must caution, however, that since for alpha particles the low energy limit of the observations is 40 keV per nucleon, a factor of two higher than the lowest heavy ion energy, the possibility of an alpha turndown below 40 keV per nucleon cannot be ruled out. On the other hand, one can definitely say that if a turndown is present in the alpha spectra, it is not nearly as strong as for the case of the heavy ions, or occurs at lower energies.

The alpha/CNO ratio at 40 keV per nucleon shows a great variability from event to event, but there is no correlation of CNO abundance with the degree of turndown in the spectra; nor is there a correlation with helium flux, CNO flux, or location of the flare. There is, however, a strong correlation of CNO spectral index γ_{CNO} with the low energy (<220 keV) proton flux averaged over the event. This interesting correlation is evident in Figure 3-15, where the CNO spectral index from 40-80 keV per charge is plotted vs the "event-averaged" 130-220 keV proton flux. The trend is clear: the larger the flare as measured by the low energy proton flux, the stronger the bend in the spectrum.

Summary of Observations

The major observations may now be summarized: 1) The mean ionic charge states of carbon and oxygen are 5.7 and 6.2 respectively, showing no variation with energy from 37 keV per charge to greater than 1 MeV per charge, and only statistical fluctuations from event to event; 2) The mean ionic charge for iron over the same energy range is found to be 11.7±0.6 (for one event); 3) In the larger events, a turndown is observed in the medium-group differential energy spectra below about

100 keV per nucleon, which seems to be well correlated with the event size as measured by the "event-averaged" 130-220 keV proton flux; and 4) In two events a time variation in the alpha/medium group ratio at 80 keV per charge is found which indicates that the medium group nuclei arrive before the helium. In addition we see a large variability from event to event in the heavy ion abundances relative to helium.

IV. DISCUSSION

As was pointed out in the previous section, the ionic charge states of the medium group nuclei measured in the events of this study show remarkable consistency from event to event. In this section the significance of the observed charge states and the features of the heavy ion spectra is examined, and it is shown that these measurements are a sensitive probe of the conditions of the acceleration region.

The Charge States and Characteristic Temperature of the Ions

Can the charge states be explained in terms of flare region conditions? According to current theory on x-ray emissions, during the flash phase of a flare, large numbers of keV electrons must be generated [Takakura, 1967; de Feiter, 1974; Kane, 1973, 1974]. It has been suggested [Braddy et al, 1973; Sakurai, 1975] that these electrons could strip heavy ions by impact ionization. However, the observed charge states, while high, do not indicate complete stripping, as would be expected if this mechanism were the dominant one.

It may be noted from the work of Jordan [1969] and others [Allen and Dupree, 1967; Cox and Tucker, 1969; Lange and Scherb, 1970] that the ionization states observed are consistent with those expected for ions in thermal equilibrium with an electron gas at a temperature of 1-2 x 10^6 °K. In addition, the charge states are very similar to those observed in the solar wind [Bame et al, 1968, 1970], although the elemental abundances are different. It thus seems likely that the low energy heavy ions seen near the earth have

achieved charge state equilibrium in regions of the solar corona, from which the solar wind orginates. In figure 4-1 are plotted, after Nakada [1969], the expected charge states vs. temperature for several elements, with our data superposed. The data, corrected for iron abundances in each event as measured by ULET at 600-1000 keV per nucleon, show that both carbon and oxygen charge states fit well to a temperature of about 1.6×10^6 °K. Now, using measured upper limits on the relative abundances of C^{+4} and O^{+8}, both lower and upper limits can be set on the temperature of the region in which the ions achieved charge state equilibrium. Specifically, since the ratio $C^{+4}/(C^{+4}+C^{+5}+C^{+6})$ is observed to be less than 10%, we can set $T_{min} > 1.0 \times 10^6$. And since the ratio $O^{+8}/(O^{+6}+O^{+7}+O^{+8})$ is less than 10%, $T_{max} < 2.5 \times 10^6$.

How sensitive are the charge states to the source region temperature? Kafatos and Tucker [1972] have done a study of the response of the ionization equilibrium states to changing plasma temperatures. They find that if the region containing the particles is instantaneously heated to 10^7 °K at an electron density of 10^9 cm^{-3} (typical parameters for the flash phase of a flare), the characteristic ionization time t_I for the heavier ions is very short. For carbon, for example, t_I is of the order of 10 seconds - much shorter than the duration of the flash phase. (By contrast, the ionization time for carbon to be heated from lower temperatures to 10^6 °K at the same electron density is about 800 seconds.) Thus immediately after

heating the charge states of the medium group ions should reflect the higher temperatures--carbon and oxygen should be fully stripped. Even if the particles immediately return to a region of temperature and density characteristic of the quiet lower corona, there is considerable hysteresis in their ionization states. For $n_e = 10^8$ cm^{-3}, $T_e = 1.5 \times 10^6$ °K, the recombination time t_r for oxygen to return to its equilibrium charge states is of the order of 5000 seconds. This time may be considerably lengthened, for if the particle moves radially outward the electron density it sees rapidly decreases, and the recombination time varies inversely as electron density.

We thus have the problem of explaining how the ions we observe, which were clearly flare accelerated, can have ionization states which are typical of the quiet corona. The first possibility is that the temperature of the acceleration region does not exceed 1.5×10^6 °K - the quiet corona temperature.

Although there is no direct experimental evidence allowing determination of the site of flare acceleration of heavy particles, there is reason to believe from x-ray and radio burst observations of the flash phase that the acceleration of electrons, at least, occurs in the lower corona, at temperatures of $1\text{-}3 \times 10^7$ °K and densities greater than 10^9 cm^{-3} [Kane, 1973; Kahler, 1973]. This is consistent with current flare models [Sturrock, 1973], and with observations of flare site temperatures [Strauss and Papagiannis, 1971]. Thus the only available evidence contradicts acceleration at low temperatures.

The second possibility is that the particles, after acceleration at high temperatures, are trapped in regions of $T_e \sim 1.5 \times 10^6$ °K for a time density product of the order of 5×10^{11} sec cm^{-3}. This trapping region may be the acceleration site itself, cooling back to pre-flare temperatures; alternatively the particles may escape the acceleration site only to be trapped elsewhere in the corona. Even if the first possibility is accepted and the ions are accelerated at low temperatures, if they have been stripped by flare-associated keV electrons some storage may be required to reestablish the characteristic charge states.

There is evidence for trapping of flare-accelerated particles. Pulsations in microwave bursts may indicate temporary containment of energetic particles in closed mangetic loops [Newkirk, 1973]. Stationary type IV bursts have been interpreted as synchrotron emission of relativistic particles trapped in stable magnetic arches, precipitating into the corona--these may last for hours or days [Wild and Smerd, 1972]. Stable closed loops suitable for trapping have been observed out to 2.5 $R_\odot$ [Boischot, 1974]. The possibility of trapping or storage of low energy protons has been suggested by Fan et al [1968], Anderson [1969], McDonald and Desai [1971], Simnett and Holt [1971], Simnett [1971, 1972, 1973], and Ma Sung et al [1975] among others.

Spectral Shapes, Particle Storage, and Energy Loss

If the ions are stored somewhere in the corona after acceleration, it is expected that their energy spectra will suffer some degradation

due to ionization energy losses. The presence of such a degradation might give evidence as to whether storage of the particles actually takes place. Is the observed spectral turndown produced by the effects of ionization energy loss during storage, or is it caused by propagation effects in interplanetary space?

Verzariu and Krimigis [1972] have pointed out that by allowing the diffusion coefficient κ to depend on particle velocity, a bend in the spectrum can be produced by adiabatic deceleration. But, since the energy change mechanism would depend only on particle velocity, different species observed at the same velocity should have experienced identical propagation effects, and thus should "map back" to the same source velocity. However, in the present case, the absence of a strong alpha turndown at the same kinetic energy per nucleon (or velocity) as for carbon and oxygen makes it unlikely that the bending is caused by a velocity-dependent κ. If the initial spectra were the same, then the same mechanism which produces a CNO turndown should produce the same degree of turndown in the alphas. Using an identical argument, the effect of a rigidity-dependent diffusion coefficient can be shown to be unlikely, since by virtue of their high state of ionization the carbon and oxygen have nearly the same rigidity (within 20-30%) as the alphas at the same energy per nucleon. Adiabatic deceleration can certainly change the shape of the spectra: The point here is that this deceleration should produce identical changes in the spectra of all species observed.

Having ruled out propagation effects, we now examine coronal trapping. Previous attempts to calculate the effect of storage on the spectra of flare particles have led to the conclusion that such storage could not explain the shape of the proton spectra observed at the lowest energies [Ahluwalia, 1971; Krimigis and Verzariu, 1971; Verzariu and Krimigis, 1972; Krimigis, 1973; Newkirk, 1973]. We point out, however, that in each of these cases, the authors have used a form of the energy loss equation which is invalid at low particle energies.

In calculating the effect of ionization energy loss on the spectra of the particles during propagation from the acceleration region and/or storage in the corona, it is important to use the correct form of the energy loss equation for low particle energies. The form valid at high energies, $dE/dx \sim 1/E$, breaks down as the particle velocity approaches the electron thermal velocity (v_{the}). For an electron temperature of $\sim 10^6$ °K, this corresponds to a particle energy of $\sim$ 225 keV per nucleon.

The problem of the slowing down of an ion in a fully ionized plasma has been treated by several authors. We use here the results of Itikawa and Aono [1965], who find a form of the energy loss equation which is valid for all values of the ion velocity. In the case where losses due to plasma ions are ignored, in the limit $M_i >> m_e$ this equation becomes:

$$\frac{dE_i}{dx} = -1.512 \times 10^{-12} \frac{n_e Q^2}{T_e M_i} \left\{ \ln\left(\frac{T_e^3}{n_e Q^2}\right)^{\frac{1}{2}} + 9.13 \right\} \left\{ \frac{\mathrm{erf}(u)}{u^2} - 1.129 \frac{\exp(-u^2)}{u} \right\} \tag{4-1}$$

with $u = 79.5 \sqrt{E_i/T_e}$, where E_i is the ion energy in keV per nucleon, T_e is the electron temperature of the plasma in °K, M_i is the ion mass in amu, x is the path length in cm, n_e is the electron density of the plasma (per cm^3) and erf is the normal error function: $\mathrm{erf}(u) = \frac{2}{\sqrt{\pi}} \int_0^u \exp(-x^2)\, dx$. In the low energy limit ($v_{ion} << v_{the}$) the specific energy loss dE_i/dx is proportional to v_{ion} or $\sqrt{E_i}$, while in the high energy limit ($v_{ion} >> v_{the}$), $dE/dx \sim 1/E_i$. The last bracketed term in (4-1) is plotted in figure 4-2. This function has the form predicted by Ginzberg and Syrovatskii [1964] for ion velocities near the plasma electron velocity.

It is instructive to first examine the behavior of a spectrum of particles in two limiting cases: One in which the particle population is propagated directly outward from the acceleration site to earth, passing through $\sim$80 $\mu gm/cm^2$ of matter, and the other in which the entire population is trapped for some time (independent of particle energy) before being released to propagate to earth. In the latter model the amount of matter passed through is dependent on particle velocity.

Consider first the case in which all particles are propagated through the same amount of matter. The low energy form of the ionization loss equation (4-1) predicts

$$\frac{dE}{dx} = -\alpha\sqrt{E} \quad .$$

After passage through a slab of matter, a particle of initial energy E_0 has its energy degraded to an energy E

$$E_0 = (\alpha x + \sqrt{E})^2 \; ; \quad \frac{dE_0}{dE} = \sqrt{\frac{E_0}{E}} \quad .$$

Now consider a differential spectrum of such particles. The initial spectrum $J_0(E_0)$ is degraded, and the new spectrum J (by conservation of particle number) obeys

$$J_0(E_0)dE_0 = J(E)dE$$

$$J(E) = J_0(E_0) \frac{dE_0}{dE}$$

or

$$J(E) = J_0[(\alpha x + \sqrt{E})^2] \frac{(\alpha x + \sqrt{E})}{\sqrt{E}} \quad .$$

If $J_0(E_0)$ is a power law in E_0

$$J_0(E_0) = A \, E_0^{-\gamma}$$

then,

$$J(E) = A \, (\alpha x + \sqrt{E})^{-2\gamma} \, (\alpha x + \sqrt{E}) \, E^{-1/2}$$

$$= A \, (\alpha x + \sqrt{E})^{1-2\gamma} \, E^{-1/2} \quad .$$

At the lowest energies ($\alpha x >> \sqrt{E}$)

$$J(E) \simeq B \, E^{-1/2} \quad .$$

So, in the low energy limit, the new spectrum is a power law with spectral index 1/2, regardless of the input spectral index.

Examining the case where all particles are stored for a constant time, it is found that in the low energy limit

$$\frac{dE}{dt} = v \frac{dE}{dx} \sim \sqrt{E} \frac{dE}{dx} \sim -C E .$$

Using a similar argument to that given above, it is found that for an incident power law spectrum $J_0(E_0) = A E_0^{-\gamma}$, at the lowest energies the new spectrum is

$$J(E) \simeq \exp[Ct(1-\gamma)] E^{-\gamma}$$

i.e., the spectral index is unchanged.

Model Calculations

We are now in a position to determine the effects of propagation and storage on the spectra of the particles. A number of model calculations have been made involving releasing an initial spectrum of particles (for simplicity assumed to be a power law $J(E) = J_0 E^{-\gamma}$) at a particular point in the corona, propagating them to another location, storing all particles there for a given time, and then allowing the particles to propagate outward to about 10 $R_\odot$ (the last value was chosen because here the electron density is about 5 orders of magnitude lower than the coronal maximum and any further propagation of the particles will contribute negligibly to the ionization loss). The corona has been assumed to be isothermal, with an electron temperature of 1.5×10^6 °K. An empirical fit to the coronal density profile of Allen [1963], $n_e = 3.6 \times 10^3 \exp(15 R_\odot/R)$ cm^{-3} was used. Energy loss was determined by numerically integrating equation (4-1) along the particle trajectories.

In figures 4-3 and 4-4 results of the model calculations are shown for various ions, for an initial power law spectrum $J(E) \sim E^{-3}$

and $J(E) \sim E^{-2}$, respectively, propagated outward from an injection point at 1.02 $R_\odot$ to a storage area at 1.4 $R_\odot$ (where $n_e = 1.4 \times 10^8$ cm^{-3}), trapped at 1.4 $R_\odot$ for 1000 seconds, and then propagated outward to 10 $R_\odot$. This gives a time-density product of about 2×10^{11} sec cm^{-3}, which is of the order required to reestablish charge states characteristic of 1.5×10^6 degrees. The particular values of storage radius and time do not affect the limiting slopes of the curves in figure 4-3, but only the time in which these limits are reached; the curves could as easily describe a spectrum stored at $n_e = 5 \times 10^6$ cm^{-3} (about 2 $R_\odot$) for 10 hours.

The factor Q^2/M in equation (4-1) is apparent in the difference in degree of flattening for alphas and heavier nuclei. Clearly a "kink" occurs in the spectrum, at the same energy for all species. In addition, the calculated energy spectra of both protons and helium show a mild turn-down.

Comparison with Observations

We note that the energy at which the bend in the spectra in figures 4-3 and 4-4 occurs is about a factor of 10 higher than the energy at which the spectra are observed to turn down in the events of this study (see figure 3-14)

The energy at which the bend occurs, E_B is, to first order, a function only of the parameter u in equation (4-1), or of $(E_i/T_e)^{1/2}$. In order to make the calculated spectra consistent with observations, E_B must be lowered by about a factor of 10. One way to accomplish this is by lowering the temperature of the

storage by a factor of 10. Limits which have been put on the temperature of the storage region from the observed charge states of the ions, however, are greater than 10^6 °K, far too high to produce the flattening at the observed energy. Storage at low temperatures (with correspondingly low equilibrium charge states) followed by stripping may be ruled out by the following argument: A turndown in the spectra of CNO which is more pronounced than for alphas, requires that in the storage region the parameter $\frac{Q^2}{M}$ in equation (4-1) must have been greater for CNO than for alphas, assuming all species are stored for the same time. Since for alphas, $\frac{Q^2}{M} = 1$, $Q^2 \geq 12$, or $Q > 3.5$ for carbon, which implies that in order for these high charge states to be maintained, the temperature in the storage region must again have been $> 8 \times 10^5$ °K. Therefore, coronal propagation and storage alone could not have produced the spectral flattening at the energies where it is observed. If the spectral turndown is the result of particle trapping and ionization loss, then some additional mechanism must also operate before we observe the particles.

A Model for Particle Propagation

On the basis of our discussions, it is suggested that the observed charge states and spectral bend come about in the following manner: Particles (alphas and heavier nuclei) are accelerated in a source region to a power law spectrum in kinetic energy. The particles are trapped near the source region at temperatures $T_e \sim 1.5 \times 10^6$ °K characteristic of a quiet corona. The particles lose energy through ionization loss, their spectrum flattens at about 800 keV per nucleon and the ions establish charge

state equilibrium with the ambient plasma. From the observations of the observed correlation between the degree of flattening and the low energy proton flux, it is concluded that either the storage time or the storage electron density is proportional to the "size" (i.e., total energy) of the flare. The particles are then diffusively propagated outward to the earth, losing energy by adiabatic deceleration. Here it is assumed that the diffusion coefficient is independent of particle parameters [Ma Sung et al, 1975], so that the adiabatic deceleration does not affect the shape of the spectrum, but simply moves it to lower energies [Venkatarangan and Lanzerotti, 1975]. Under these conditions, the required energy losses may be produced by a diffusion coefficient of the order of 5×10^{20} cm^2 sec^{-1} [Parker, 1965] which is consistent with our observations for at least one event (1974 June 10), and with the observations of others [Lin et al, 1974; Lupton and Stone, 1973] at low energies. Thus, the "bend" in the spectrum of CNO is moved down to the energy at which it is observed. Statistical errors in the helium observations, unfortunately, prevent an unambiguous identification of the predicted bending in the helium spectra.

It should be noted that the value of $\kappa_{\parallel}$ required above is only a average value. A diffusion coefficient which is very small close to the sun could have a large effect on energy loss, as most of the loss would occur there [Jokipii and Owens, 1975].

Because the theoretical results derived for alpha particles apply equally for protons, there should also be a bend in the proton

spectrum to match that of the alphas. Since the lowest observed energy for protons is even higher than that for alphas, it is not expected that this bend would be seen in the data presented here.

It should also be noted that all species appearing in Figure 4-3 were initially equally abundant. After storage, the heavy ion abundances are depressed relative to helium. Thus, in order to explain events which show enhanced heavy element fluxes, it is necessary either to have a "super enriched" source, or to invoke some mechanism which preferentially accelerates the heavier ions.

The mechanism of thermal diffusion in the corona, as proposed by Nakada [1969], can produce a source region which is enriched (to practically any degree desired) in heavier elements, depending on thermal gradients in the lower corona. The ionic charge states which are observed are consistent with those required by his model. For example, the iron charge states observed in the May 14 event would produce an enhancement of the Fe/O ratio of $\sim$ 10 for a coronal temperature gradient of 1°K/cm.

The Helium/CNO Ratio

The time profile of the alpha/CNO ratio must now be explained. Although the time variations of the ratio during an event are consistent with the observations of Van Allen et al [1974], our interpretation of the cause differs. Van Allen et al interpret their results as the effect of a rigidity dependent diffusion coefficient on partially stripped carbon and oxygen. The results

of this study indicate that the rigidities of low energy carbon and helium at the same energy per nucleon differ by only 20-30%, and that of low energy oxygen is ∿ 30% higher than low energy helium. It is unlikely that such a small change in rigidity could produce the required large change in the interplanetary diffusion coefficient. At the source, however, the composition is a strong function of temperature [Nakada, 1969; see especially his figures 5 and 6]. A gradual cooling of the source region throughout the event could produce the observed alpha/CNO profile. As the source region cools, the source becomes less enriched in heavier nuclei (relative to helium),and the alpha/medium ratio in the accelerated particle population increases. This source region cooling has been observed in soft x-ray emission from flares [Craig et al, 1973; Peterson et al, 1973]. Although these observations give timescales for cooling of the order of 1 hour, they extend only to about 8×10^6 °K. At lower temperatures the cooling time could be longer. We note that this interpretation is consistent with the observations and interpretation of Gold et al [1975] and Roelof et al [1975] of "coronal control" of cosmic ray events.

The same mechanism of thermal diffusion at the source could explain the variability of the average alpha/CNO ratio from event to event. The heavy ion enrichment depends on thermal gradients in the lower corona. As these gradients would be expected to vary greatly from flare to flare (due to differences in flare geometry), the alpha/medium ratio would also be expected to change from event to event.

Summary

The importance of observations of low energy ions from solar events as a probe of flare conditions cannot be overemphasized. From analysis of ten events, we can conclude:

1) Low energy carbon and oxygen appear in ionization states which bear the "imprint" of temperatures characteristic of the quiet lower corona, and show remarkable consistency from event to event.

2) The very consistency of these charge states implies that the low energy ions do not reach us directly, but are trapped in regions of electron temperature $T_e \sim 1.5 \times 10^6$ °K for some time - i.e., a time-density product of $\sim 5 \times 10^{11}$ sec cm^{-3}.

3) During this trapping the ions spectra are degraded by ionization energy loss. This degradation is consistent with the observations if strong adiabatic deceleration takes place, with the interplanetary diffusion coefficient having the value measured in one event.

4) A time variation of the alpha/medium group ratio has been found which is consistent with a variable source enrichment due to source region cooling.

5) The ionic charge states of low energy iron have been measured for one event, and here too the ionization states are characteristic of an electron temperature of 1.5×10^6 °K.

Additional event statistics from current experiments, and results from even lower energies with greater resolution in future experiments, promise a wealth of new data on solar particle acceleration and particle propagation in the corona.

- APPENDIX A -

THE UNIVERSITY OF MARYLAND ELECTROSTATIC ENERGY-CHARGE ANALYZER EXPERIMENT

The measurements of the energy and charge spectra of low energy interplanetary particles requires two parameter analysis from which the particle's total energy and charge can both be determined.

A technique commonly used consists of measurement of the energy loss and total energy for particles using a combination of thin and thick detector elements respectively. Telescopes employing the so-called "dE/dx vs E" method have achieved excellent chemical and isotopic resolution by using low noise silicon detectors as the sensitive elements of the sensors. In the past the low energy limit for two-dimensional dE/dx vs E analysis could not be extended below several MeV per nucleon because of lack of suitably thin dE/dx elements.

The usefulness of the dE/dx vs E analysis technique has been extended to energies below 60 keV per nucleon for iron by using a thin-window proportional counter as the dE/dx detector element. The Ultra Low Energy Telescope (ULET), included as part of the University of Maryland Experiment on the IMP 7 and 8 spacecraft uses a low mass ($\sim$330 $\mu gm/cm^2$) total thickness gas proportional counter as the energy loss rate, or dE/dx, detector and thus has a low energy limit for two dimensional analysis of 300 keV per nucleon for protons and 200 keV per nucleon for alpha particles.

To extend the range to even lower energies, and to determine the particle's ionic charge requires a different technique. The Electrostatic Energy-Charge Analyzer is the main sensor of the University of Maryland IMP 8 experiment. This device uses electrostatic deflection vs total energy measurements to determine the ionization state and energy of particles in the range of 37 to 1250 keV per charge (for charge $Q \geq 2$ particles). The sensor is similar in principles of operation to the instrument flown on IMP 7 [Fan et al, 1971], but is primarily designed to investigate positively charged ions and has a lower energy limit--a factor of three below that of the IMP 7 experiment. In this appendix the sensor and the electronics used for signal processing and data handling are described.

The Deflection System

The deflection d of an ion travelling through an approximately transverse electrostatic field generated by a potential V is related to the particle's kinetic energy T and its ionic charge Q through [Spiker, 1970]

$$d = \frac{2\gamma\, g\, VQ}{(\gamma+1)\, T} \qquad \text{(A-1)}$$

where g is a constant dependent on the deflector geometry and γ is the relativistic factor. Thus, by measuring simultaneously a particle's deflection in a known electrostatic field and its total kinetic energy one determines its ionic charge Q.

In the IMP instrument the deflection fields are created by applying voltages to two flat non-parallel magnesium plates, mounted on stand-off insulators inside a ground cavity (Figure A-1). One

plate is maintained at a potential of + 14.5 kV relative to the ground plate, the other at + 3.5 kV. Three field regions are thus created in the deflection cavity with potential differences of 14.5 kV (top), 11 kV (center), and 3.5 kV (bottom), corresponding to fields at the front edge of deflection plates of 7.25 kV/cm, 11 kV/cm and 1.75 kV/cm. These fields decrease as one moves away from the front edge due to the increased separation of the plates. However, this does not significantly affect the validity to first order of the expression (A-1) above. A passive collimator at the entrance of the cavity defines the arrival directions of incoming particles.

A charged particle entering the sensor is deflected in one of these three field regions. Its deflection is determined by the location of that one solid state detector in the array of eight which is triggered as the particle strikes its surface after exiting the deflection cavity. Simultaneously, pulse-height analysis of the triggered detector's output signal determines the particle's total energy. The differential energy range per charge of each detector is defined by its position and width (figure A-2) and does not depend on electronic threshold levels. Using eight discrete detectors we obtain eight differential energy channel analyzers (seven for positive ions and one for electrons) simply counting the number of particles which trigger each of the eight detectors. The charge and finer energy resolution within each of the 7 positive ion channels is achieved by pulse height analysis of the signals of that detector.

The Detector Array

The front of the detector array (Figure A-3) consists of seven thin (100 μ) silicon surface barrier detectors designated P1 to P4 and P6 to P8 in order of increasing energy of the particles able to reach them. In addition, a thick (1000 μ) Li drifted Si [Si(Li)] detector (called N) is included in the array at a position to intersect electrons. The signal from the N detector is not pulse-height analyzed--it serves only as a rate trigger. Detector P5 is covered with an aluminum foil just thick enough to stop protons deflected to it. This detector is identical to P2 and P6 and its purpose is to measure the shape of the background energy spectrum and the background rate. Continuous monitoring of the background spectrum and rate are essential because the background spectral shape was found to change during solar flare events. The detector energy per charge ranges and geometrical factors are listed in Table A-I.

Behind this front layer is an array of six thick Si(Li) detectors, positioned so that particles which penetrate one of the front detectors must also strike one of these. All back detectors are connected in parallel and are referred to as B. The requirement for pulse-height analysis of a given P detector P_i is $P_i \cdot \overline{B}$, since positive ions reaching these P detectors will be stopped in them. High priority for analysis is given to heavy ion events in certain detectors. The N rate requires N•B coincidence reflecting the high probability that electrons reaching N will penetrate and trigger B. The coincidence requirement assures identification of electrons unambiguously and serves to reduce background. The B anticoincidence for pulse-height analysis also helps in reducing background due to penetrating particles.

A plastic anticoincidence scintillator surrounds the detectors, preventing analysis of high energy penetrating particles and further reducing background. In addition, the scintillator counting rate is a measure of the integral proton flux above about 18 MeV, with a large geometrical factor (about 1100 cm^2 sterad).

The Collimator

The collimator at the entrance of the sensor cavity overcomes one fo the major disadvantages of the electrostatic deflection method, namely the inherently small geometrical factor. For deflection measurements to be meaningful the entrance angles of the entering particles must be severely restricted. This entails very strict collimation, with the result that such sensors usually have very small geometrical factors. We have overcome this problem to some extent by using a collimator with a large open area and many slits.

The 40 mm thick collimator consists of a total of 270 thin (0.144 mm) aluminum plates stacked together and rigidly attached to either side of a magnesium frame (Figure A-4). Aluminum was chosen because of low atomic number and moderate density, yielding a collimation thickness of approximately 5.4 gm/cm^2 for particles with skew trajectories. The curved frame (inside radius 270 mm) has 150 plates on the convex front side and the remaining 120 on the back. Each stack is secured to the frame by screws.

Each aluminum plate has 1521 slotted openings chemically milled through its surface (Figure A-5). These slots are 0.254 mm wide and

vary in length from 12.37 to 14.25 mm. Proceeding from the outermost to innermost plate the slots become shorter and the row spacings narrower. A total of 27 different plate types are used. Stacking these plates creates a series of vertically and radially converging tunnels through which particles may pass. The upper and lower collimator sections have a vertical acceptance angle of 6.10° while the center section has a convergence angle of 2.47°. The horizontal acceptance angle (in the ecliptic plane) is $\sim$ 60°. "Focusing" of particles is achieved by the combined vertical and horizontal convergence of the tunnels. The points of convergence lie along three separate arcs, one for each electric field region, 188.5 mm behind the collimator. The dispersion of particles on this arc represent the geometrical resolution of the focused collimator. This resolution depends on slot width, focal length, collimator thickness and stacking accuracy. Resolution of this collimator ranged from 1.6 to 1.7 mm (FWHM). The geometrical factors, a function of both acceptance angle and detector area, were calculated for the various detectors using a Monte-Carlo method and are listed in Table A-I, above.

To alleviate small angle scattering of both light and energetic particles in the collimator 30% of the plates were replaced with spacers to form "light traps". Three spacers were included with the 10 plates of each type for all 27 different types.

The Electronics

A simplified block diagram of the electronics is shown in Figure A-6. The electronics serves to count the number of particles which strike the various solid state detectors and to measure the energy lost

in the detectors. It also interfaces with the spacecraft, transfers the data to spacecraft for telemetry and monitors the performance of the instrument.

Each detector has a set of linear circuits consisting of a charge sensitive amplifier, pulse shaping amplifier and at least one amplitude discriminator. The output from these circuits is a logic pulse from an amplitude discriminator indicating that a pulse exceeding threshold has occurred, and a voltage pulse suitable for pulse height analysis whose amplitude is a function of the charge deposited on a detector. The amplifier noise level is $\leq$ 50 keV (FWHM).

There are two pulse height analyzers (PHA) in the instrument. Each PHA contains a delay line, linear gate, pulse height to pulse width converter and a gated clock. The maximum PHA channel number, determined by the saturation of the amplifiers, is about 1150. The spacecraft telemetry limits the analysis rate to one event, consisting of 2 PHA's, every 1.28 seconds. The two PHA's analyze either coincident pulses from ULET detectors or two single pulses from EECA detectors.

Since there are a total of ten detectors whose outputs are pulse height analyzed, an increase in the noise level of one detector to a point where noise pulses are analyzed will seriously reduce the amount of PHA data obtained from other detectors. To minimize this possibility the PHA's are multiplexed between ULET and EECA so that only ULET pulses are analyzed for a specified

fixed time period and EECA pulses are analyzed the rest of the time. Either sensor can be selected by a ground command to have 75% (48 sequences out of 64) of the PHA time. As a further protection against individual detector failure, there are threshold rate meters monitoring the pulse rates from amplitude discriminators. Whenever the pulse rate from a discriminator exceed the threshold rate, pulses from the detector associated with the particular discriminator are no longer pulse height analyzed and therefore have no adverse affect on the dead times of other, operational detectors. All detectors, except the anticoincidence scintillator PM tubes, have such rate meters. The rate thresholds are set at $\sim$ 50 khz for both ULET detectors and the low energy EECA detector. All other rate thresholds are at 10 khz.

The logic circuits generate the event counting rates and determine when and which pulses are to be pulse height analyzed. The event counting rates are summarized in Table A-II. The basic requirement for positively charged particle counting rates is that the front detector produce a pulse and that neither the B detector nor the anticoincidence cup (A1) produces a pulse. The basic requirement for the electron rate is that both the front detector and the back detector have coincident pulses with no pulse from the anticoincidence cup. (The nominal requirement to record a coincidence or anticoincidence is that the pulses are within 0.6 μsec). Most rates are sectored into four quadrants, according to aspect angle of the rotating spacecraft with respect to the sun, thus providing anisotropy information. The spacecraft spin rate

of 22.9 RPM gives a short time scale for these measurements. For the University of Maryland experiment 12 rates are available, 8 sectored into four quadrants each (SR) and 4 unsectored rates (R). Since a total of 18 rates had to be telemetered some rates are multiplexed as shown in Table A-II.

The PHA requirements for the EECA detector analysis are the same as for positive ion rates with the additional requirements that the analyzer is not busy, the data from registers are not being telemetered, no other detector using the same PHA has a pulse, the PHA is in the EECA instead of ULET mode, the threshold rate from the detector has not been exceeded, and that no high priority event is stored in the register. High priority is assigned to analyses of charge $Q \geq 4$ from P2 detector in one PHA and to analyses of charge $Q \geq 2$ from P7 in the other PHA. When these analyses occur a flag is set and the PHA is inhibited from analyzing other events until the data is telementered. If the priority flag is not set, pulses are analyzed until $\sim$ 2.5 msec before telemetry and the result of last analysis is transmitted. The priority scheme was implemented to obtain PHA data for heavier particles during times of high fluxes. With each PHA event a code identifying which detector produced the pulse and the angular position of spacecraft, to the nearest 45°, at the time the event occurred is also recorded.

To verify the proper operation and to detect any significant drifts in gain or thresholds an in-flight calibrate system is used. For a period of $\sim$ 82 seconds every $\sim$ 3 hours the instrument is commanded by the spacecraft into a calibrate mode. During this

time pulses are applied to the test inputs of each of the charge sensitive amplifiers in turn. The amplitude of these pulses is stepped through a predetermined sequence. For each linear channel pulses of appropriate amplitude are generated so that the overall gain from charge input to channel number output is checked at at least two points. To avoid particle data from interfering with calibration the PHA input is enabled only for $\sim$ 40 μsec and the calibrate input pulse is generated during this time.

Analog voltages which monitor performance of some subsystems are also periodically read out. The temperature at the EECA detector cup and the detector bias voltage are measured once every $\sim$ 82 seconds. The + 3.5 kV supply, the 14.5 kV power supply, ULET proportional counter pressure and the temperature of the thermal valve controlling ULET pressure are monitored every 164 seconds.

Extensive calibrations were performed on the EECA, using both sources and accelerator beams. The first calibrations and design verification have been reported by Spiker [1970]. Additional source calibrations and resolution measurements were reported by Fan et al [1971]. Electron, proton, helium, and nitrogen beams were used to calibrate the IMP-8 experiment, both at the University of Maryland and Goddard Space Flight Center accelerators.

- APPENDIX B -

INSTRUMENT RESPONSE

In order to make full use of the PHA histograms, it is necessary to understand how the instrument responds to a incident spectrum of particles, and to deconvolve the effects of detector and electronic noise, deflection dispersion, electronic thresholds, energy defect, etc.

We first define:

a) $\varepsilon(E)$ = detection efficiency: the probability that a particle incident with energy E strikes the detector active area.

We note that a particle of incident energy E does not, in general, deposit its full energy in the detector, because of non-ionizing nuclear collisions [Campbell and Lin, 1973; Linhard et al, 1963]. The deposited energy E' is related to E by

$$E' = \delta(Z,A,E) \cdot E$$

where δ is the nuclear defect and $\delta \leq 1$. An empirical formula for δ has been derived and used in this analysis:

$$\delta(Z,A,E) = 1 - \{[1-5.12\times10^{-3}(Z+10)\sin(\frac{Z-2}{14}\pi)] \times .03737\sqrt{\frac{Z\ell nZ}{E}}\}$$

with E measured in MeV.

b) $D(E',h)\,dh$ = probability that deposition of an energy E' in the detector gives a pulse height between h and h+dh. This is ideally a Gaussian function of the electronics noise with σ_E:

$$D(E',h) = \frac{1}{\sqrt{2\pi}\,\sigma_E} e^{-(E'-h)^2/2\sigma_E^2}$$

c) $P_t(h)$ = probability that the detector signal h triggers the threshold discriminator, allowing pulse height analysis to take place.

$= P(\frac{h-t}{\sigma_E})$, where t is the threshold and P(x) is the normal probability integral

$$P(x) = \frac{1}{\sqrt{2\pi}} \int_{-\infty}^{x} e^{-u^2/2}\,du$$

We can now define a detector response function [Berger et al, 1969]

$$R(E,h)dh = \varepsilon(E)\, D(\delta \cdot E,h)\, P_t(h)\, dh$$

= probability that an incident particle with energy E is detected and gives rise to an analyzed pulse height between h and h+dh.

If the incident flux of particles is $j(E)$ (particles/cm^2-sr-sec-MeV), we then obtain a pulse height distribution H(h) (particles/sec-MeV),

$$H(h)\,dh = G \int_0^\infty j(E)\, R(E,h)\, dE \cdot dh$$

where G = geometrical factor (cm^2 sterad)

H(h) dh = # of particles detected/second with pulse height between h and h+dh

$$= G \int_0^\infty j(E)\ \varepsilon(E)\ D(\delta\cdot E,h)\ P_t(h)\ dE \cdot dh$$

Going to the discrete case, for pulse height channel n we define

$$H_n \equiv \frac{1}{h_{n+1}-h_n} \int_{h_n}^{h_{n+1}} H(h)\ dh$$

= particles/sec-MeV in channel n with h_n and h_{n+1} the lower and upper energy limits of channel n, respectively.

$$H_n = \frac{1}{h_{n+1}-h_n} \int_{h_n}^{h_{n+1}} dh\ G \int_0^\infty j(E)\ \varepsilon(E)\ D(E\delta,h)\ P_t(h)\ dE$$

$$= \frac{G}{h_{n+1}-h_n} \int_0^\infty dE\ j(E)\ \varepsilon(E) \int_{h_n}^{h_{n+1}} \frac{1}{\sqrt{2\pi}\ \sigma_E} e^{-(E\delta-h)^2/2\sigma_E^2} P\left(\frac{h-t}{\sigma_E}\right) dh$$

$$= \sum_{m=1}^{\infty} \frac{G}{h_{n+1}-h_n} \int_{E_m}^{E_{m+1}} dE\ j(E)\varepsilon(E) \int_{h_n}^{h_{n+1}} \frac{1}{\sqrt{2\pi}\ \sigma_E} e^{-(E\delta-h)^2/2\sigma_E^2} P\left(\frac{h-t}{\sigma_E}\right) dh$$

$$\text{or } H_n \simeq \sum_{m=1}^{N} \frac{G}{h_{n+1}-h_n} \int_{E_m}^{E_{m+1}} dE\ j(E)\ \varepsilon(E)\ \left[P\left(\frac{E\delta-h_n}{\sigma_E}\right) - P\left(\frac{E\delta-h_{n+1}}{\sigma_E}\right)\right] \cdot P\left(\frac{h_n-t}{\sigma_E}\right)$$

Recall that $\varepsilon(E)$ = detection efficiency for incident energy E, or the probability that a particle with incident energy E will strike the detector. For a perfect electrostatic deflection sensor, $\varepsilon(E)$ should be a rectangular window:

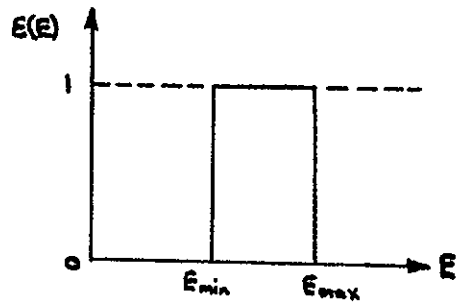

where E_{min} and E_{max} are determined by detector size and position, and particle deflection y:

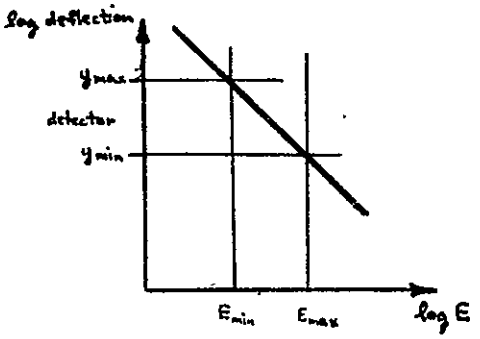

However, in a real sensor, particles of energy E_o are deflected with some finite dispersion about the mean position

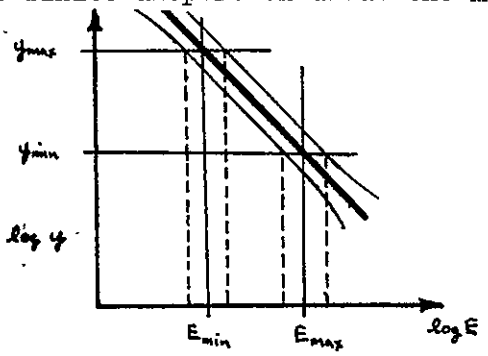

and thus the detection efficiency looks like this:

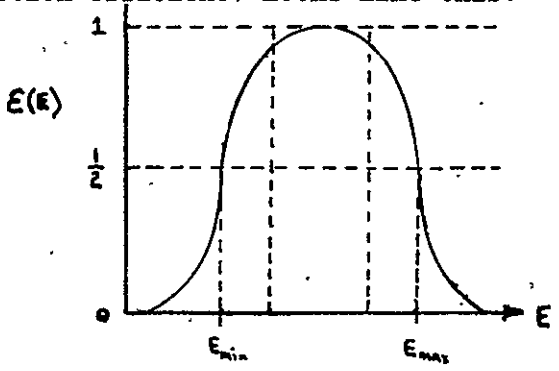

Numerically

$$\varepsilon(E_o) = \int_{y_{min}}^{y_{max}} \frac{1}{\sqrt{2\pi}\,\sigma_D} \, e^{-(y_o-y)^2/2\sigma_D^2} \, dy$$

where $y_o = \frac{kQ}{E_o}$ and $\sigma_D = (.43281 + .00081\, y^2)^{1/2}$ mm [Fan et al, 1971] is the deflection dispersion.

Thus

$$\varepsilon(E_o) = P\left(\frac{y_o - y_{min}}{\sigma_D}\right) - P\left(\frac{y_o - y_{max}}{\sigma_D}\right)$$

or $$\varepsilon(E) = P\left(\frac{\frac{kQ}{E} - y_{min}}{\sigma_D}\right) - P\left(\frac{\frac{kQ}{E} - y_{max}}{\sigma_D}\right)$$

So the pulse height histogram becomes

$$H_n = \sum_{m=1}^{N} \frac{G}{h_{n+1}-h_n} \int_{E_m}^{E_{m+1}} j(E)\left[P\left(\frac{E\delta-h_n}{\sigma_E}\right) - P\left(\frac{E\delta-h_{n+1}}{\sigma_E}\right)\right]$$

$$\left[P\left(\frac{\frac{kQ}{E} - y_{min}}{\sigma_D}\right) - P\left(\frac{\frac{kQ}{E} - y_{max}}{\sigma_D}\right)\right] \; P\left(\frac{h_n - t}{\sigma_E}\right) \, dE$$

particles/(sec MeV) in channel n

If we assume that over the energy interval (E_m, E_{m+1}), $j(E)$ is a constant j_m (a good approximation for small channel widths $E_{m+1} - E_m$)

$$j_m(\bar{E}_m) = \frac{1}{E_{m+1}-E_m} \int_{E_m}^{E_{m+1}} j(E) \, dE \qquad \text{(B-1)}$$

then,

$$H_n = \frac{G}{h_{n+1}-h_n} \sum_{m=1}^{N} j_m \int_{E_m}^{E_{m+1}} \left[P\left(\frac{E\delta-h_n}{\sigma_E}\right) - P\left(\frac{E\delta-h_{n+1}}{\sigma_E}\right)\right]$$

$$\left[P\left(\frac{\frac{kQ}{E} - y_{min}}{\sigma_D}\right) - P\left(\frac{\frac{kQ}{E} - y_{max}}{\sigma_E}\right)\right] P\left(\frac{h_n - t}{\sigma_E}\right) \, dE$$

or $$H_n = \sum_{m=1}^{N} R_{nm} \, j_m$$

where

$$R_{nm} \equiv \frac{G}{h_{n+1}-h_n} \int_{E_m}^{E_{m+1}} \left[P\left(\frac{E\delta-h_n}{\sigma_E}\right) - P\left(\frac{E\delta-h_{n+1}}{\sigma_E}\right)\right] \left[P\left(\frac{\frac{kQ}{E} - y_{min}}{\sigma_D}\right) -\right.$$

$$\left. - P\left(\frac{\frac{kQ}{E} - y_{max}}{\sigma_D}\right)\right] P\left(\frac{h_{n-t}}{\sigma_E}\right) \, dE \qquad \text{(B-2)}$$

Thus

$$\vec{H} = \underset{\sim}{R}\vec{j} \qquad \text{(B-3)}$$

where $\vec{H}$ and $\vec{j}$ are N-dimensional column vectors and $\underset{\sim}{R}$ is an NxN matrix.

- APPENDIX C -

DETERMINATION OF CHARGE STATE ABUNDANCES

Suppose that we have a pulse height histogram $\vec{C}$ which we believe may be represented as a linear superposition of a set of histograms $\vec{P}_j$, where $\vec{P}_j$ is the result of operating on an incident spectrum of particles of type j with the instrument response function $\underset{\sim}{R}$(B-3). As an example, assume that for a particular event a given detector's histogram is a composite of the charge states 5,6,7, and 8. Thus, for a given element (channel) of the histogram C_i,

$$C_i \simeq \alpha_5 P_{5i} + \alpha_6 P_{6i} + \alpha_7 P_{7i} + \alpha_8 P_{8i} \quad . \qquad \text{(C-1)}$$

Our problem is now to determine the most likely α_j.

Since there will be statistical errors σ_i in the C_i, the equality in equation (C-1) will not, in general, hold. Define a difference measure for channel i

$$\Delta_i^2 = \frac{(C_i - \sum_{j=5}^{8} \alpha_j P_{ji})^2}{\sigma_i^2}$$

and a difference sum

$$S = \sum_i \Delta_i^2 = \sum_i \frac{1}{\sigma_i^2} (C_i - \sum_j \alpha_j P_{ji})^2 \quad .$$

By the principle of maximum likelihood, by minimizing this sum, we determine the most likely values of the α_j.

We now perform a standard least squares analysis. At the minimum of S, its variation δS is stationary with respect to changes in the α_K

$$\delta S = 0$$

thus,

$$\frac{\partial S}{\partial \alpha_K} = 0$$

or,

$$\frac{\partial}{\partial \alpha_K} \{ \sum_i \frac{1}{\sigma_i^2} (C_i - \sum_j \alpha_j P_{ji})^2 \} = 0$$

thus,

$$\sum_i [\frac{P_{Ki}}{\sigma_i^2} (C_i - \sum_j \alpha_j P_{ji})] = 0$$

or,

$$\sum_i \frac{P_{Ki} C_i}{\sigma_i^2} = \sum_i (\sum_j \alpha_j P_{ji}) \frac{P_{Ki}}{\sigma_i^2}$$

interchanging the order of summation,

$$= \sum_j \alpha_j (\sum_i \frac{P_{ji} P_{Ki}}{\sigma_i^2})$$

defining

$$\beta_K = \sum_i \frac{P_{Ki} C_i}{\sigma_i^2}$$

and

$$A_{Kj} = \sum_i \frac{P_{ji} P_{Ki}}{\sigma_i^2}$$

we have

$$\beta_K = \sum_j A_{Kj} \alpha_j$$

or

$$\vec{\beta} = \underline{\underline{A}} \vec{\alpha}$$

[which is a polynomial equation in the α_j which may be solved by matrix techniques]

thus

$$\vec{\alpha} = \underset{\sim}{\varepsilon}\,\vec{\beta} \qquad \text{with} \quad \underset{\sim}{\varepsilon} = \underset{\sim}{A}^{-1}; \text{ hence}$$

$$\alpha_j = \sum_K (\varepsilon_{Jk}\ \beta_K) = \sum_k \{\varepsilon_{jK} \sum_i \frac{P_{Ki}\ C_i}{\sigma_i^2}\} \qquad \text{(C-2)}$$

The errors in the α_j are given by [Bevington, 1969] $\sigma^2_{\alpha_j} = \varepsilon_{jj}$.

Unfortunately, the histograms $\vec{P}_j$ are functions of the spectral index of the incident spectrum (see Appendix B), so the solutions of (C-2) are not well defined. However, from rate data it is usually possible to estimate the spectral index and use this estimate to fit histograms. In addition, it has been determined that in most cases there is only a weak dependence of the calculated abundances on spectral index used, and it is these ratios that we are usually interested in.

A computer program, named MSPCT, has been developed which performs all necessary operations on the pulse height data. This program uses as its input data pulse height histograms punched on 80 column computer cards. (These cards are punched by another program, which is responsible for accumulating the PHA data for specified time periods from the experiment encyclopedia tapes.) MSPCT calls subroutine BSUB to normalize and subtract a quiet time "background" histogram from the histogram of the time period of interest. The background histogram may be normalized in one of several ways. Usually, the histogram is normalized to absolute flux levels. During time periods when the flux of high-energy protons is high the background counting rate changes, and it has been found that this "absolute flux" method does not give very reliable results.

In these cases, it is possible to specify a certain energy range over which no "real" events are expected. BSUB then calculates the normalization constant which will minimize excess counts over background in this range. The third method is used when it is believed that the background spectrum in a detector has some simple form--a power law in energy, for example. The measured histogram then consists of this power law background plus, over some energy range, a number of "real" events. By fitting a polynomial to the histogram exterior to those areas where genuine events are expected, the resultant fitted background curve may be used to correct the observed histogram. The program then reads in the appropriate instrument response matrices from magnetic tape (these matrices are generated by a subroutine named, logically enough, MATRIX). The routine calls a subroutine which generates an "incident" histogram of the form (B-1) for the input spectral index, and performs the matrix multiplication of this histogram and the response matrix to generate the predicted instrument response histogram $\vec{P}_j$. The matrix A is generated and inverted, and the α_j are computed. Both the data histogram (before and after background correction) and the computed superposition of $\vec{P}_j$ may be plotted. Finally, charge state abundance ratios and a "goodness of fit" measure are computed.

In addition, the routine has the ability to generate and plot pulse height histograms which represent "predicted" instrument response to an input mix of charge state abundances and spectral indices. The dashed curves of Figure 3-2 were generated in this manner.

SELECTED REFERENCES

Ahluwalia, H. S. (1971). Proc. 12th Int'l Conf. Cosmic Rays (Hobart), 2, 468.

Allen, C. W. (1963). Astrophysical Quantities, Univ. of London, (Athlone Press), London.

Allen, J. W. and A. K. Dupree (1967). Scientific Report No. 24, Harvard College Observatory.

Aller, L. H. (1971). Atoms, Stars, and Nebulae, Harvard Univ. Press, Boston.

Anderson, K. A. (1969). Solar Physics, 6, 111.

Anderson, K. A. (1972). Solar Physics, 27, 442.

Armstrong, T. P. and S. M. Krimigis (1971). J. Geophys. Res., 76, 4230

Armstrong, T. P., S. M. Krimigis, D. V. Reames, and C. E. Fichtel (1972). J. Geophys. Res., 77, 3607.

Bame, S. J., A. J. Hundhausen, J. R. Asbridge, and I. B. Strong (1968). Phys. Rev. Lett., 20, 393.

Bame, S. J., J. R. Asbridge, A. J. Hundhausen, and M. D. Montgomery (1970). J. Geophys. Res., 75, 6360.

Berger, M. J., S. M. Seltzer, S. E. Chappell, J. C. Humphreys, and J. W. Motz (1969). Technical Note #489, National Bureau of Standards.

Bertsch, D. L., C. E. Fichtel, and D. V. Reames (1969). Astrophys. J. (lett.), 157, L53.

Bertsch, D. L., C. E. Fichtel, and D. V. Reames (1972). Astrophys. J., 171, 169.

Betz, H. D. (1972) Rev Mod Phys., 44, 465.

Bevington, P. R. (1969). Data Reduction and Error Analysis for the Physical Sciences, McGraw-Hill, New York.

Biswas, S., and C. E. Fichtel (1964). Astrophys. J., 139, 941.

Biswas, S., and C. E. Fichtel (1965). Sp. Sci. Rev., 4, 709.

Boischot, A. (1974). Coronal Disturbances, IAU Symp. No. 57, p. 423, (G. Newkirk, ed.), D. Reidel, Dortrecht.

Braddy, D., J. Chan, and P. B. Price (1973). Phys. Rev. Lett., 30. 669.

Campbell, R. D. and R. P. Lin (1973). Rev. Sci. Inst., 44, 1510.

Cartwright, B. G. and A. Mogro-Compero (1972). Astrophys. J. (lett,), 177, L43.

Cox, D. P. and W. H. Tucker (1969). Astrophys. J., 157, 1157.

Craig, I. J. D., J. L. Culhane, K. J. Phillips, and J. Vesecky (1973). High Energy Phenomena in the Sun, NASA preprint X-693-73-193 (ed. R. Ramaty and R. Stone), p. 276.

Crawford, H. J., P. B. Price, and J. D. Sullivan (1972). Astrophys. J. (lett.), 175, L149.

Crawford, H. J., P. B. Price, B. G. Cartwright, and J. D. Sullivan (1975). Astrophys. J., 195, 213.

Fan, C. Y., M. Pick, R. Pyle, J. A. Simpson, and D. R. Smith (1968). J. Geophys. Res., 73, 1555.

Fan, C. Y., G. Gloeckler, and E. Tums (1971). Proc. 12th Int'l Conf. Cosmic Rays (Hobart), 4, 1602.

Fan, C. Y., G. Gloeckler, and D. Hovestadt (1975). Phys. Rev Lett., 34, 495.

Fichtel, C. E. and D. E. Guss (1961). Phys. Rev. Lett., 6, 495.

Flower, D. R. and H. Nussbaumer (1974). Astron. and Astrophys., 31, 353.

Ginzberg, V. L. and S. I. Syrovatskii (1964). The Origin of Cosmic Rays, MacMillian, N. Y.

Gloecker, G., C. Y. Fan and D. Hovestadt (1973). Proc. 13th Int'l Conf. Cosmic Rays (Denver)

Gloeckler, G., R. Sciambi, C. Y. Fan, and D. Hovestadt (1974). EOS, 55, 385.

Gloeckler, G., R. K. Sciambi, C. Y. Fan, and D. Hovestadt (1975a). Proc. 14th Int'l Cosmic Ray Conf. (Munich), 5, 1576.

Gloeckler, G., D. Hovestadt, O. Vollmer, and C.Y. Fan (1975b). Astrophys. J. (lett.), 200, L45.

Gloeckler, G., R. Sciambi, C.Y. Fan, and D. Hovestadt (1975c). Bull. Am. Astron. Soc., 7, 536.

Gold, R. E., S. M. Krimigis, E. C. Roelof, A. S. Krieger, and J. T. Nolte (1975). Proc. 14th Int'l Cosmic Ray Conf. (Munich), 5, 1710.

Holzer, T. E. and W. I. Axford (1970). J. Geophys. Res., 75, 6354.

Hovestadt, D. and O. Vollmer (1971). Proc. 12th Int'l Conf. Cosmic Rays (Hobart), 4, 1608.

Ipavich, F. M. (1974). Geophys. Res. Lett., 1, 149.

Itikawa, Y. and O. Aono (1965). Phys. Fluids, 9, 1259.

Jokipii, J. R. and A. J. Owens (1975). J. Geophys. Res., 80, 1209.

Jordon, C. (1969). Mon. Not. Roy. Astron. Soc., 142, 501.

Kafatos, M. C. and W. H. Tucker (1972). Astrophys. J., 175, 837.

Kahler, S. W. (1973). High Energy Phenomena on the Sun, NASA Preprint X-693-73-193 (ed. R. Ramaty and R. Stone), p. 124.

Kane, S. R. (1973). High Energy Phenomena on the Sun, NASA Preprint X-693-73-193 (ed. R. Ramaty and R. Stone), p. 55.

Kane, S. R. (1974). Coronal Disturbances, IAU Symp. No. 57, p. 105 (G. Newkirk, ed.), D. Reidel, Dortrecht.

Krimigis, S. M. (1973). High Energy Phenomena on the Sun, NASA Preprint X-693-73-193 (ed. R. Ramaty and R. Stone). p. 478.

Krimigis, S. M. and P. Verzariu (1971). J. Geophys. Res., 76, 792.

Lange, J. and F. Scherb (1970). J. Geophys. Res., 75, 6350.

Lin, R. P., R. E. McGuire, and K. A. Anderson (1974). Coronal Disturbances, IAU Symp. No. 57 (G. Newkirk, ed.), p. 461 D. Reidel, Dortrecht.

Linhard, J., M. Scharff and H. E. Schiott (1963). Kgl. Danske Videnskab Selskab., Mat.-Fys. Medd., 33, 14.

Lupton, J. E. and E. C. Stone (1973). J. Geophys. Res., 78, 1007.

Ma Sung, L. S., M. A. I. Van Hollebeke, and F. B. McDonald (1975). Proc. 14th Int'l Cosmic Ray Conf. (Munich), 5, 1767.

McDonald, F. B. and U. D. Desai (1971). J. Geophys. Res., 76, 808.

McGuire, R. E., R. P. Lin, and K. A. Anderson (1975). Proc. 14th Int'l Cosmic Ray Conf. (Munich), 5, 1785

Mogro-Compero, A. and J. A. Simpson (1972). Astrophys. J. (lett.), 171, L5.

Nakada, M. P. (1969). Solar Physics, 7, 302.

Newkirk, G. (1973). High Energy Phenomena on the Sun, NASA Preprint X-693-73-193 (ed. R. Ramaty and R. Stone), p. 453.

Parker, E. N. (1965). Planetary Sp. Sci., 13, 9.

Peterson, L. E., D. Datlowe, and D. McKenzie (1973). High Energy Phenomena on the Sun, NASA Preprint X-693-73-193 (ed. R. Ramaty and R. Stone), p. 132.

Price, P. B., I. Hutcheson, R. Cowsik, and D. J. Barber (1971). Phys. Rev. Lett., 26, 916.

Roelof, E. C., R. E. Gold, S. M. Krimigis, A. S. Krieger, J. T. Nolte, P. S. McIntosh, A. J. Lazarus, and J. D. Sullivan (1975). Proc. 14th Int'l Conf. Cosmic Rays (Munich), 5, 1704.

Sakurai, K. (1974). Physics of Solar Cosmic Rays, Univ. of Tokyo Press, Tokyo.

Sakurai, K. (1975). Proc. 14th Int'l Cosmic Ray Conf. (Munich), 5, 1552.

Sciambi, R., G. Gloeckler, C. Y. Fan, and D. Hovestadt (1974). EOS, 55, 1165.

Simnett, G. M. (1971). Solar Physics, 20, 448.

Simnett, G. M. (1972). Solar Physics, 22, 189.

Simnett, G. M. (1973). High Energy Phenomena on the Sun, NASA Preprint X-693-73-193 (ed. R. Ramaty and R. Stone), p. 503.

Simnett, G. M. and S. S. Holt (1971). Solar Physics, 16, 208.

Spiker, J. B. (1970). University of Maryland Technical Report #71-022.

Strauss, F. M. and M. D. Papagiannis (1971). Astrophys. J., 164, 369.

Sturrock, P. A. (1973). High Energy Phenomena on the Sun, NASA Preprint X-693-73-193, (ed. R. Ramaty and R. Stone), p. 3.

Sullivan, J. D. and P. B. Price (1973). Proc. 13th Int'l Conf. Cosmic Rays (Denver), 2, 1470.

Takakura, T. (1967). Solar Physics, 1, 304.

Teegarden, B. J., T. T. von Rosenvinge, and F. B. McDonald (1973). Astrophys. J., 180, 571.

Van Allen, J. A., P. Venkatarangan, and D. Venkatesan (1974). J. Geophys. Res., 79, 1.

Venkatarangan, P. and L. J. Lanzerotti (1975). J. Geophys. Res., 80, 1744.

Verzariu, P., and S. M. Krimigis (1972). J. Geophys. Res., 77, 3985.

Wentzel, D. G. (1965). Astrophys. J., 137, 135.

Wild, J. P. and S. F. Smerd (1972). Ann. Rev. Astron. and Astrophys., 10, 159.

Table 3-I

Characteristics of 10 Solar Particle Events

Event Date	PHA Data	Flare Time	Flare Importance	Approx. Location
73/11/4	11/4 :0000 to 11/5 :1159	11/3 :0012	2N	S18W85
74/1/25	1/25:1200 to 1/27:0300	1/22:1915	1N	N09W60
74/5/14	5/14:0700 to 5/15:0500	5/13:2118	2N	S13W66
74/5/31	5/31:0000 to 5/31:1200	5/29:1200	1B	S15W63
74/6/10	6/9 :0000 to 6/11:1200	6/8 :1450	3N	S13W64
74/6/22	6/22:0000 to 6/24:2400	6/21:1822	1F	S20W27
74/6/26	6/26:0000 to 6/29:1200	6/24:1515	1N	S13W69
74/7/4	7/5 :1200 to 7/8 :2400	7/4 :1338	2B	S16W03
74/10/14	10/12:1200 to 10/15:2400	10/11:1010	1B	N13W03
74/11/8	11/8 :0000 to 11/10:2400	11/6 :0220	1B	S12W75

Table 3-II

Ionization State Abundances

Date	C^{+5}/C	C^{+6}/C	O^{+6}/O	O^{+7}/O	O^{+8}/O	Fe^{+10}/Fe	Fe^{+11}/Fe	Fe^{+12}/Fe	Fe^{+13}/Fe
73/11/4	0.25 ±.04	0.74 ±.04	0.72 ±.05	0.20 ±.05	0.07 ±.03				
74/1/25	0.31 ±.06	0.68 ±.07	0.69 ±.04	0.16 ±.06	0.05 ±.06				
74/5/14	0.23 ±.03	0.76 ±.05	0.66 ±.05	0.33 ±.04	0.00 ±.03	0.14 ±.04	0.30 ±.06	0.34 ±.07	0.20 ±.05
74/5/31	0.20 ±.05	0.79 ±.06	0.70 ±.07	0.23 ±.05	0.06 ±.04				
74/6/10	0.17 ±.02	0.82 ±.05	0.81 ±.07	0.16 ±.06	0.02 ±.01				
74/6/22	0.34 ±.07	0.65 ±.02	0.73 ±.06	0.20 ±.03	0.06 ±.05				
74/6/26	0.18 ±.02	0.81 ±.07	0.67 ±.04	0.21 ±.06	0.08 ±.04				
74/7/4	0.28 ±.06	0.71 ±.03	0.68 ±.05	0.27 ±.04	0.04 ±.06				
74/10/14	0.26 ±.05	0.73 ±.04	0.77 ±.03	0.21 ±.05	0.01 ±.02				
74/11/8	0.22 ±.04	0.77 ±.06	0.71 ±.04	0.15 ±.06	0.13 ±.08				
All Events	0.24 ±.04	0.75 ±.05	0.71 ±.05	0.22 ±.05	0.05 ±.04	0.14 ±.04	0.30 ±.06	0.34 ±.07	0.20 ±.05
Solar Wind[a]			0.77	≤0.15		0.24	0.21	0.14	
Solar Corona[b]	0.186	0.813	0.759	0.234	0.008	0.141	0.257	0.316	0.155

a) Bame et al [1968]

b) Jordan [1969] for $T_e = 1.58 \times 10^6$ °K

Table 3-III

Composition and Spectrum Data for Ten Solar Particle Events

Event Averaged Values

Date	Relative Abundance α/CNO (40 keV/nuc)	Alpha Spectral Index γ_α 40-80 keV/nuc	CNO Spectral Index γ_{CNO} 20-40 keV/nuc	proton flux $(cm^2\text{-sr-sec-MeV})^{-1}$ 130-220 keV	ULET Abundances (600 keV/nuc) C/O	Fe/O
73/11/4	14	1.9 ± 0.2	1.1 ± 0.4	340	0.43	<0.01
74/1/25	17	2.4 ± 0.3	0.9 ± 0.5	1000	1.3	0.14
74/5/14	2	$2.8 \pm .04$	2.4 ± 0.3	65	0.39	2.5[a]
74/5/31	17	2.6 ± 0.3	1.5 ± 0.4	100	0.27	0.09
74/6/10	3	0.4 ± 0.5[b]	0.15 ± 0.5	1200	0.46	0.20
74/6/22	7	2.7 ± 0.4	2.0 ± 0.5	200	0.64	<0.01
74/6/26	14	3.1 ± 0.5	1.1 ± 0.5	250	0.79	0.16
74/7/4	16	1.8 ± 0.3	-0.2 ± 0.5	12000	0.40	0.36
74/10/14	20	3.3 ± 0.4	1.2 ± 0.5	230	0.31	0.17
74/11/8	8	1.7 ± 0.2	-0.5 ± 0.75	2500	0.46	0.05

a) "iron rich" [Gloeckler et al, 1975b]

b) alpha turndown observed in this event

TABLE A-1

Detector Energy-Charge Ranges

Detector[a]	Charge Threshold	Energy Range	Geometrical Factor (cm^2 sr)
P1	$Q \geq 6$	37-55 keV/Q	.02
P2	$Q \geq 2$	65-100 keV/Q	.03
P2',[b]	$Q \geq 4$	65-100 keV/Q	.03
P3	$Q \geq 1$	130-210 keV/Q	.03
P4	$Q \geq 1$	160-230 keV/Q	.02
P5	$Q \geq 1$	background $\geq$ 160 keV	---
P6	$Q \geq 1$	390-600 keV/Q	.018
P6',[c]	$Q \geq 4$	390-600 keV/Q	.018
P7	$Q \geq 1$	550-900 keV/Q	.03
P7',[b,c]	$Q \geq 2$	550-900 keV/Q	.03
P8	$Q \geq 1$	740-1200 keV/Q	.018
N·B	electrons	600-860 keV	.018
A1	protons	$\geq$ 18 MeV	1100.
A2	protons	$\geq$ 6 MeV	675.

[a] Discriminator rates for all detectors are generated and read out through telemetry. In addition, all detector signals except N·B and A1 and A2 are pulse height analyzed.

[b] Denotes pulse height analysis priority event.

[c] For detectors listed twice the prime indicates a higher threshold for rate or pulse height analysis.

TABLE A-II

Event Counting Rates

Rate	Multiplex Step	Time in Mux Step (sec)	Logical Equation	Accumulation time/ readout (sec).	Period between readouts (sec)
R1			$P4 \cdot (\overline{B}+BRD) \cdot \overline{A1}$	5.12	5.12
R2			$P7' \cdot (\overline{B}+BRD) \cdot \overline{A1}$	5.12	5.12
R3			$P2' \cdot (\overline{B}+BRD) \cdot \overline{A1}$	5.12	5.12
R4	0	61.44	A1	10.24	10.24
	1	20.48	A2	10.24	10.24
	2	61.44	B	10.24	10.24
	3	20.48	A2	10.24	10.24
SR1	0	61.44	No rate (sync)	--	20.48
	1	20.48	$P5 \cdot (\overline{B}+BRD) \cdot \overline{A1}$	4.59/sector	20.48
	2	81.92	$P7 \cdot (\overline{B}+BRD) \cdot \overline{A1}$	4.59/sector	20.48
	3	81.92	$P6 \cdot (\overline{B}+BRD) \cdot \overline{A1}$	4.59/sector	20.48
	4	81.92	$P3 \cdot (\overline{B}+BRD) \cdot \overline{A1}$	4.59/sector	20.48
SR2			$P6' \cdot (\overline{B}+BRD) \cdot \overline{A1}$	4.59/sector	20.48
SR3			$N \cdot (\overline{B}+BRD) \cdot \overline{A1}$	4.59/sector	20.48
SR4	0	61.44	$D2 \cdot \overline{A2}$	4.59/sector	20.48
	1	20.48	$D1 \cdot \overline{A2}$	4.59/sector	20.48
SR5			$P8(\overline{B}+BRD) \cdot \overline{A1}$	4.59/sector	20.48
SR6			$D1 \cdot D2 \cdot \overline{A2}$	4.59/sector	20.48
SR7			$P2(\overline{B}+BRD)\overline{A1}$	4.59/sector	20.48
SR8			$P1(\overline{B}+BRD)\overline{A1}$	4.59/sector	20.48

NOTE: BRD true when B threshold rate is exceeded.

FIGURE CAPTIONS

Figure 2-1 Ionic charge state resolution of IMP-8 detector P3. This detector nominally responds to ions with energies in the range 130 to 220 keV per charge. Note that, while the energy bands for ions of charge 5, 6, 7, and 8 overlap, there is a range where only ions of charge 5 appear. By means of a simple iteration procedure, it is possible to calculate abundances for each ionic charge state.

Figure 2-2 Cross section of the Max-Planck-Institut's Ultra Low Energy Telescope (ULET) as flown on IMP-8. The ΔE element is a thin-window flow through proportional counter.

Figure 2-3 The IMP-8 spacecraft orbit in the solar ecliptic (SE) coordinate system, plotted from ephemeris tapes for early May, 1974. The upper panel shows the distance from the earth-sun line $\sqrt{Y_{SE}^2 + Z_{SE}^2}$ vs distance from the earth (in earth radii) along the earth-sun line (X_{SE}). The nominal position of the earth's bowshock and magnetopause are shown. The lower left-hand panel shows the projection of the orbit into the ecliptic (X_{SE}-Y_{SE}) plane. The sun-earth-vehicle (SEV) angle is indicated. The lower right-hand panel shows the projection in the Y_{SE}-Z_{SE} plane, normal to the ecliptic. Courtesy of Dr. J.D. Sullivan, MIT.

Figure 3-1 a) Uncorrected pulse-height histogram from detector P3. The smoothed, measured background distribution is shown as a dashed line.
b) Pulse-height histogram corrected for background. Note the characteristic triple-peaked form of the distribution. The rightmost peak corresponds to carbon and oxygen in the charge group 5-8, or iron with $8 \leq Q \leq 12$.

Figure 3-2 a) Corrected pulse-height histogram from detector P3 for the "iron rich" event of Gloeckler et al [1975b]. The dashed curve represents a computed fit of ionic charges 8 to 12 of iron and 5, 6, 7, and 8 of carbon and oxygen to the observed distribution.
b) The same histogram as a). Here it has been assumed that all iron is Fe^{+26}. The required Fe^{+26} peak (dashed curve) is clearly not present.

Figure 3-3 Measured iron and helium fluxes from ULET and the EECA during the 1974 May 14 event. Iron has been assumed to have ionic charges 8-12 in the EECA. The agreement between the two experiments is very good.

Figure 3-4 Fluxes of 40, 80, and 150 keV per charge heavy ions vs time in the 1974 July 4 event. Note that the fluxes from the two lowest energy channels overlap, indicating a strong bend-down in the energy spectrum.

Figure 3-5 The helium/medium-group ratio at 80 keV per charge plotted as a function of time, for the July 4 event. During both large particle increases in Figure 3-4, the ratio starts low and increases throughout the event.

Figure 3-6 The event-averaged energy spectrum of helium during the 1974 July 4 event.

Figure 3-7 The event-averaged energy spectrum for the charge 5-8 group during the 1974 July 4 event. Note the spectral flattening below 100 keV per nucleon.

Figure 3-8 The mean ionic charge states of carbon and oxygen as a function of energy for the 1974 July 4 event. There is no statistically significant variation with energy.

Figure 3-9 Proton, helium, and medium-group differential energy spectra for the 1974 June 10 event. In this event, both the helium and the medium-group spectra show a flattening at lower energies.

Figure 3-10 The mean ionic charge states of carbon and oxygen as a function of energy for the 1974 June 10 event. Again, there is no significant energy dependence.

Figure 3-11 Time variation of the spectral index γ ($J \sim E^{-\gamma}$) for heavy ions between 40 and 80 keV per charge during the 1974 June 10 event. The spectral index, after velocity dispersion effects no longer are important, remains at a low, more-or-less constant value.

Figure 3-12 The helium/medium-group ratio at 80 keV per charge, for the June 10 event. The trend is for the ratio to increase with time during the event.

Figure 3-13 Proton, helium, and medium-group differential energy spectra for the 1974 June 22 event. This event shows no spectral flattening (compare to Figures 3-9 and 3-14).

Figure 3-14 Proton, helium, and medium-group differential energy spectra for the 1974 November 8 event. Here a strong bend-down appears in the heavier nuclei, but there is none apparent in the helium spectrum.

Figure 3-15 Medium-group "event-averaged" spectral index (40-80 keV per charge) vs "event-averaged" proton flux (130-220 keV). Note the strong correlation of (-spectral index) with event size.

Figure 4-1 The expected charge states of carbon, oxygen, and iron as a function of temperature [Jordan, 1969], with the experimental results shown as a dashed line. For the theoretical points, a bar represents the temperature range over which more than half of the ions have that ionization state; a point represents the temperature at which that species is most abundant. After Nakada [1969].

Figure 4-2 The relative ionization loss rate term $\left[\frac{\mathrm{erf}(u)}{u^2} - 1.13\frac{\exp(-u^2}{u}\right.$ plotted vs $u = 79.5\sqrt{\frac{E_i}{T_e}}$. The function has the expected form for ion velocities near the plasma electron velocity.

Figure 4-3 Results of model ionization loss calculations for various ions. All species were initially equally abundant, with a power law spectrum $J \sim E^{-3}$. The particles were released at 1.02 $R_\odot$, stored at 1.4 $R_\odot$ ($n_e = 10^8$ cm^{-3}) for 1000 seconds, and then propagated to 10 $R_\odot$. The corona has been assumed to be isothermal, with an electron temperature of 1.5×10^6 ^{0}K.

Figure 4-4 The same as Figure 4-3, except that the initial spectrum was $J \sim E^{-2}$. The bending occurs at the same energy in both cases.

Figure A-1 Cross section of the University of Maryland Electrostatic Energy-Charge Analyzer, as flown on the IMP-8 spacecraft.

Figure A-2 Energy ranges of the IMP-8 experiment detectors for various incident ionic charges.

Figure A-3 (Upper panel) Front view of the IMP-8 detector array. This array consists of eight 100 μ totally depleted surface barrier detectors and one 1000 μ Si(Li) detector (N).
(Lower panel) Back view of the IMP-8 detector array. Here groups B1 and B2 are shown. Electrically, all of these detectors are wired in parallel and collectively referred to as B.

Figure A-4 The collimator assembly. The stack consists of 270 thin aluminum plates, mounted to a curved magnesium frame.

Figure A-5 The innermost and outermost collimator plates. Proceding from the outermost to the innermost plate the slots become shorter and the row spacing smaller. This creates a series of vertically converging radial tunnels when the plates are assembled to the frame.

Figure A-6 A simplified block diagram of the EECA instrument as flown on IMP-8. All linear and logic circuits are shown, which are required for pulse-height analysis, rate generation, and internal calibration.

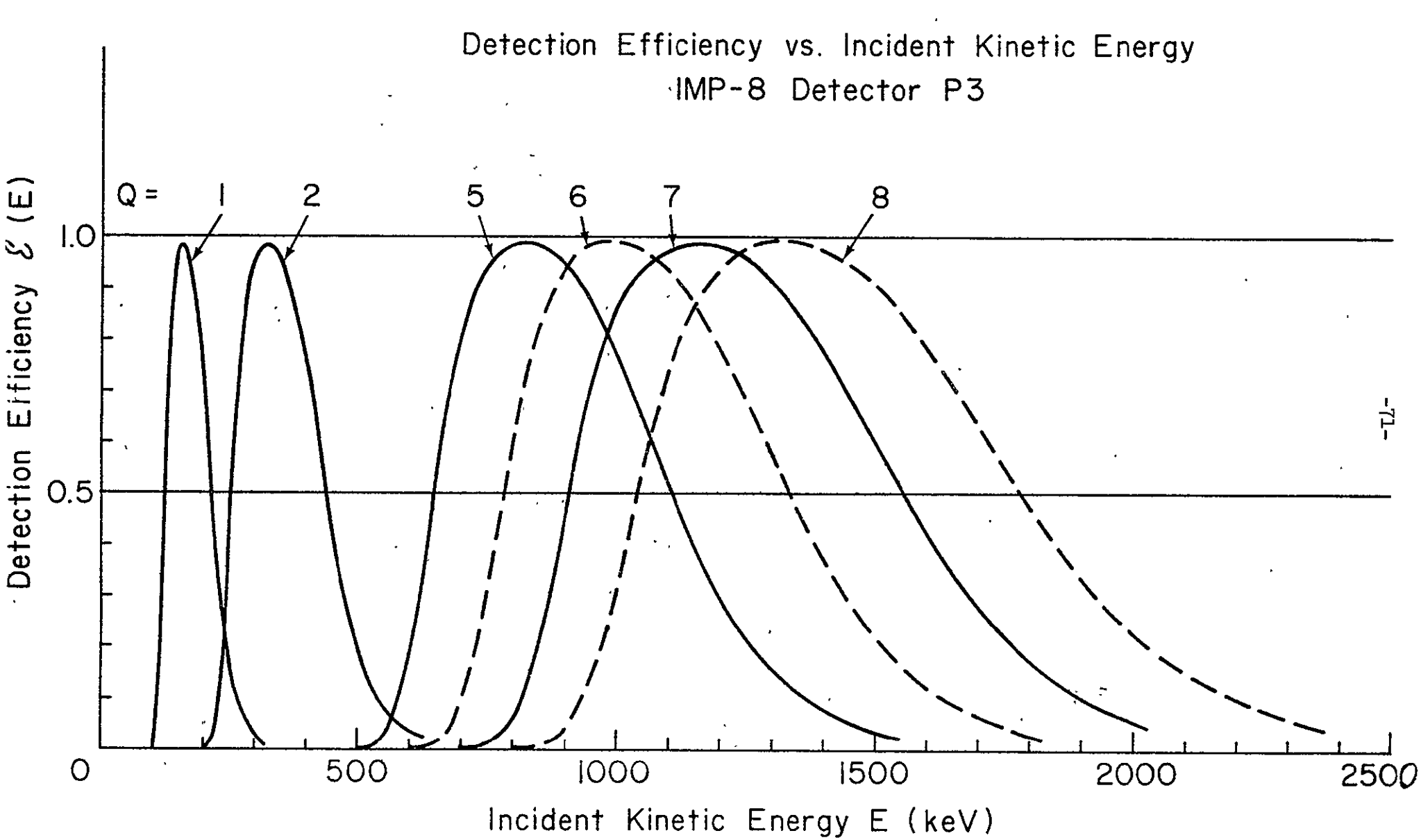
Detection Efficiency vs. Incident Kinetic Energy
IMP-8 Detector P3
Q = 1
2
5
6
7
8
Detection Efficiency ℰ (E)
1.0
0.5
0
500
1000
1500
2000
2500
Incident Kinetic Energy E (keV)

FIGURE 2-1

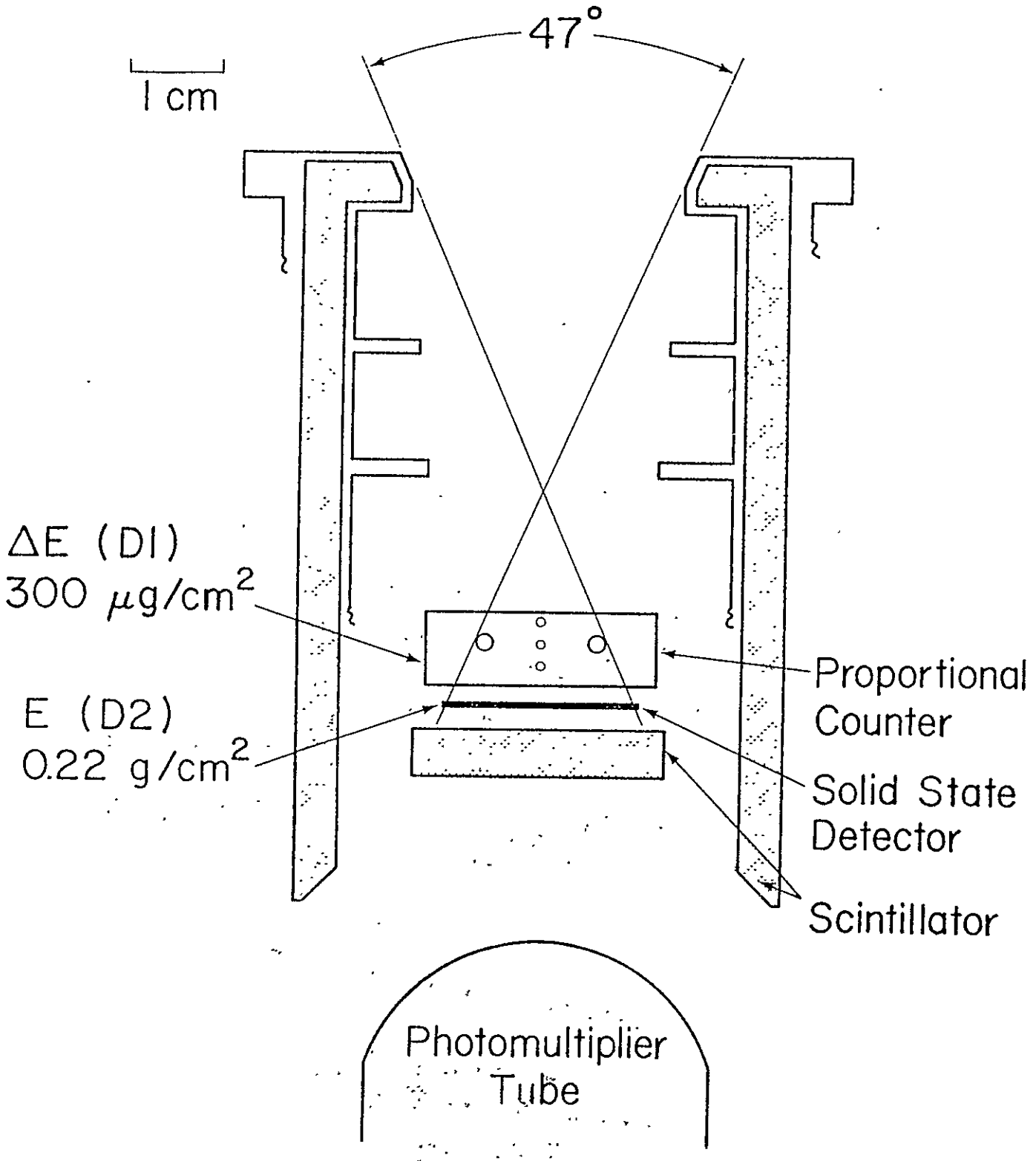
ULET
Univ of Maryland / MPI Experiment
IMP 8
47°
1 cm
ΔE (D1)
300 μg/cm²
E (D2)
0.22 g/cm²
Proportional Counter
Solid State Detector
Scintillator
Photomultiplier Tube

FIGURE 2-2

MIT 12/09/74

IMP 8 TRAJECTORY. ASCENDING NODE 17

FROM MAY 8 TO MAY 20 1974

DAYS 128 THRU 140

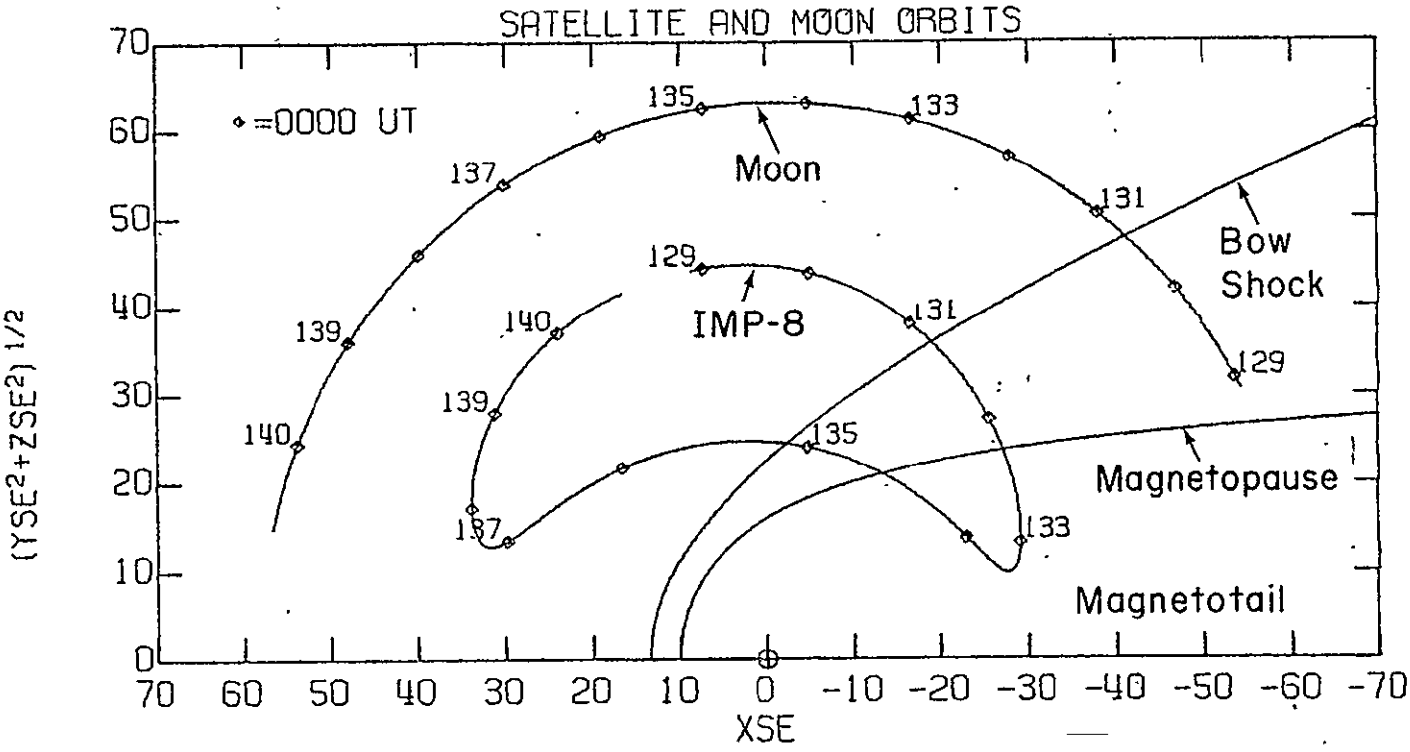

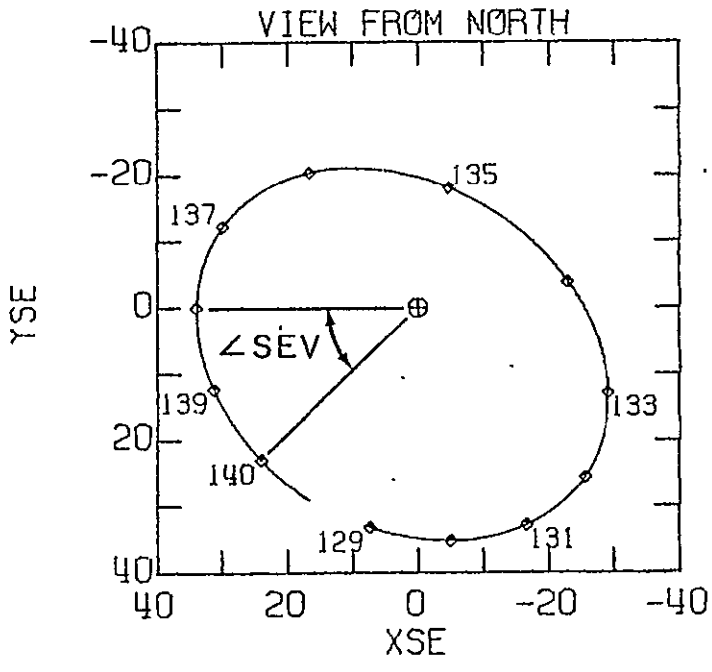

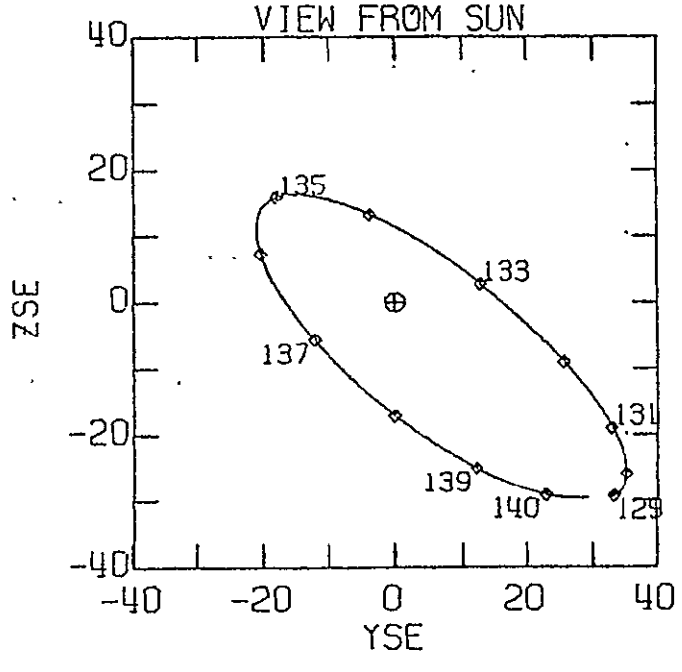

FIGURE 2-3

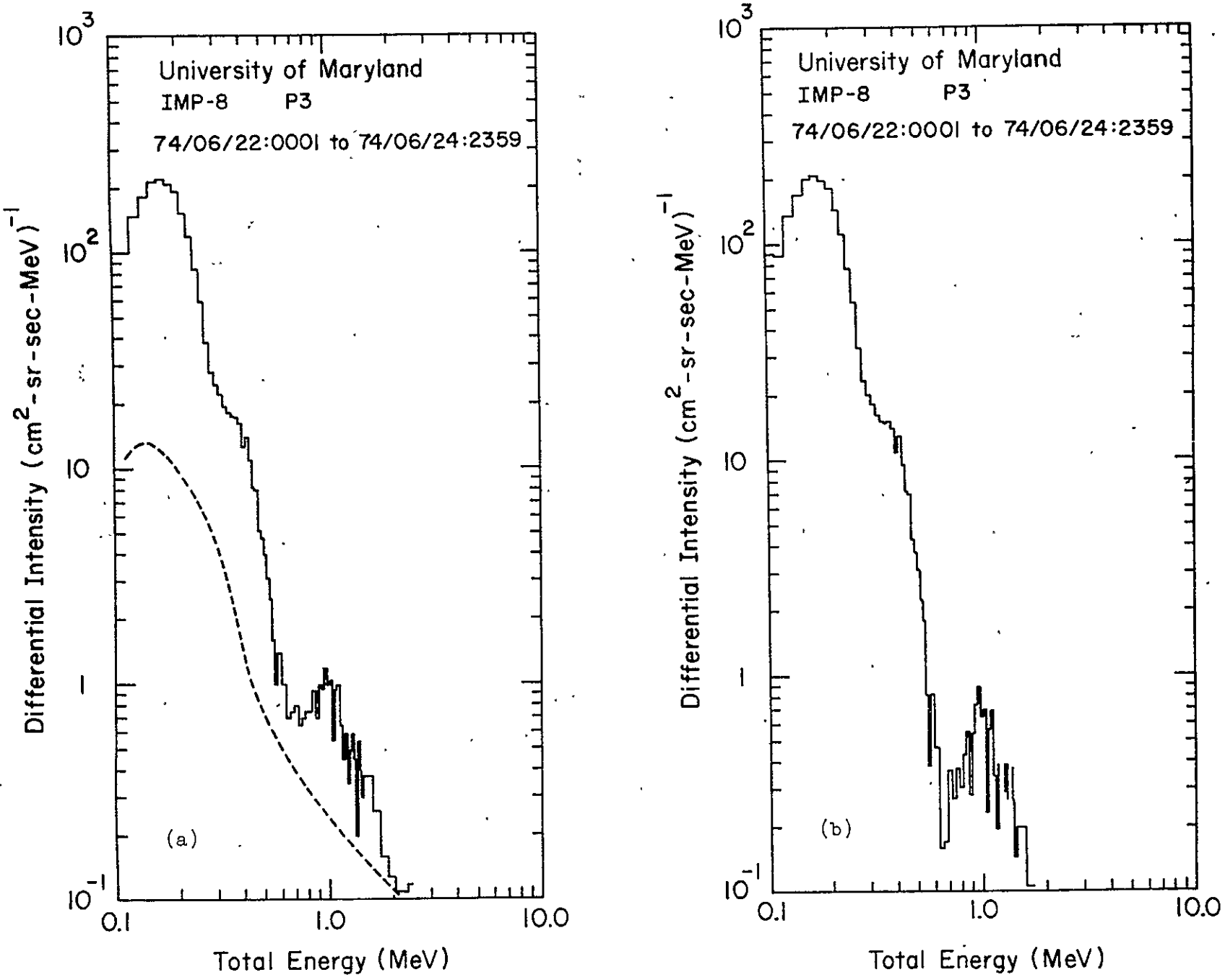
University of Maryland
IMP-8 P3
74/06/22:0001 to 74/06/24:2359
Differential Intensity (cm^2-sr-sec-MeV)$^{-1}$
Total Energy (MeV)
(a)
(b)
10^3
10^2
10
1
10^{-1}
0.1
1.0
10.0

FIGURE 3-1

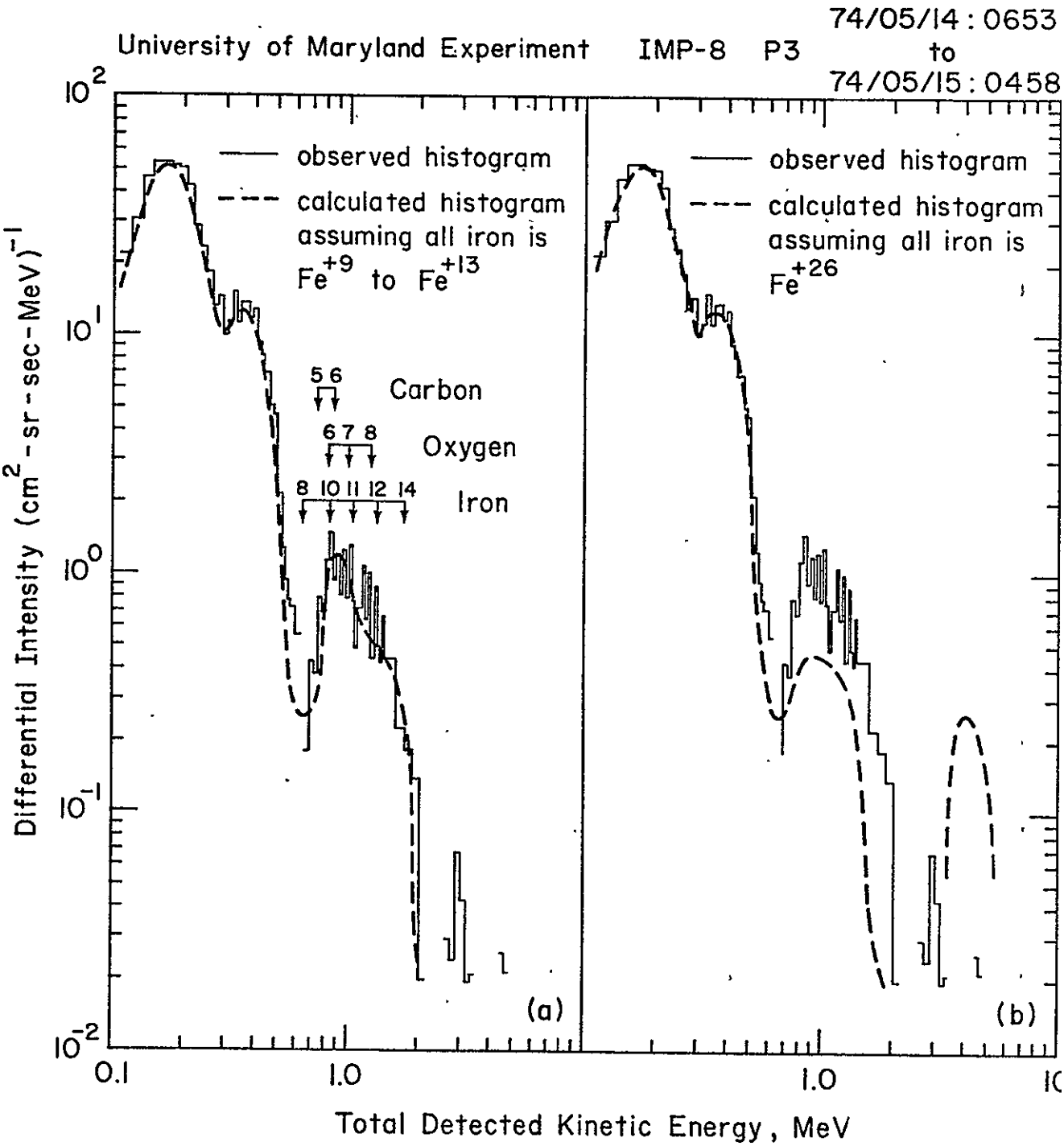
University of Maryland Experiment IMP-8 P3
74/05/14 : 0653
to
74/05/15 : 0458
observed histogram
calculated histogram assuming all iron is Fe+9 to Fe+13
observed histogram
calculated histogram assuming all iron is Fe+26
5 6 Carbon
6 7 8 Oxygen
8 10 11 12 14 Iron
(a)
(b)
Differential Intensity (cm2-sr-sec-MeV)-1
Total Detected Kinetic Energy, MeV
10^2
10^1
10^0
10^-1
10^-2
0.1
1.0
1.0

FIGURE 3-2

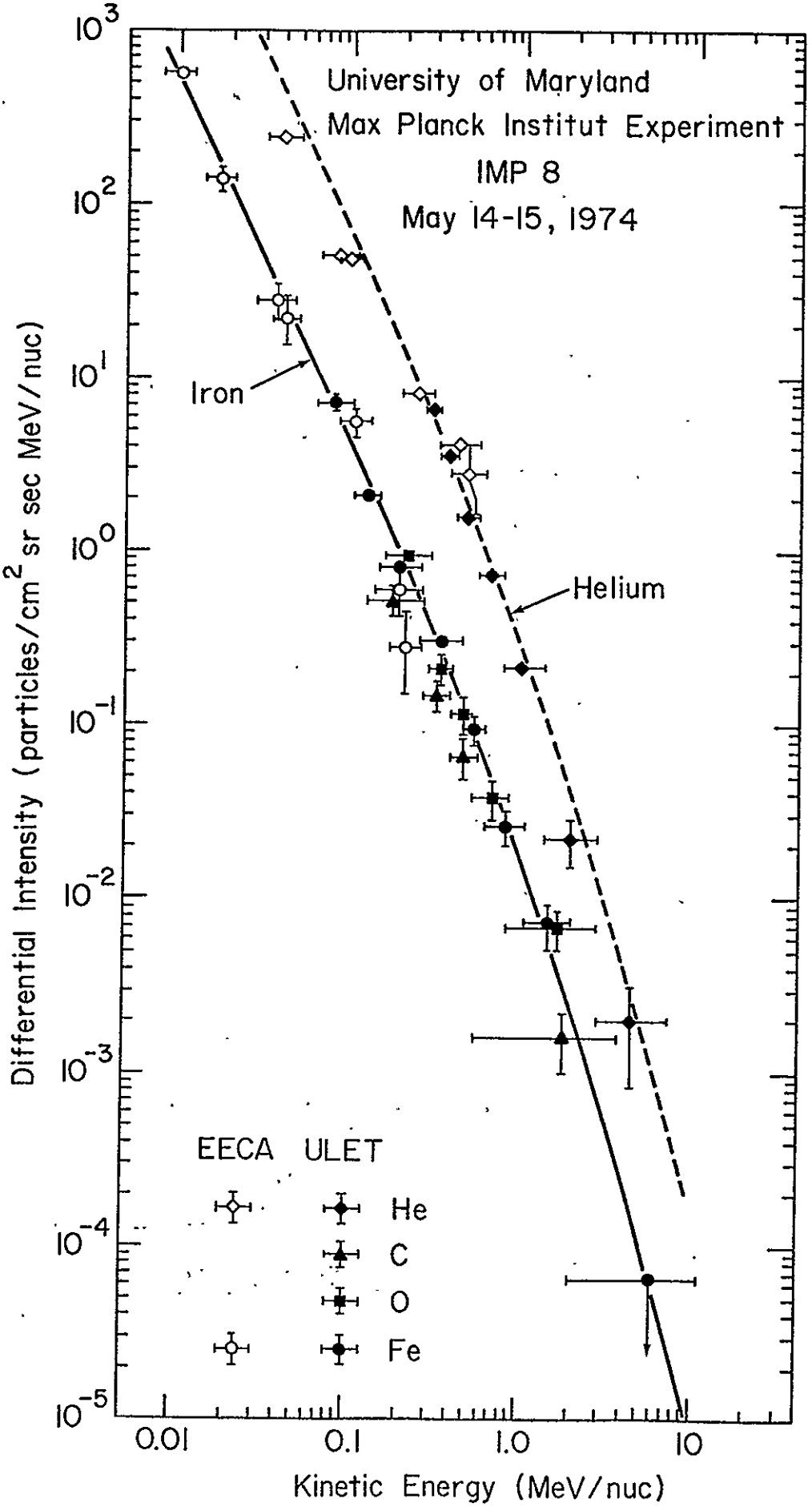
University of Maryland
Max Planck Institut Experiment
IMP 8
May 14-15, 1974
Iron
Helium
EECA ULET
He
C
O
Fe
Differential Intensity (particles/cm² sr sec MeV/nuc)
Kinetic Energy (MeV/nuc)
10³
10²
10¹
10⁰
10⁻¹
10⁻²
10⁻³
10⁻⁴
10⁻⁵
0.01
0.1
1.0
10

FIGURE 3-3

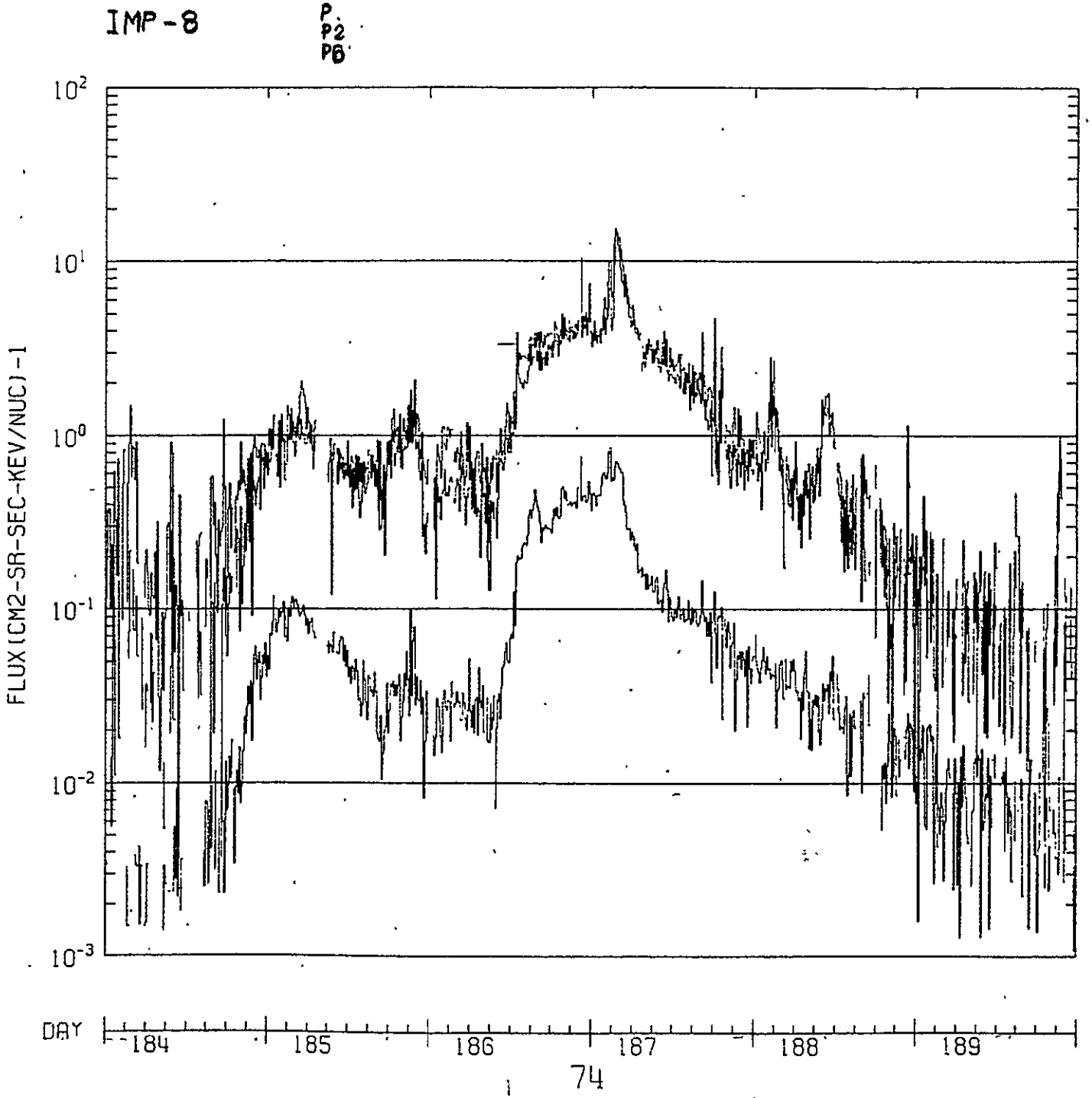
IMP-8
P1
P2
P6
FLUX(CM2-SR-SEC-KEV/NUC)-1
10^2
10^1
10^0
10^{-1}
10^{-2}
10^{-3}
DAY
184
185
186
187
188
189

FIGURE 3-4

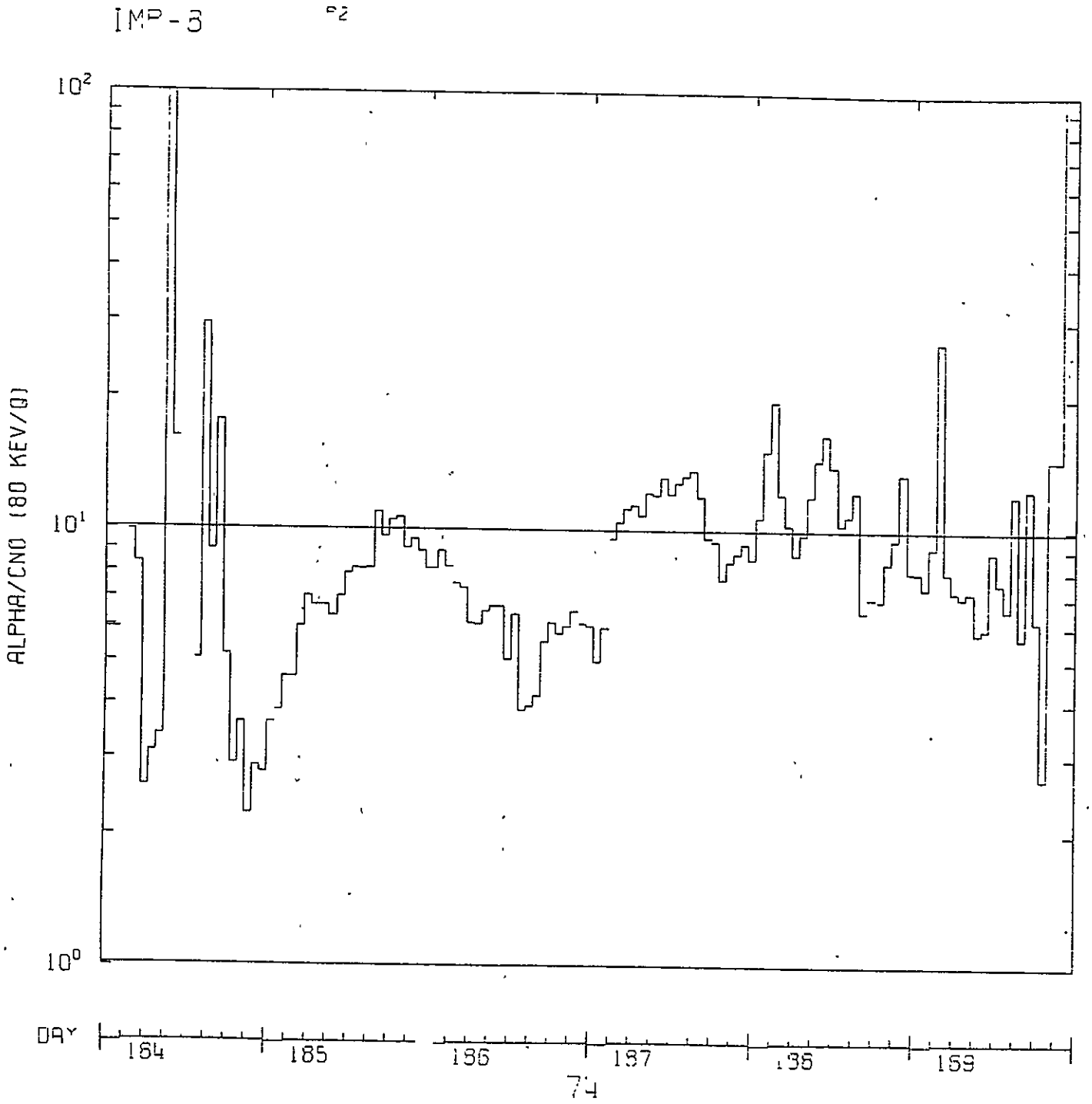

FIGURE 3-5

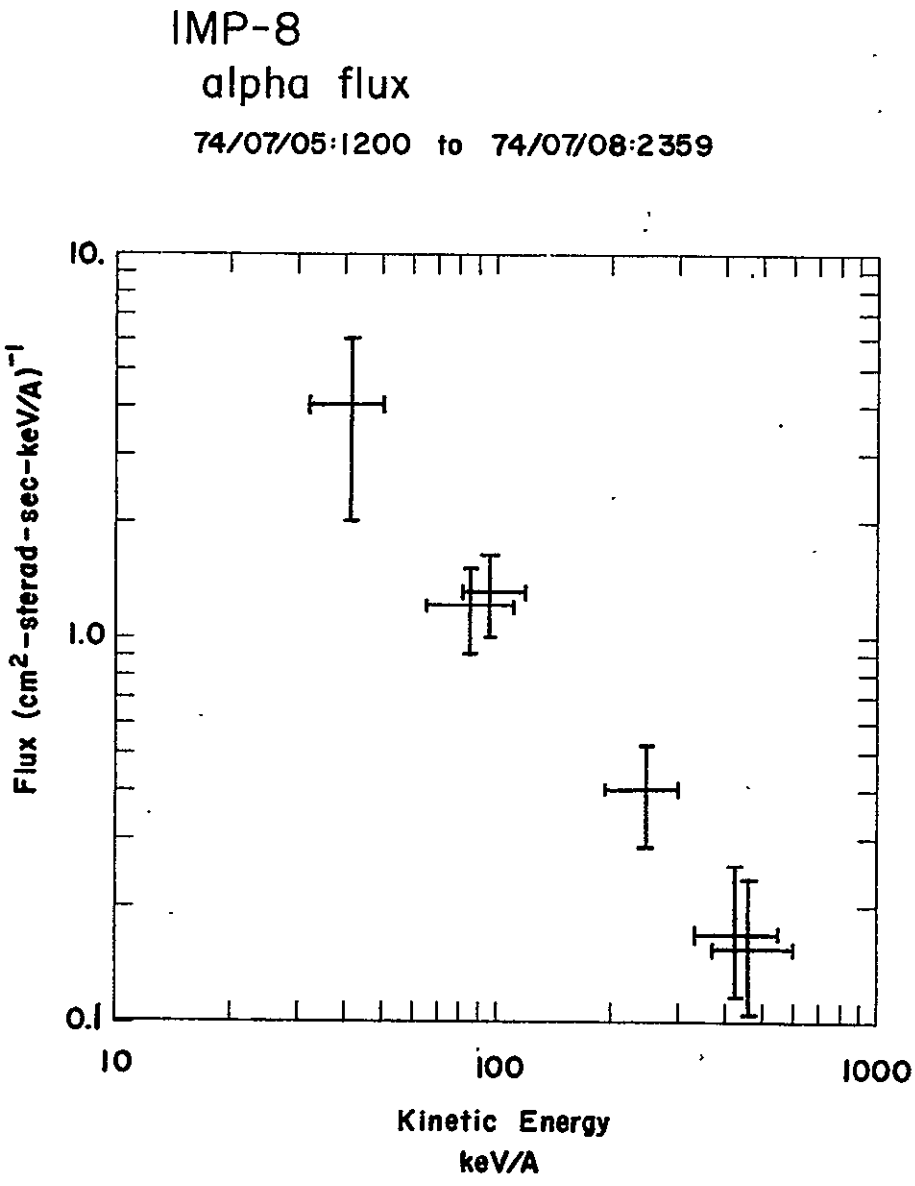
IMP-8
alpha flux
74/07/05:1200 to 74/07/08:2359
10.
1.0
0.1
Flux (cm²-sterad-sec-keV/A)⁻¹
10
100
1000
Kinetic Energy
keV/A

FIGURE 3-6

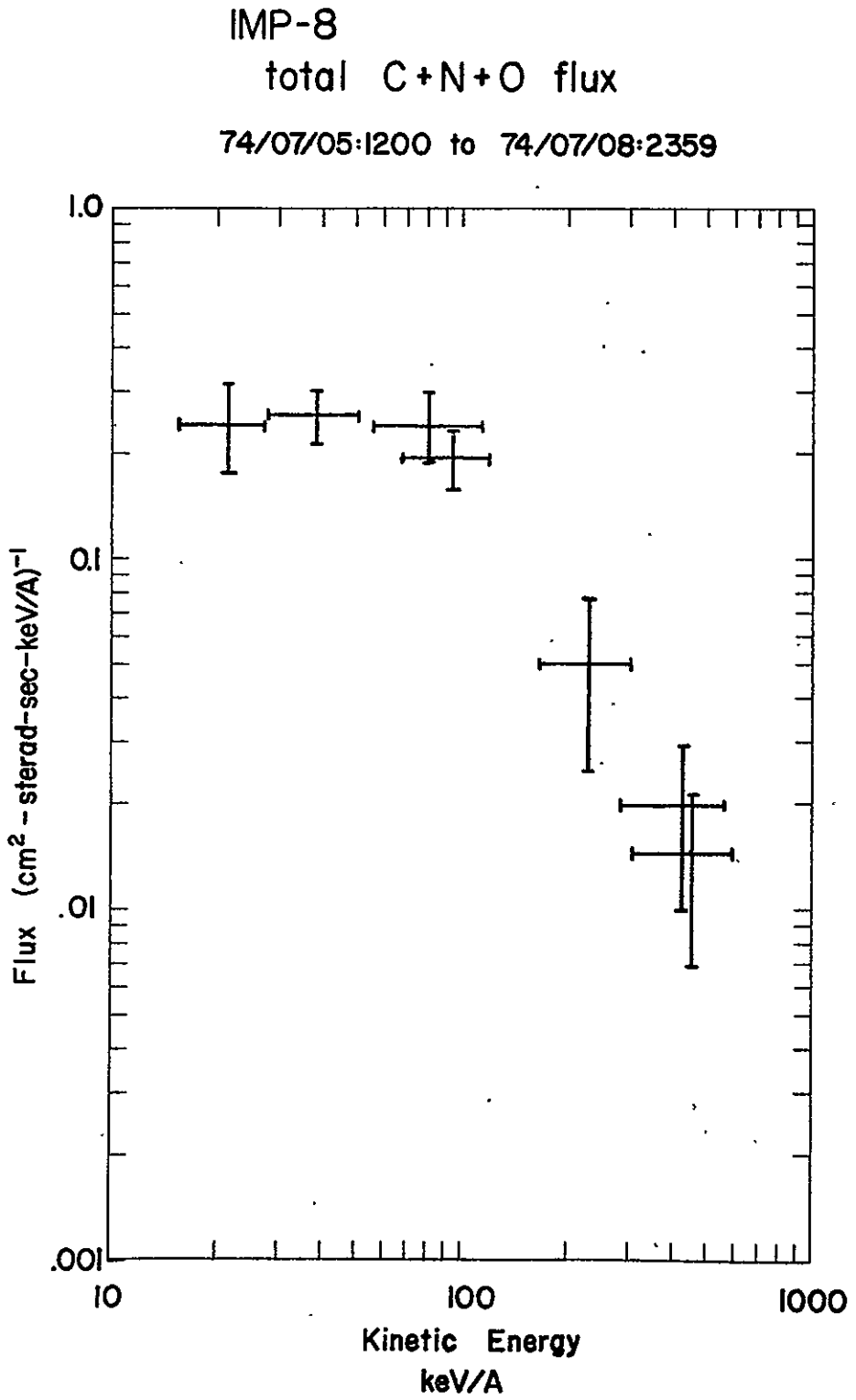
IMP-8
total C+N+O flux
74/07/05:1200 to 74/07/08:2359
1.0
0.1
.01
.001
Flux (cm² - sterad - sec - keV/A)⁻¹
10
100
1000
Kinetic Energy
keV/A

FIGURE 3-7

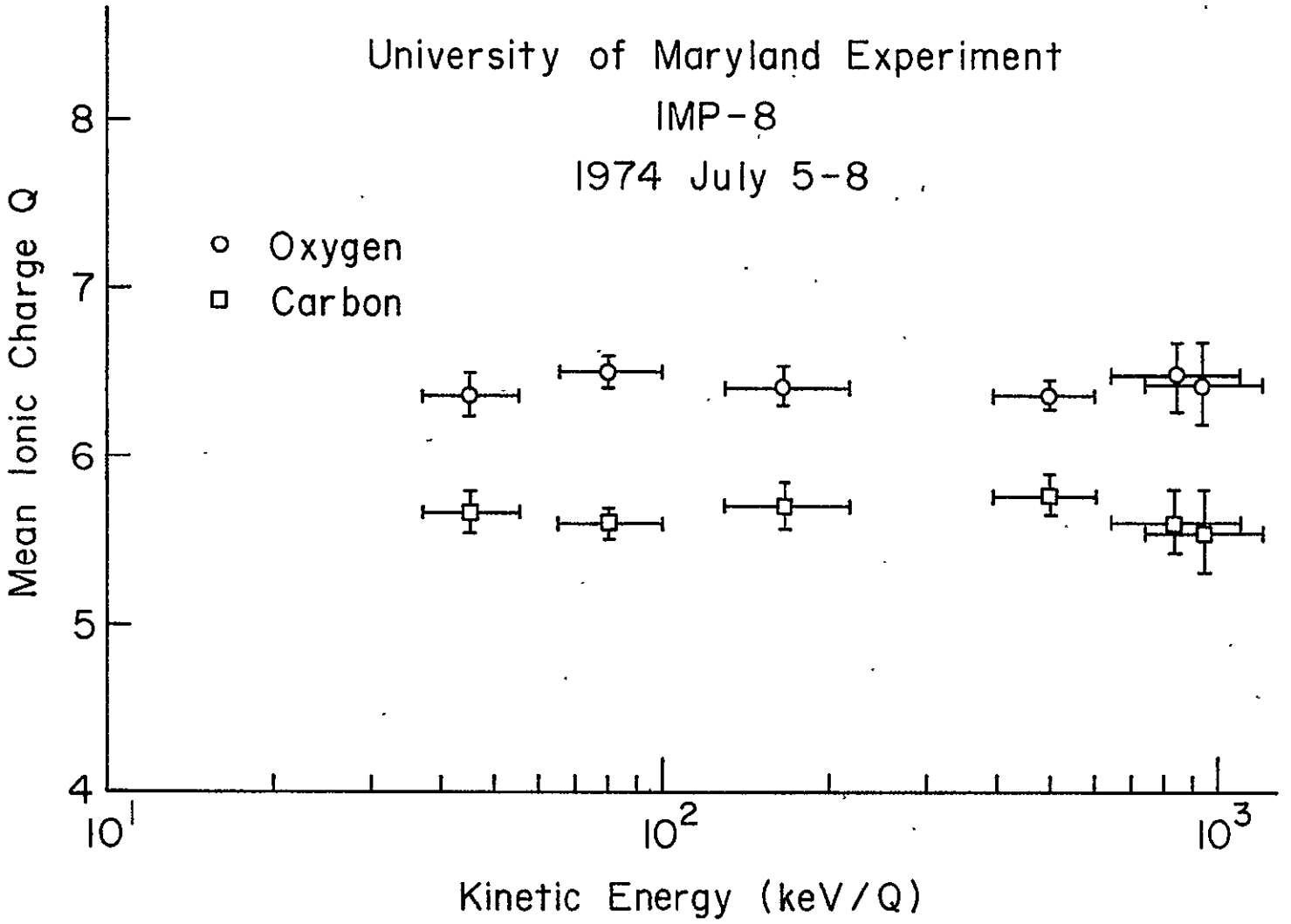
University of Maryland Experiment
IMP-8
1974 July 5-8
Oxygen
Carbon
Mean Ionic Charge Q
8
7
6
5
4
10^1
10^2
10^3
Kinetic Energy (keV/Q)

FIGURE 3-8

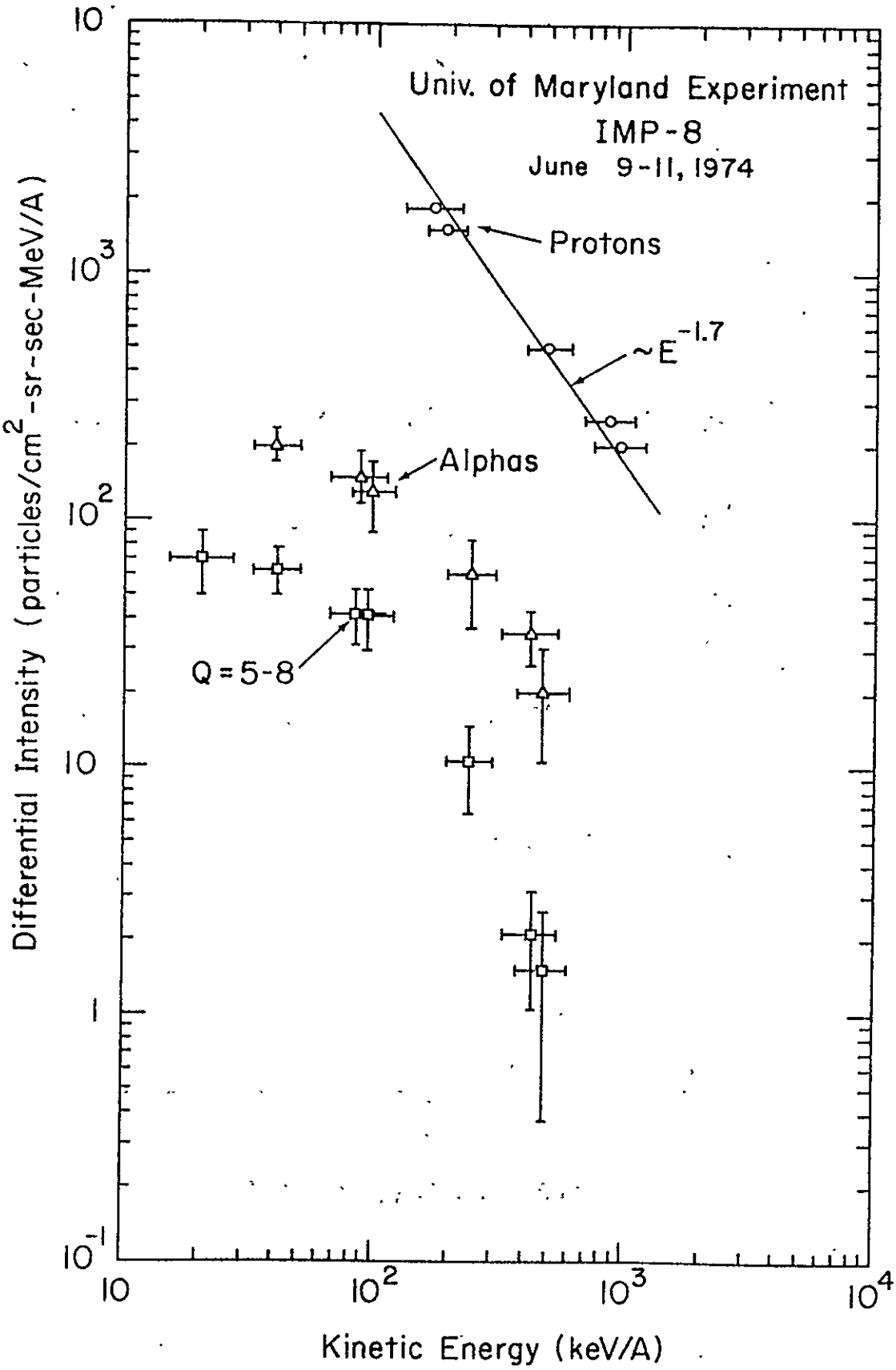
Univ. of Maryland Experiment
IMP-8
June 9-11, 1974
Protons
~E^-1.7
Alphas
Q=5-8
Differential Intensity (particles/cm^2-sr-sec-MeV/A)
Kinetic Energy (keV/A)
10
10^2
10^3
10^4
1
10^-1

FIGURE 3-9

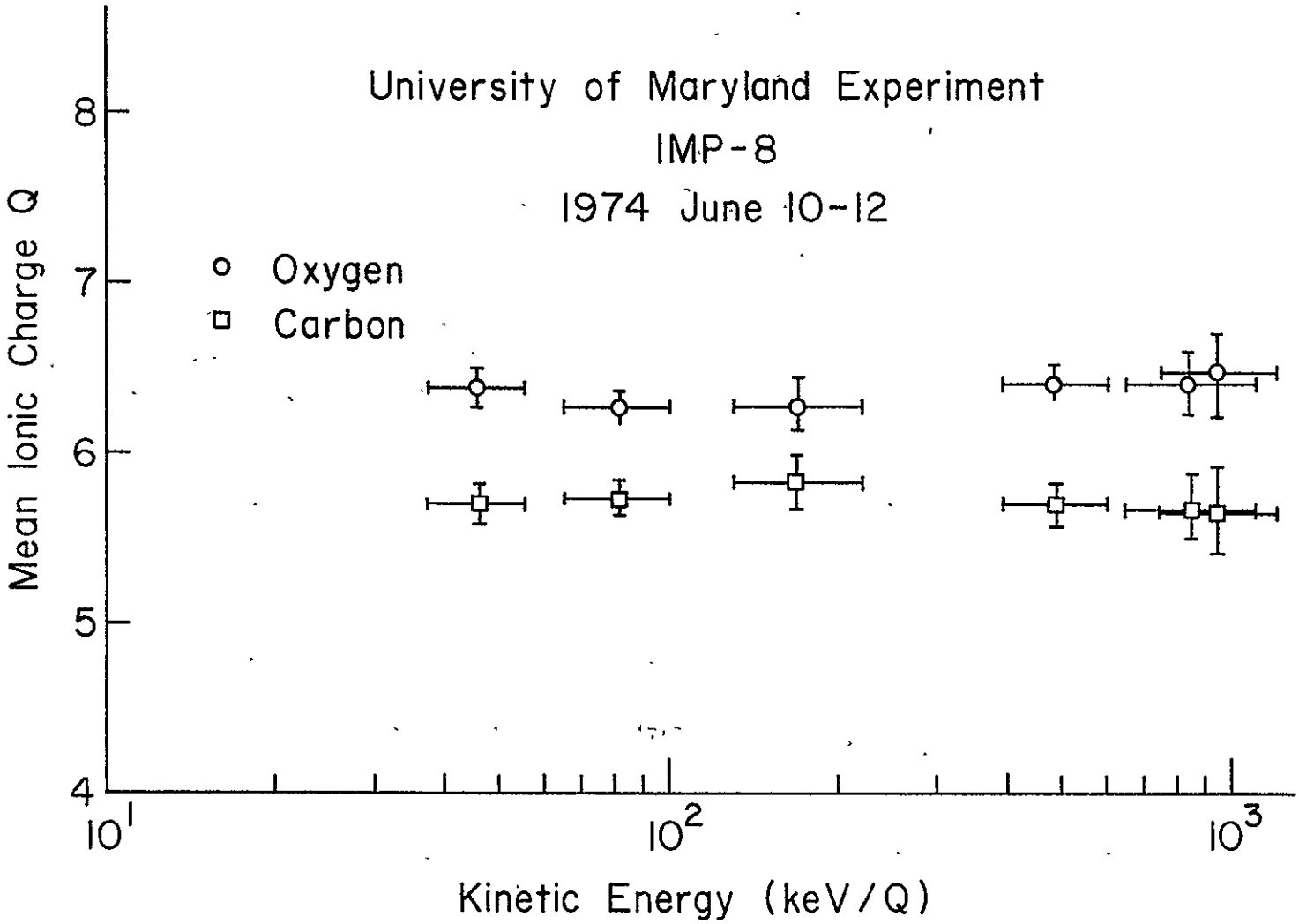
University of Maryland Experiment
IMP-8
1974 June 10-12
Oxygen
Carbon
Mean Ionic Charge Q
8
7
6
5
4
10^1
10^2
10^3
Kinetic Energy (keV/Q)

FIGURE 3-10

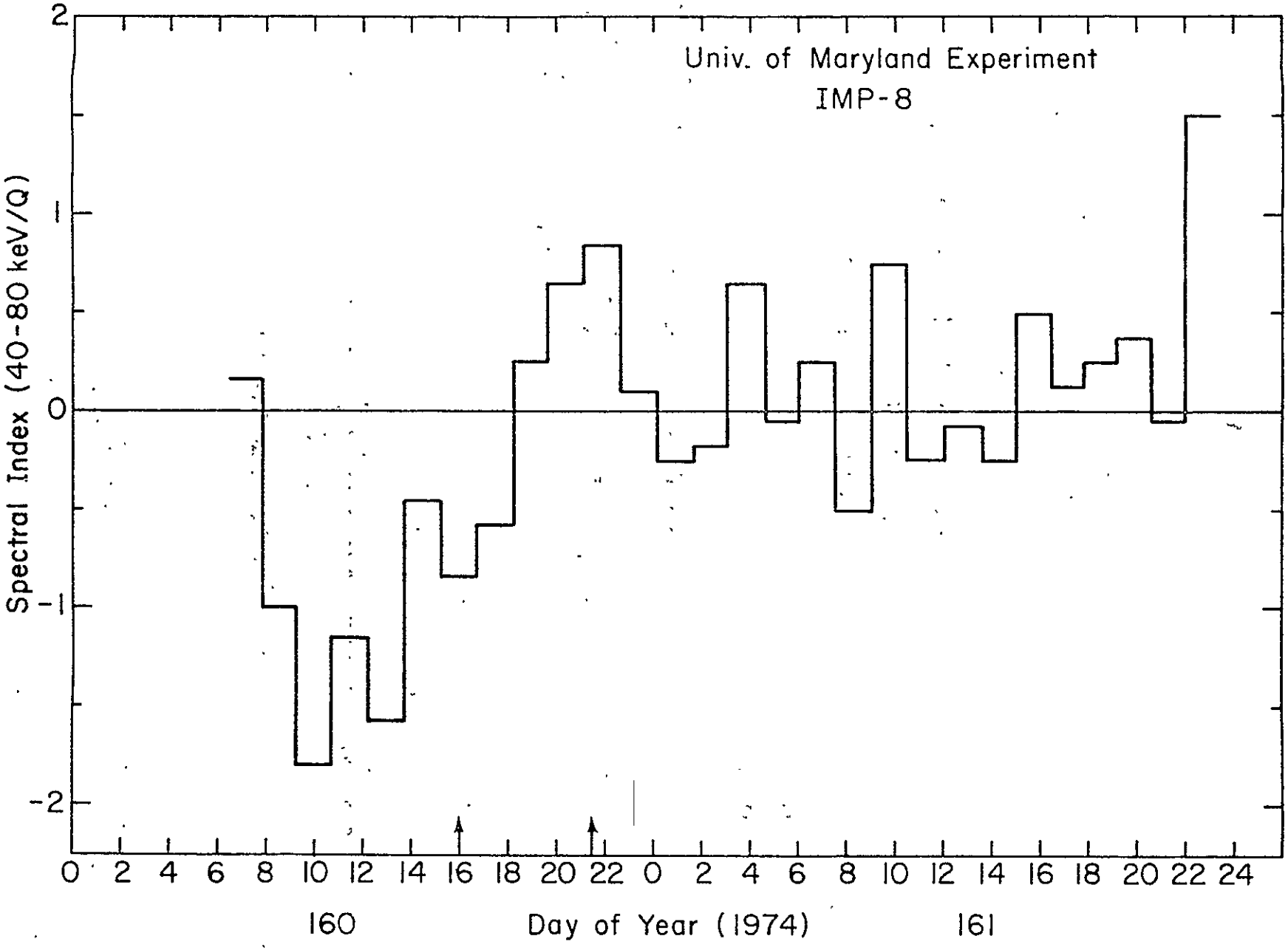
Univ. of Maryland Experiment
IMP-8
Spectral Index (40-80 keV/Q)
2
1
0
-1
-2
0 2 4 6 8 10 12 14 16 18 20 22 0 2 4 6 8 10 12 14 16 18 20 22 24
160
Day of Year (1974)
161

FIGURE 3-11

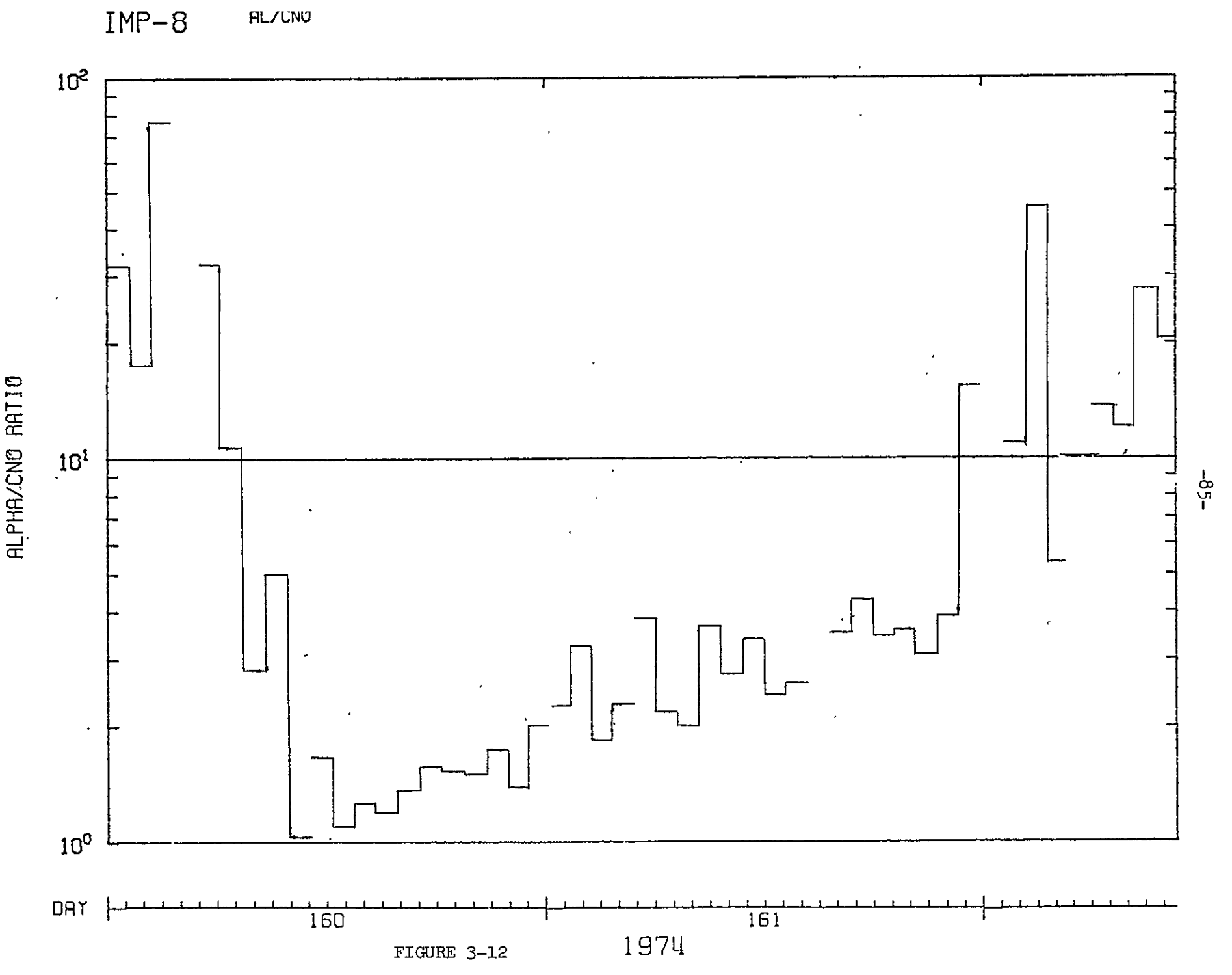

FIGURE 3-12

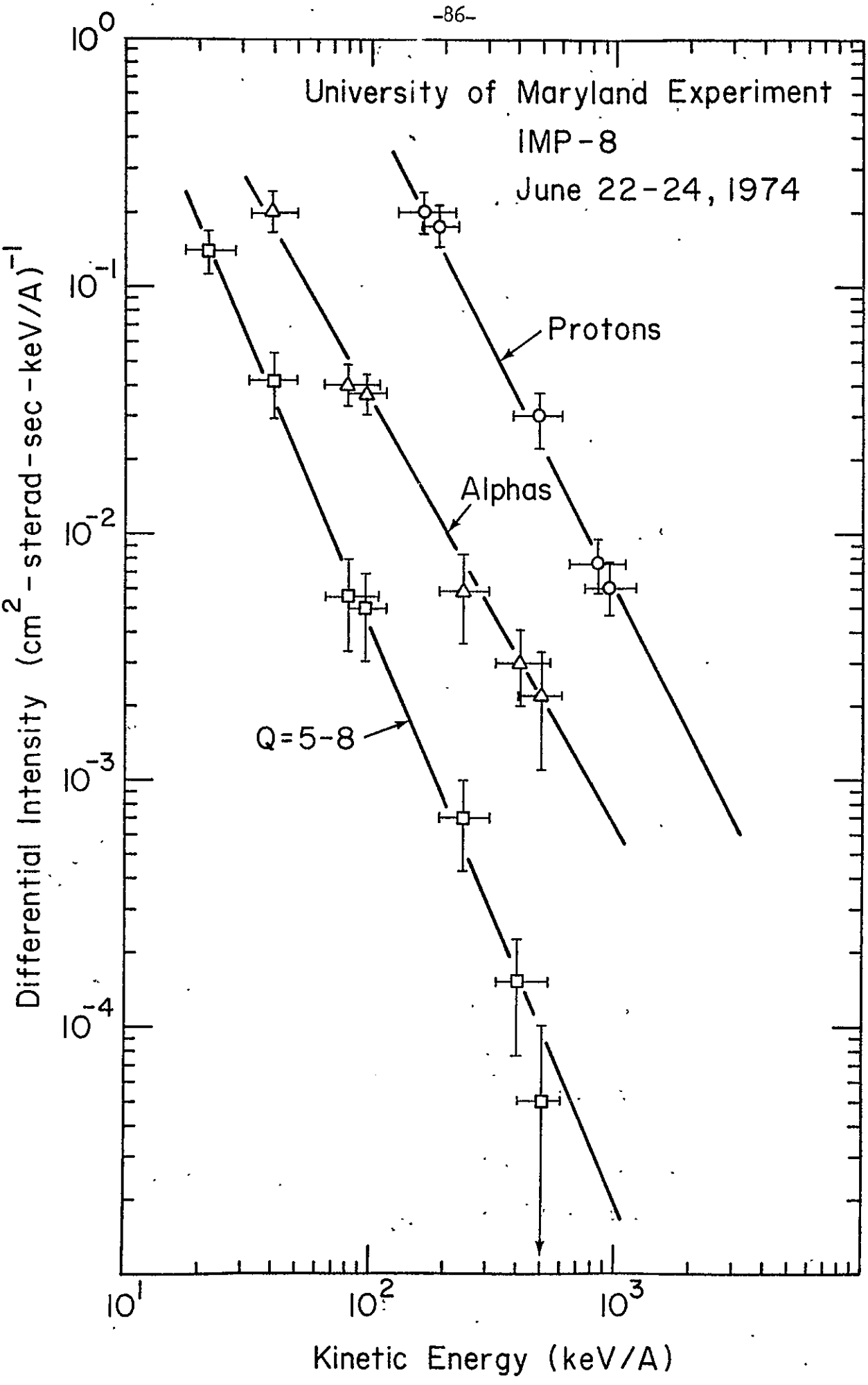
University of Maryland Experiment
IMP-8
June 22-24, 1974
Protons
Alphas
Q=5-8
Differential Intensity (cm^2-sterad-sec-keV/A)$^{-1}$
Kinetic Energy (keV/A)
10^0
10^{-1}
10^{-2}
10^{-3}
10^{-4}
10^1
10^2
10^3

FIGURE 3-13

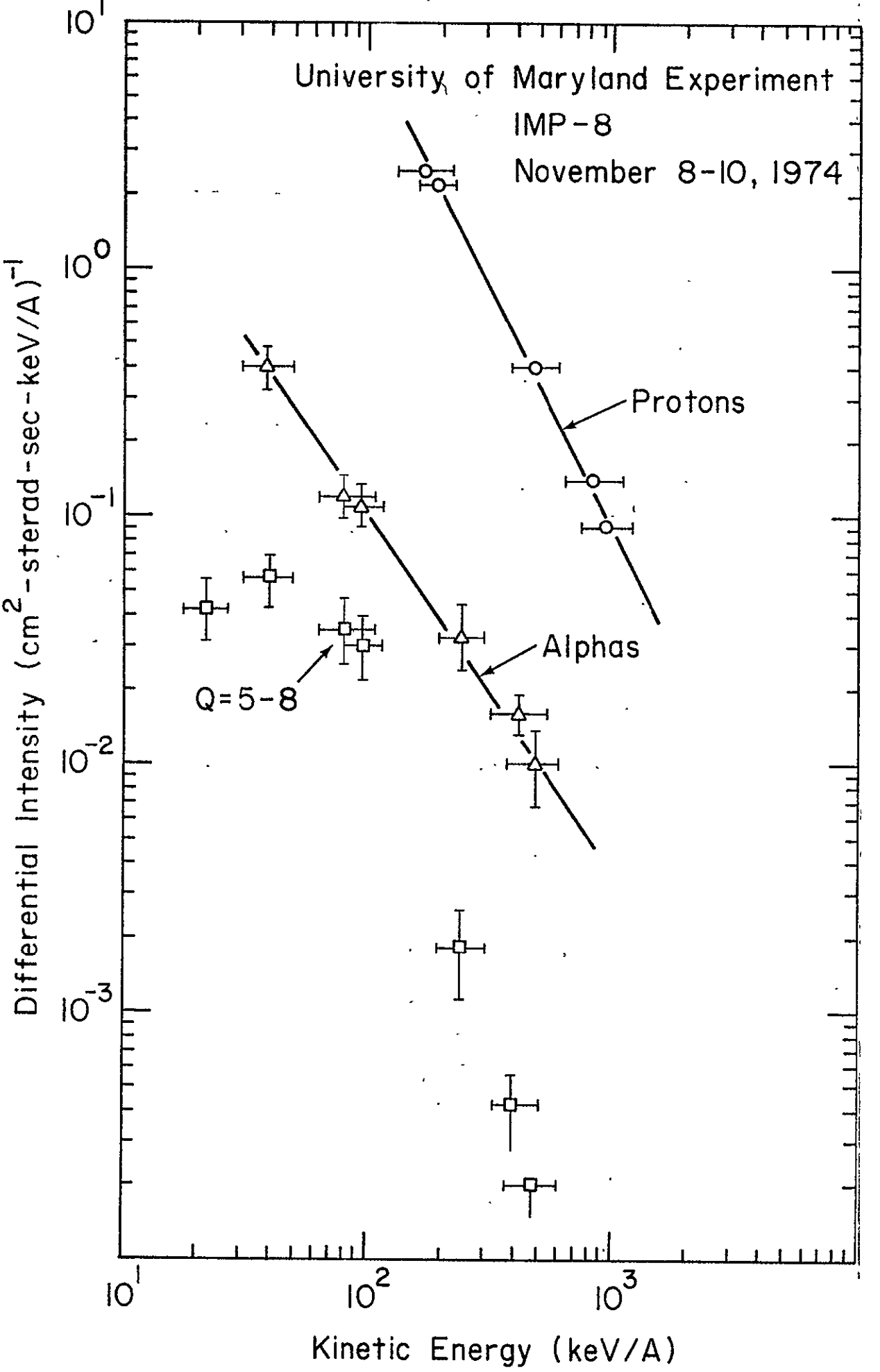
University of Maryland Experiment
IMP-8
November 8-10, 1974
Protons
Alphas
Q=5-8
Differential Intensity (cm^2-sterad-sec-keV/A)$^{-1}$
Kinetic Energy (keV/A)
10^1
10^0
10^{-1}
10^{-2}
10^{-3}
10^1
10^2
10^3

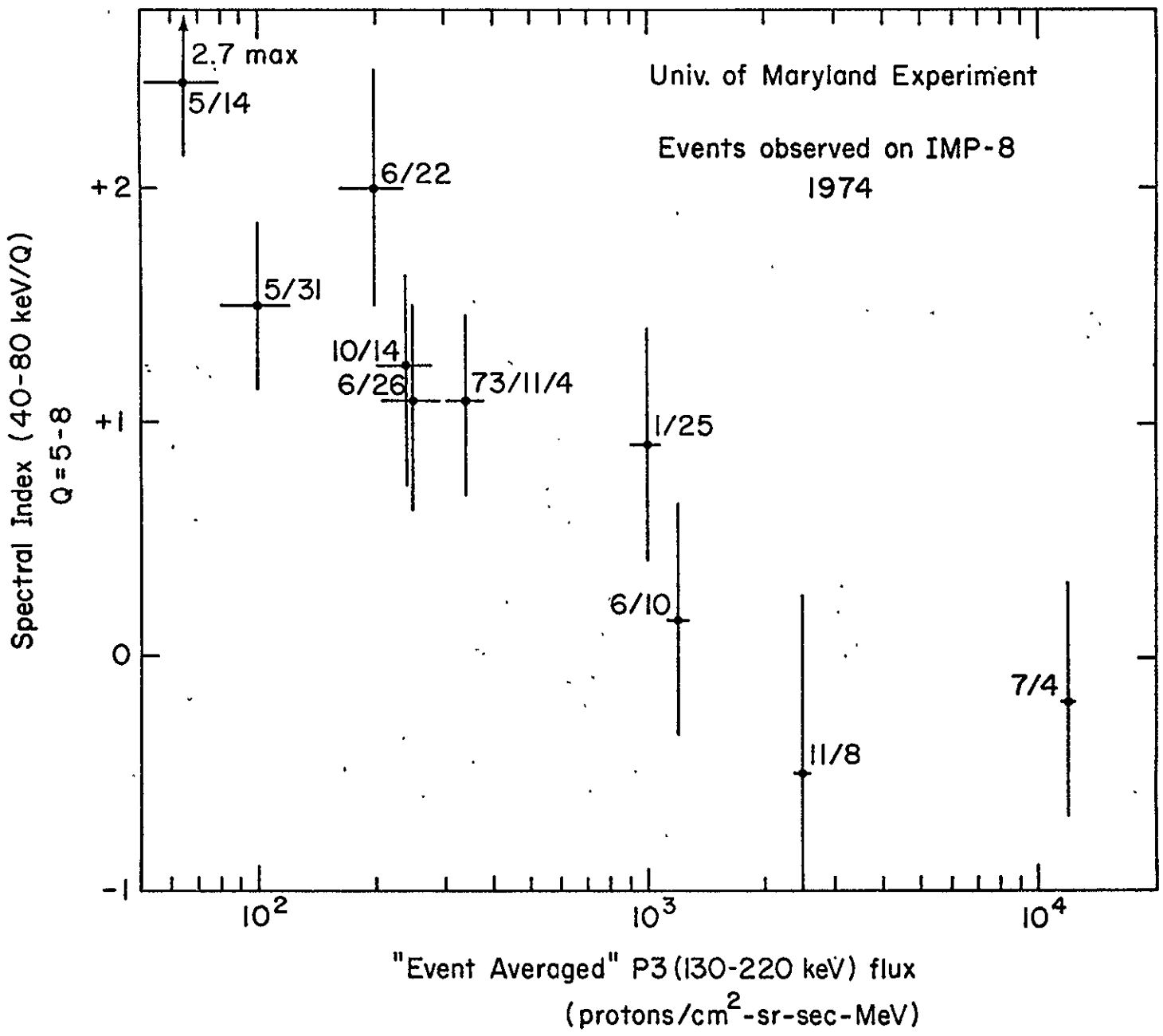
Univ. of Maryland Experiment
Events observed on IMP-8
1974
2.7 max
5/14
6/22
5/31
10/14
6/26
73/11/4
1/25
6/10
11/8
7/4
+2
+1
0
-1
10^2
10^3
10^4
Spectral Index (40-80 keV/Q)
Q=5-8
"Event Averaged" P3 (130-220 keV) flux
(protons/cm^2-sr-sec-MeV)

FIGURE 3-15

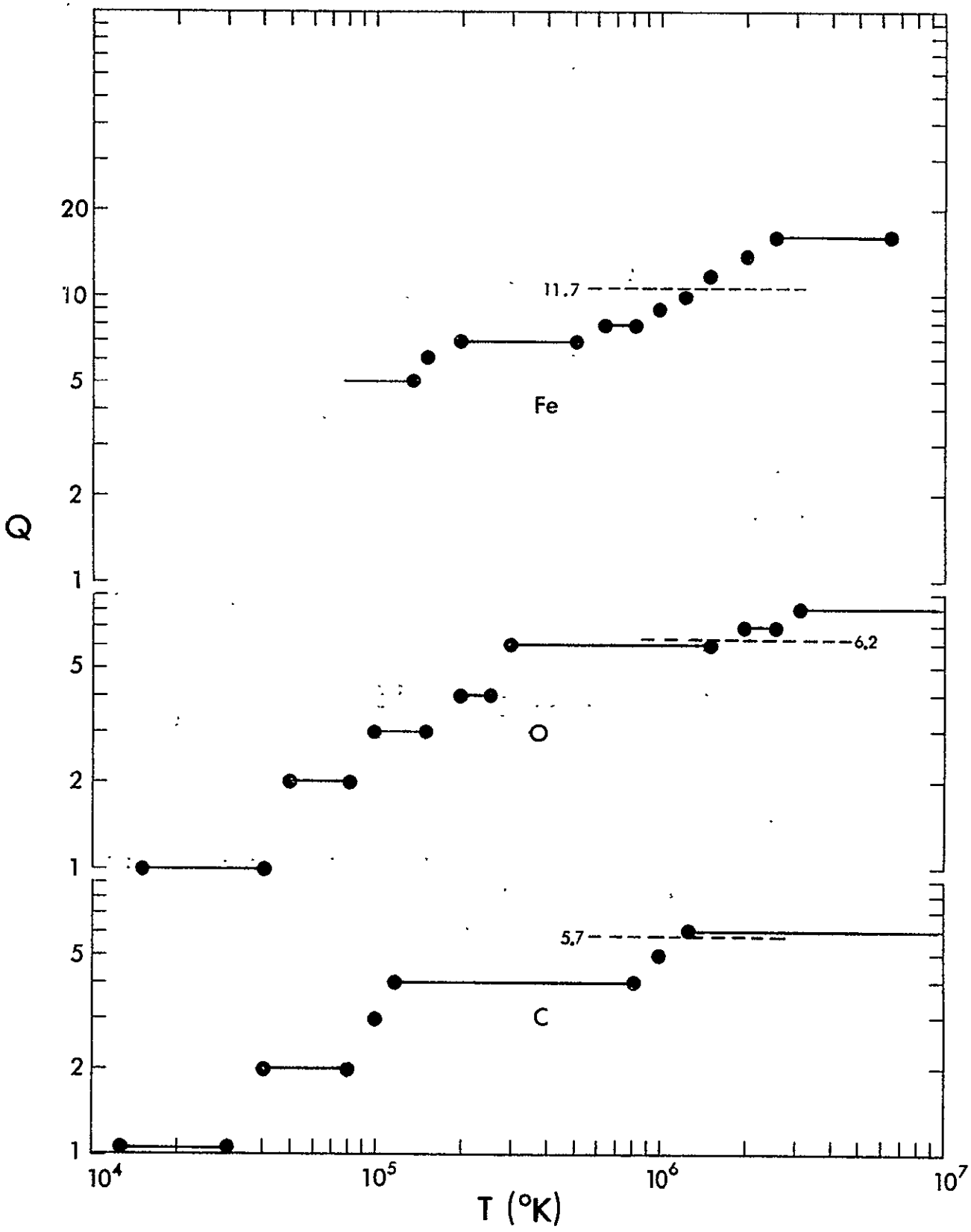

FIGURE 4-1.

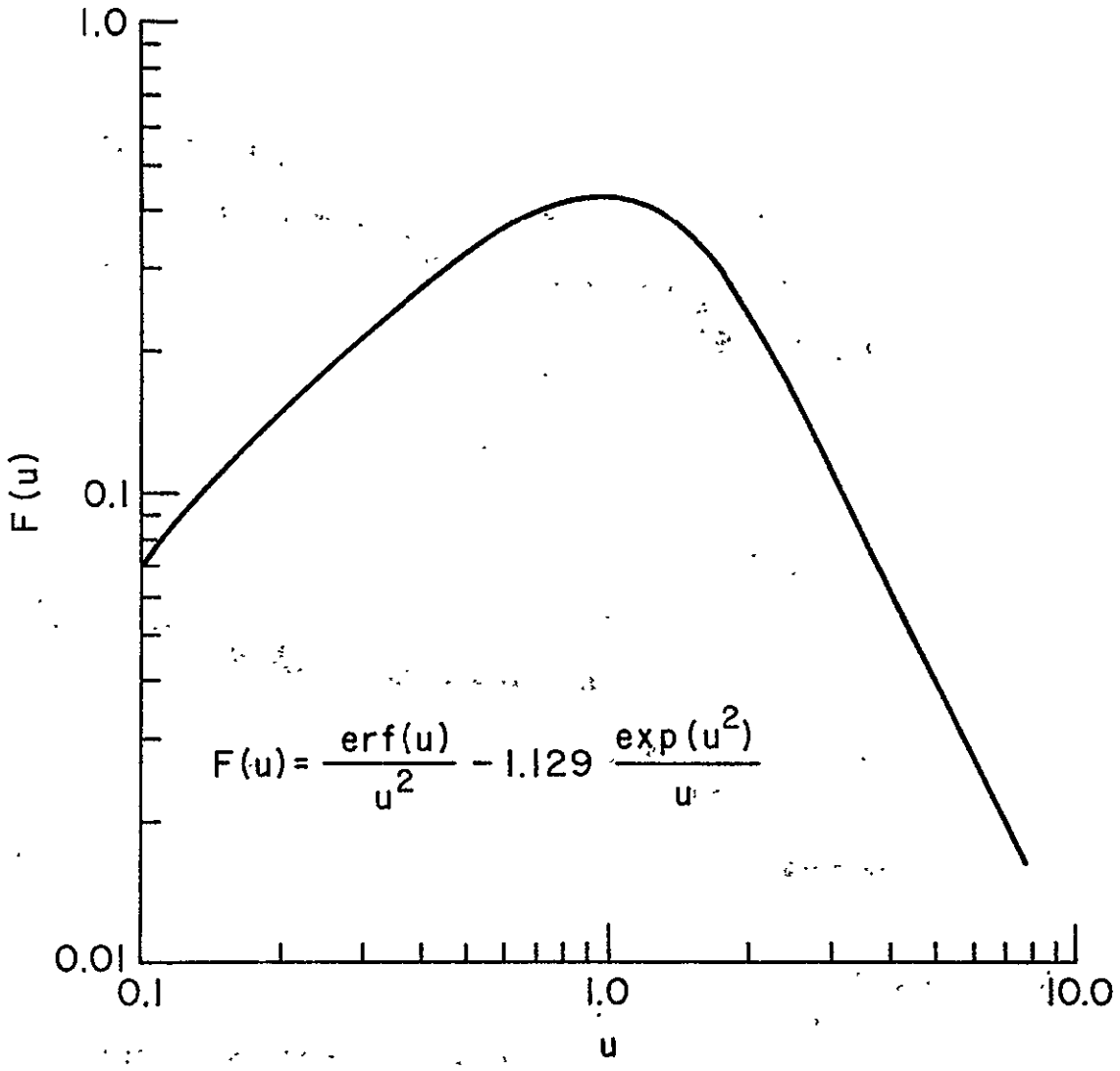

FIGURE 4-2

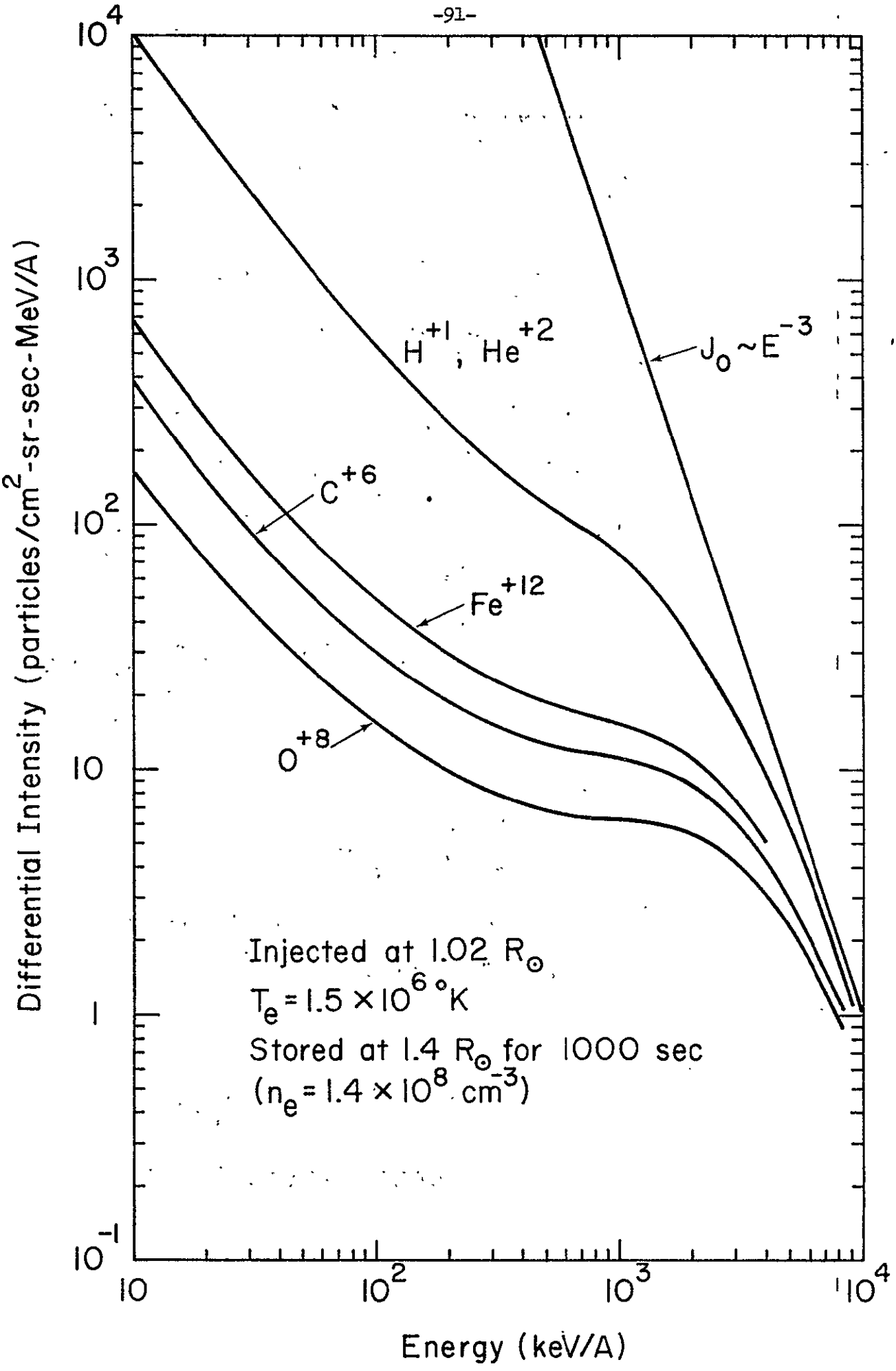
Differential Intensity (particles/cm^2-sr-sec-MeV/A)
Energy (keV/A)
10^4
10^3
10^2
10
1
10^{-1}
10
10^2
10^3
10^4
H^{+1} ; He^{+2}
$J_0 \sim E^{-3}$
C^{+6}
Fe^{+12}
O^{+8}
Injected at 1.02 $R_\odot$
$T_e = 1.5 \times 10^6$ °K
Stored at 1.4 $R_\odot$ for 1000 sec
($n_e = 1.4 \times 10^8$ cm^{-3})

FIGURE 4-3

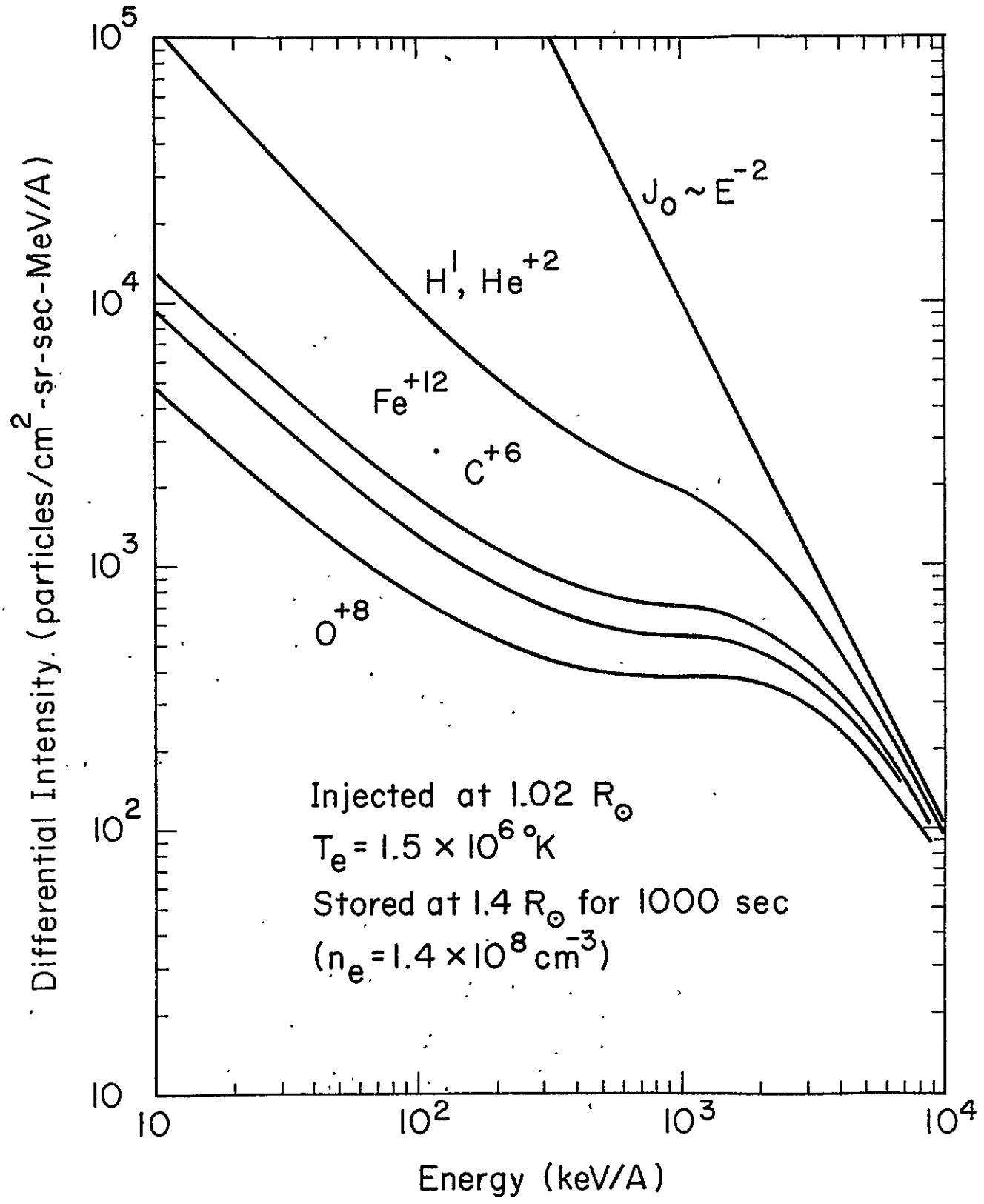
Differential Intensity (particles/cm^2-sr-sec-MeV/A)
Energy (keV/A)
10^5
10^4
10^3
10^2
10
10
10^2
10^3
10^4
$J_0 \sim E^{-2}$
H^1, He^{+2}
Fe^{+12}
C^{+6}
O^{+8}
Injected at 1.02 $R_\odot$
$T_e = 1.5 \times 10^6$ °K
Stored at 1.4 $R_\odot$ for 1000 sec
($n_e = 1.4 \times 10^8$ cm^{-3})

FIGURE 4-4

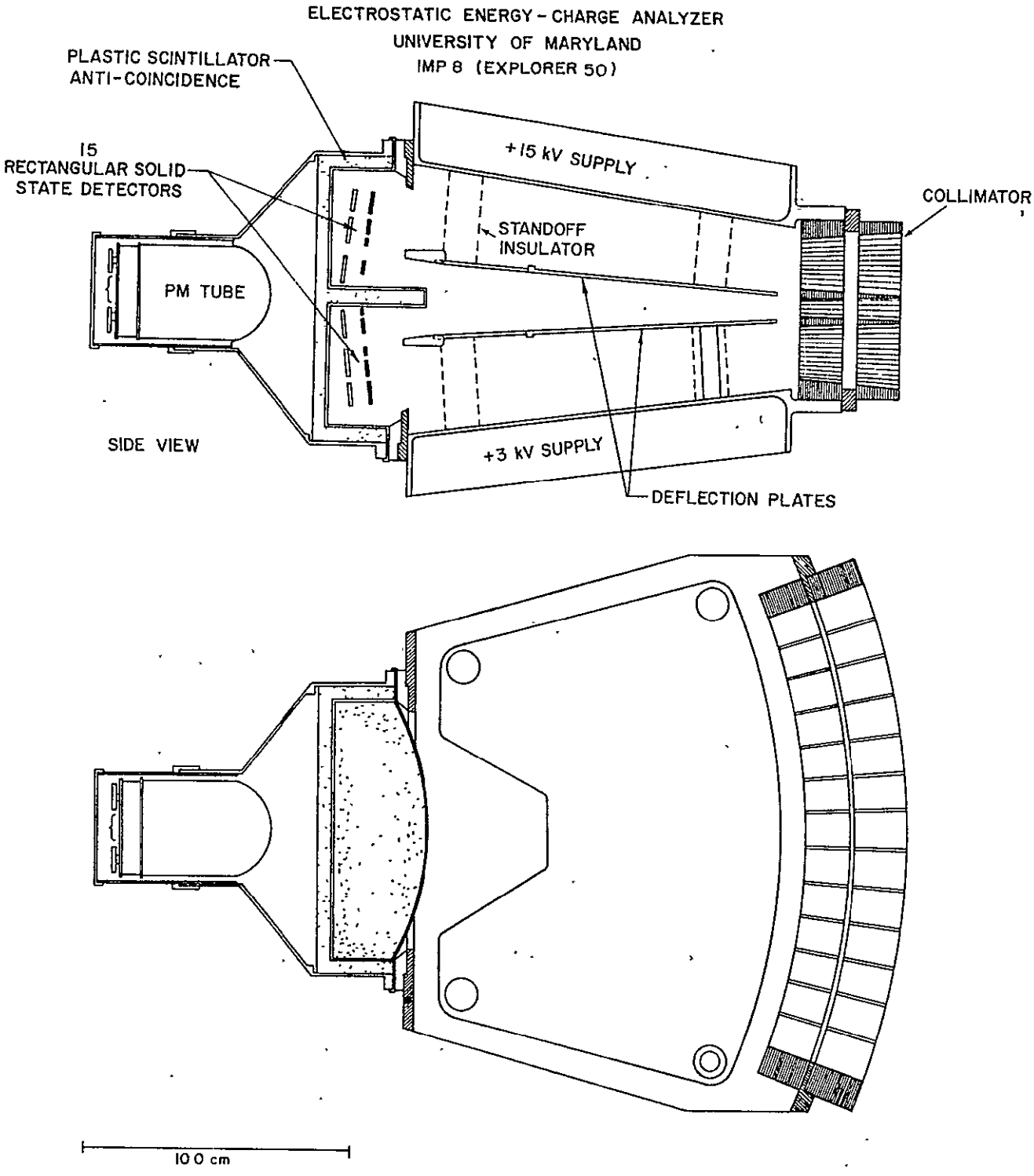

ELECTROSTATIC ENERGY/CHARGE ANALYZER
CROSS SECTION - TOP VIEW

FIGURE A-1

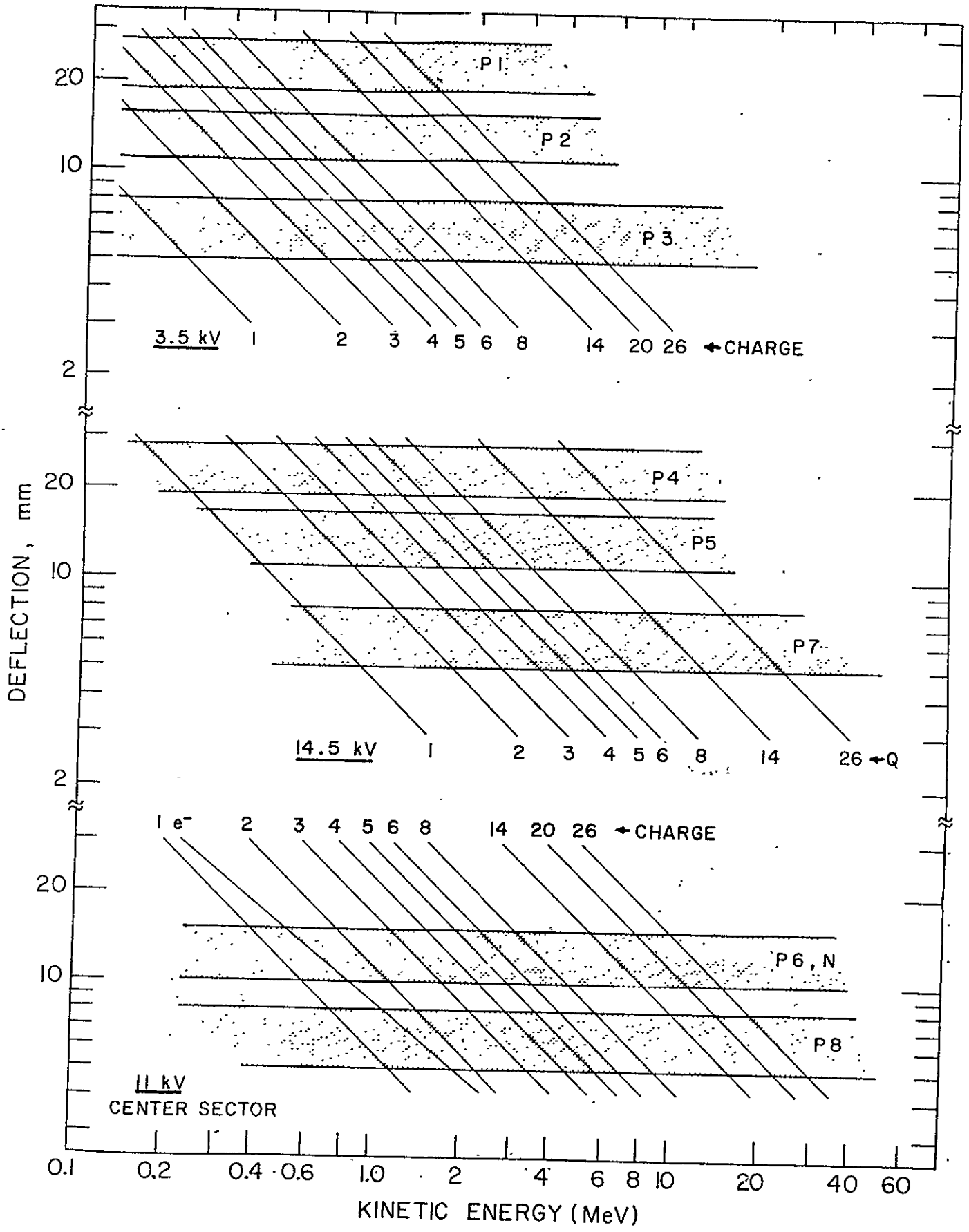
P1
P2
P3
3.5 kV
1
2
3
4
5
6
8
14
20
26
CHARGE
P4
P5
P7
14.5 kV
1
2
3
4
5
6
8
14
26
Q
1 e⁻
2
3
4
5
6
8
14
20
26
CHARGE
P6, N
P8
11 kV
CENTER SECTOR
DEFLECTION, mm
20
10
2
20
10
2
20
10
0.1
0.2
0.4
0.6
1.0
2
4
6
8
10
20
40
60
KINETIC ENERGY (MeV)

FIGURE A-2

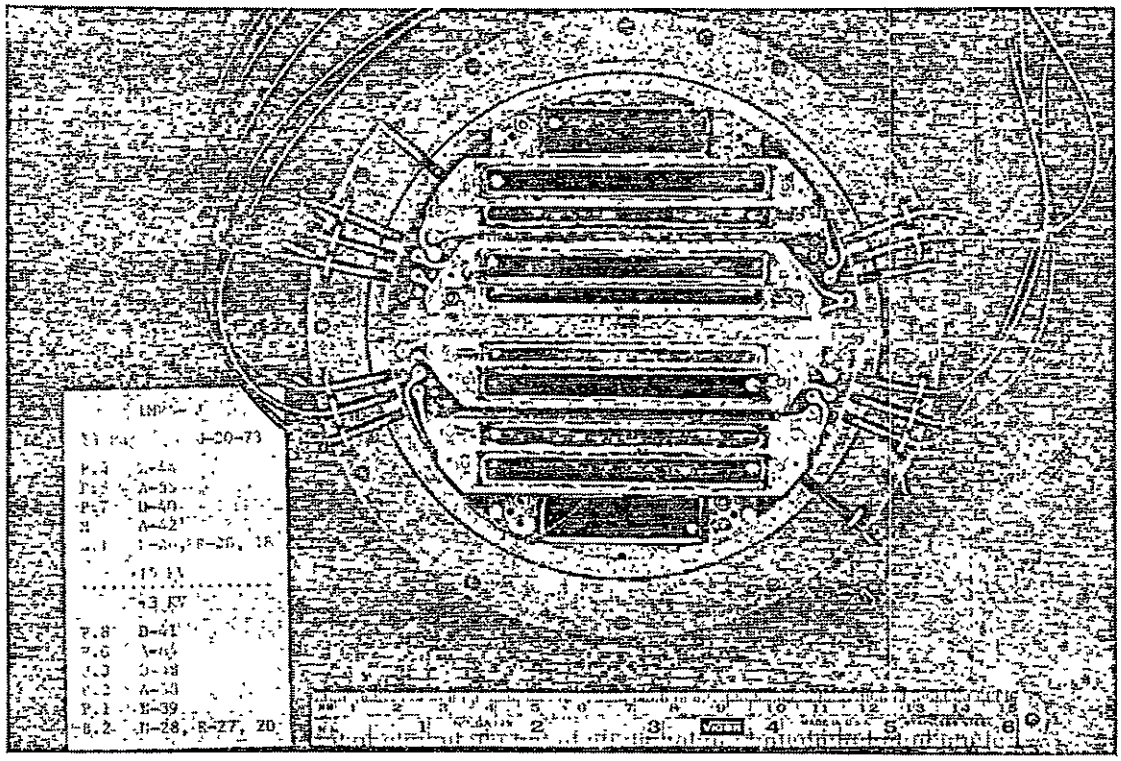

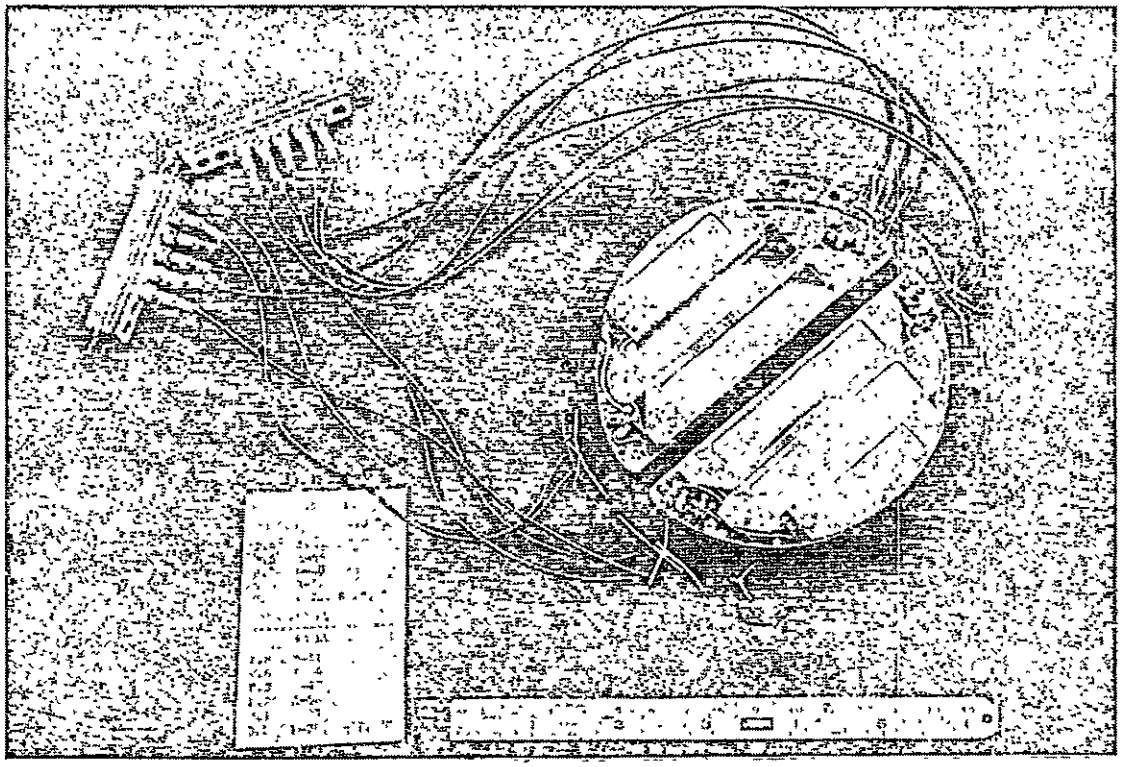

FIGURE A-3

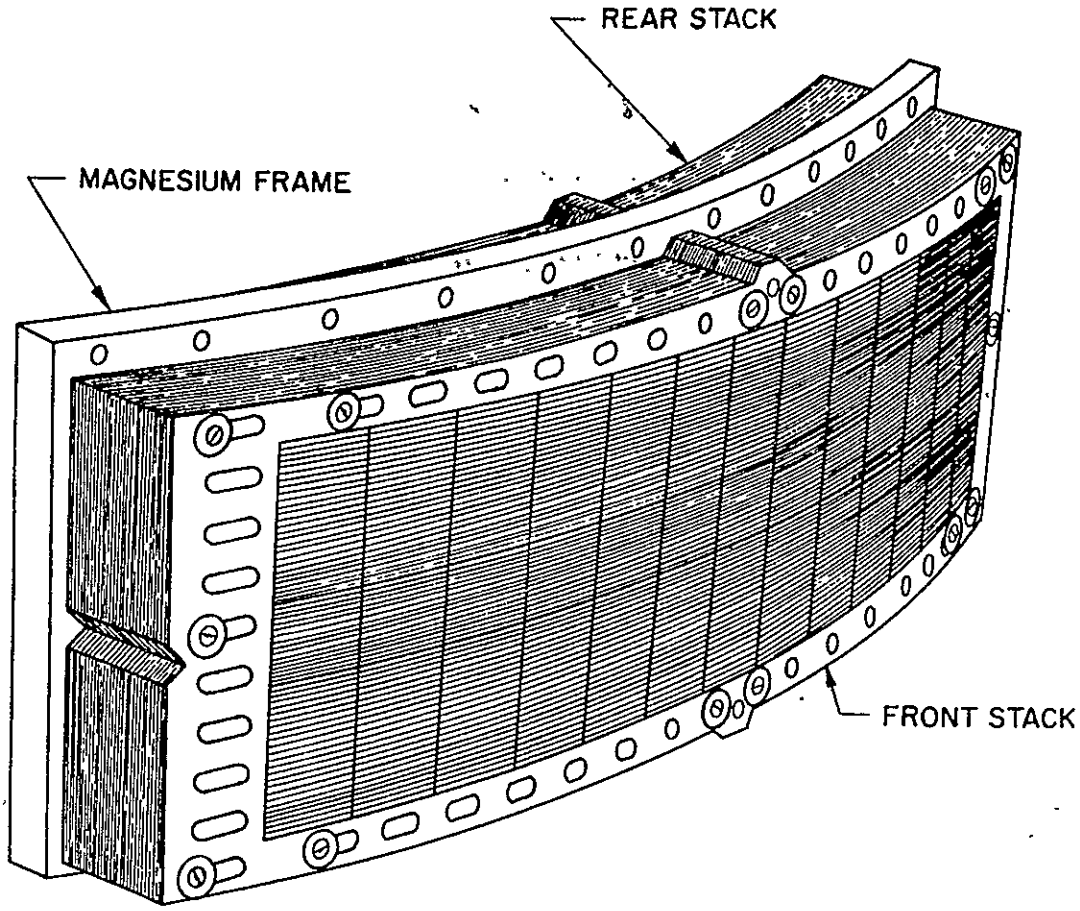

THE ASSEMBLED COLLIMATOR STACK

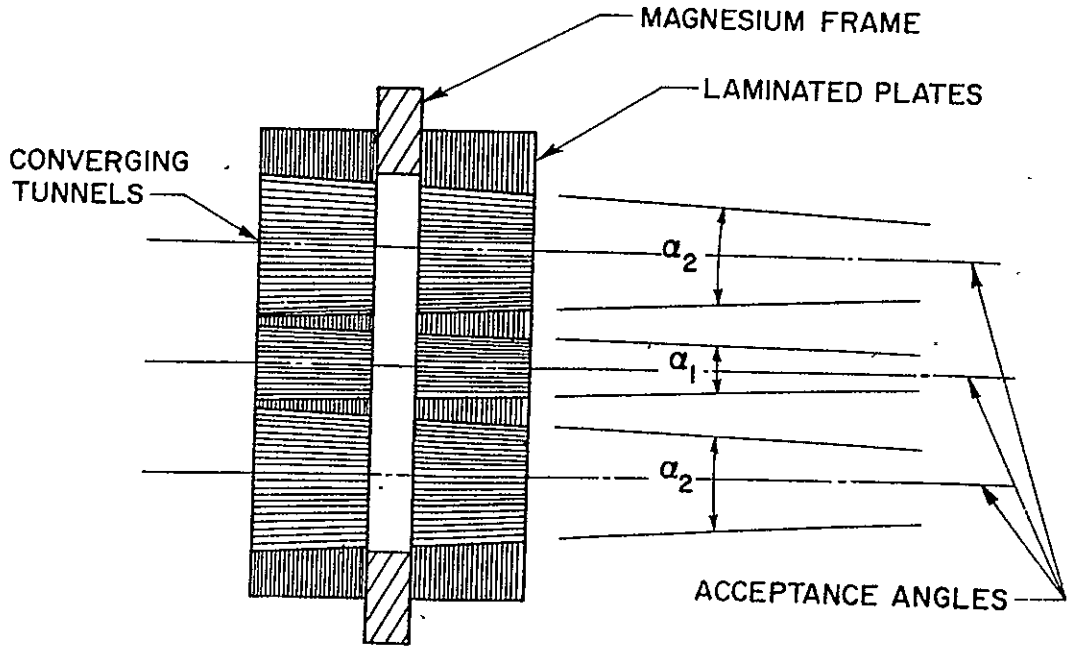

CROSS SECTION THRU THE COLLIMATOR

FIGURE A-4

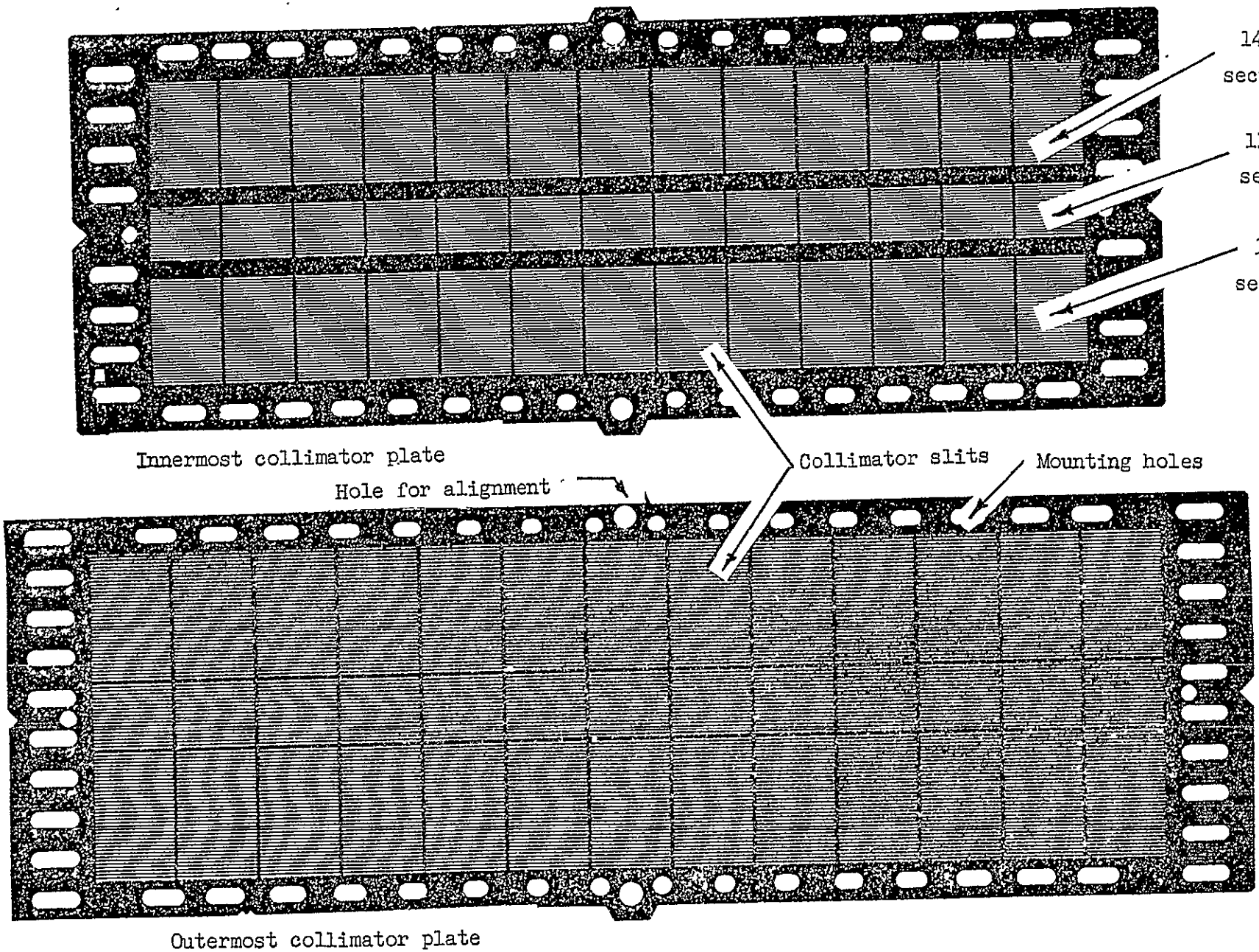
14.5 kv
section
11 kv
section
3.5 kv
section
Innermost collimator plate
Collimator slits
Mounting holes
Hole for alignment
Outermost collimator plate

FIGURE A-5

BLOCK DIAGRAM OF ELECTROSTATIC ENERGY - CHARGE ANALYZER
UNIVERSITY OF MARYLAND

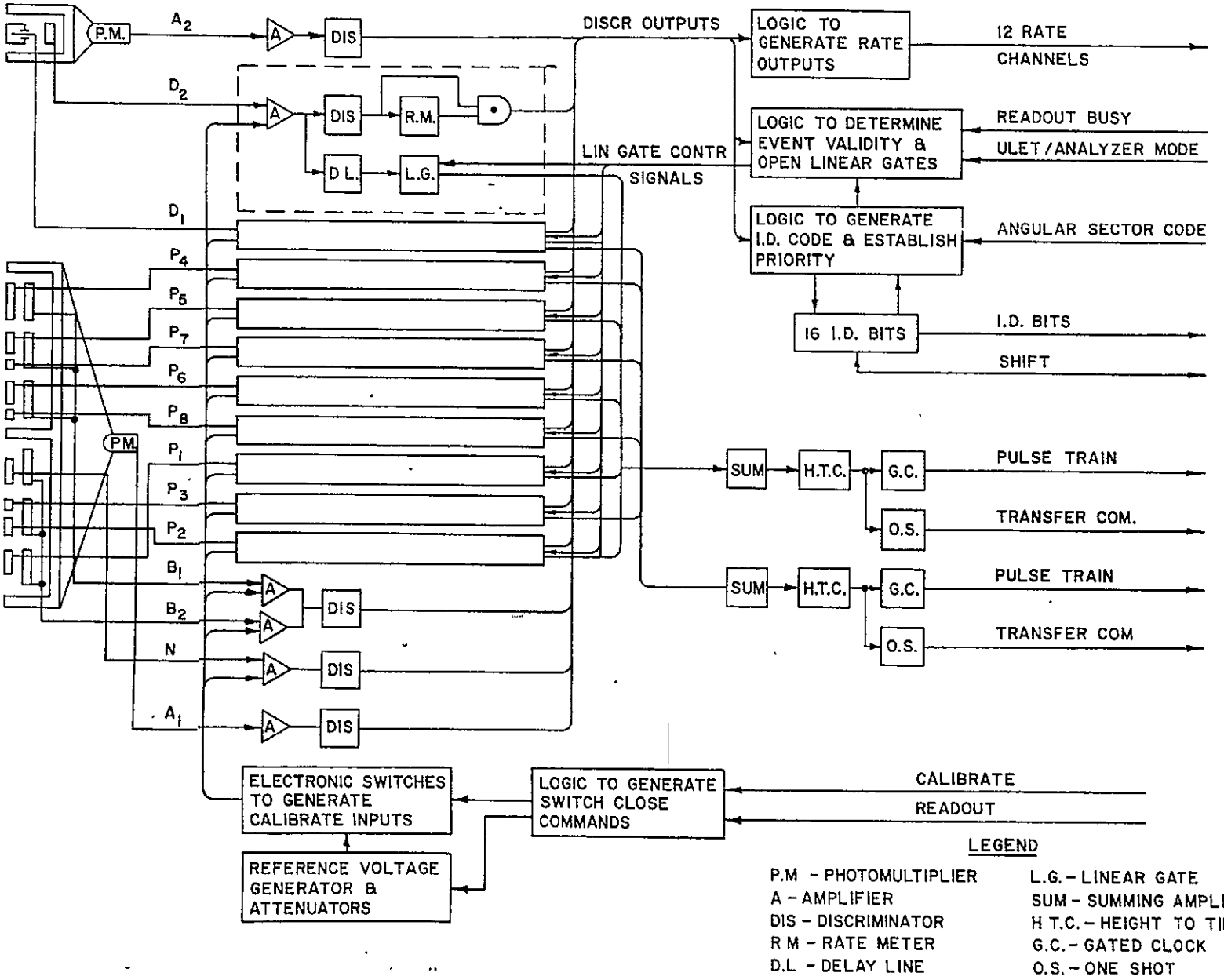

LEGEND

P.M - PHOTOMULTIPLIER	L.G. - LINEAR GATE
A - AMPLIFIER	SUM - SUMMING AMPLIFIER
DIS - DISCRIMINATOR	H T.C. - HEIGHT TO TIME CONV.
R M - RATE METER	G.C. - GATED CLOCK
D.L - DELAY LINE	O.S. - ONE SHOT

TABLE 3

Effect of Antifoams on Foam Height[1]
With Ivory and Palmeto Based Wash Waters

Antifoam	Foam Height at Various Dosages (cm)							
	200 ppm		300 ppm		400 ppm		500 ppm	
	15 sec	60 sec	15 sec	60 sec	15 sec	60 sec	15 sec	60 sec
Palmeto Soap Based Wash Water								
AF-60 [2]	0.1	0.1	0.1	0.1	-	-	-	-
	0.2	0.1	0.0	0.0	-	-	-	-
AF-72 [2]	0.1	0.1	0.0	0.0	-	-	-	-
	0.1	0.1	0.0	0.0	-	-	-	-
AF-93 [2]	0.1	0.1	0.1	0.1	-	-	-	-
	0.1	0.1	0.3	0.1	-	-	-	-
Ivory Soap Based Wash Water								
SWS-211 [3]	0.6	0.3	0.5	0.2	-	-	0.5	0.1
	0.6	0.3	0.5	0.2	-	-	0.5	0.2
AF-72	-	-	0.4	0.2	0.4	0.2	0.5	0.2
	-	-	0.4	0.2	0.5	0.2	0.3	-
AF-93	-	-	0.5	0.2	-	-	-	-
	-	-	0.5	0.2	-	-	-	-
AF-60	-	-	0.5	0.3	-	-	-	-
	-	-	0.4	0.3	-	-	-	-

(1) By NASA "shake test"

(2) General Electric

(3) SWS Silicones

TABLE 4

Effect of Antifoams on Dynamic Foam Height
Using Miranol JEM Based Wash Water

Antifoam	Foam Height (cm) Vs. Time Resulting From Various Dosages of Antifoam					
	50 ppm			200 ppm		
	1 min.	2 min.	5 min.	1 min.	2 min.	5 min.
AF-75 (1)	1/2 1/2	1/2 1/2	1/2 1	- -	- -	- -
DB-110 (2)	1/2 1/2	1/2 1/2	1/2 1/2	- -	- -	- -
Colloid 680 (3)	- -	- -	- -	0 1/2	1/2 1/2	1/2 1
Control, no antifoam	4	7	13	-	-	-

(1) General Electric Company

(2) Dow Corning Corporation

(3) Colloids, Inc.

TABLE 5

Effect of Antifoams on Dynamic Foam Height
Using Palmeto Based Wash Water

Antifoam	Foam Height (cm) Vs. Time Resulting From Various Dosages of Antifoam					
	200 ppm			300 ppm		
	1 min.	2 min.	5 min.	1 min.	2 min.	5 min.
AF-75	1-1/2 1-1/2	2 2	3 4	1/2 0	1 1/2	1-1/2 1
SWS-211 (1)	1-1/2 1	2 1	2 1-1/2	1/2 1/2	1/2 1	1/2 1
DB-110	2 1	2 1-1/2	4 4	1 1/2	1-1/2 1	3 1-1/2
Control, no antifoam	48 cm (5 minutes)					

(1) SWS Silicones, Division of Stauffer Chemical

TABLE 6

Effect of Antifoams on Dynamic Foam Height
Using ML-11 Based Wash Water

Antifoam	Foam Height (cm) Vs. Time Resulting From Various Dosages of Antifoam											
	100 ppm			150 ppm			200 ppm			300 ppm		
	1 min.	2 min.	5 min.	1 min.	2 min.	5 min.	1 min.	2 min.	5 min.	1 min.	2 min.	5 min.
AF-93 (1)	1	1-1/2	4	-	-	-	0	1/2	1	0	0	1
	1	1-1/2	3	-	-	-	0	1/2	1-1/2	-	-	-
SWS-211	-	-	-	-	-	-	1	1-1/2	2	0	0	1
	-	-	-	-	-	-	1-1/2	2	2-1/2	-	-	-
AF-75	1	2	5-1/2	-	-	-	0	1	1-1/2	0	0	1
	-	-	-	-	-	-	0	1	2	-	-	-
Ferric Chloride	-	-	-	1	1-1/2	1-1/2	-	-	-	-	-	-
Control, no antifoam	-	-	-	15	25	43	-	-	-	-	-	-

(1) General Electric Company

TABLE 7

Effect of Antifoams on Dynamic Foam Height
Using Ivory Soap Based Wash Water

Antifoam	Foam Height (cm) Vs. Time Resulting From Various Dosages of Antifoam								
	100 ppm			200 ppm			300 ppm		
	1 min.	2 min.	5 min.	1 min.	2 min.	5 min.	1 min.	2 min.	5 min.
AF-93	0 0	1/2 1/2	2 2	0 1	1/2 1-1/2	1/2 3	0 -	1/2 -	1 -
AF-75	2 2	2-1/2 3	3 5	0 1	1/2 1	1 1-1/2	- -	- -	- -
AF-72 (1)	1/2 1-1/2	1 2	2 3	0 1	0 1	1/2 1-1/2	0 1	0 1	0 1-1/2
DB-110	1 1	2 2	5-1/2 5-1/2	0 1	1/2 1	1-1/2 2-1/2	1/2 -	1/2 -	1-1/2 -
Ferric Chloride	-	-	-	0	-	0	-	-	-
Control, no antifoam	27	37	48	-	-	-	-	-	-

(1) General Electric Company

III. EVALUATION OF REMOVAL AGENTS AND PROCESSES

Under Contract NAS 9-13536 - Wash Water Solids Removal System Study - we demonstrated the feasibility of chemical precipitation using ferric chloride. During the follow-up program under Contract NAS 9-14518, we continued our evaluation of removal agents using synthetic wash waters based on several soaps including Ivory and Palmeto. Under the present program we continued to screen removal agents for various wash water/soap combinations.

We have continued our precipitation work using the traditional "jar experiments". General procedures have been described in "Wash Water Solids Removal System Study", Final Report, under Contract NAS 9-13536, July 1974. Coagulation work was done with a Hach Floc Tester, essentially a gang stirrer, which consists of six magnetic stirrers connected in tandem and set to operate at 60 rpm. Coagulants were added with a dasher mixer; mixing time was 30 seconds. The slow mix time was 15 minutes at 60 rpm.

PALMETO BASED WASH WATER

A synthetic wash water was prepared as described on page 4 using 1000 ppm (soap solids) of Palmeto. Preliminary precipitation experiments using aluminum sulfate were not promising (Table 8). There was very little coagulation of the soap in the range 200-370 ppm aluminum sulfate. We evaluated lower dosages of aluminum sulfate (160-190 ppm - Table 9), but again the results were not promising. No further work was done with this combination of soap and coagulant.

NEUTROGENA BASED WASH WATER

During earlier work under Contract NAS 9-13536, we found that 160-190 ppm of ferric chloride would generally remove 60-70 percent of the soap. The removal estimate was based, however, on total dissolved solids, which later in the program was suspected of being somewhat inaccurate. To better define what is happening during the Neutrogena coagulation, we refined our analysis.

According to U. S. Patent 2,820,768 and the McDonnell Douglas Report covering OSW Contract 14-30-3062, Neutrogena Bar Soap is composed of the following:

1. Sodium soap (saponified tallow, coconut oil, and castor oil) - 35-40 percent
2. Triethanol ammonium salt of stearic acid - 35-40 percent
3. Triethanolamine)
4. Glycerine) Relative amounts not specified by manufacturer
5. Perfume)

Based on chemical composition, this represents approximately 55-60 percent minimum quantity of fatty acid (normally mixtures of C-14 to C-18 fatty acids such as stearic and palmitic).

Our chloroform/IR analysis indicated approximately 50 percent fatty acid in Neutrogena. This figure is perhaps low, but not unreasonable, assuming that the Neutrogena Corporation is operating within the claims of their patent.

We prepared fresh wash water with 1000 ppm soap. Since there had been no evidence that the electrolytes in the synthetic wash water were playing a part in the coagulation, we left them out in this case. This was done to facilitate the analysis.

Wash water samples were treated with ferric chloride at dosages of from 150-190 ppm. Promising samples (150 and 170 ppm ferric chloride) were analyzed for fatty acid and total dissolved solids. While fatty acid analysis indicated that 90-97 percent of the acid was removed by the coagulation, total dissolved solids analysis showed that only 49-54 percent of the soap had been removed. The conclusion is that while coagulation is effective in removing fatty acid, it has little or no effect on the triethanolamine, glycerine, and perfume. No further pretreatment work has been done with Neutrogena.

ML-11 BASED WASH WATER

ML-11 is another potassium fatty acid soap from Rochester Germicide Company. Our solids analysis indicated approximately 39 percent soap. Wash water prepared from this soap was treated with ferric chloride at dosages from 150-220 ppm (Table 10). IR analysis indicates that ferric chloride at a dosage of between 200 and 220 ppm will remove 93-95 percent of the soap.

Aluminum sulfate was also evaluated with ML-11 based wash water (Table 11). As with other wash water systems investigated during the program, aluminum sulfate showed no promise as a primary coagulant.

MIRANOL JEM BASED WASH WATER

Miranol JEM based water was treated with various dosages of two coagulants: ferric chloride (Table 12) and aluminum sulfate (Table 13). In both instances the results were not promising. No further work was done with this cleansing agent.

These sets of experiments conclude the chemical pretreatment portion of this effort. The overall results are discussed in Section V of this report.

TABLE 8

Chemical Precipitation with Palmeto Soap Based Wash Water

Aluminum Sulfate Series

Experiment Number	Coagulant $FeCl_3$ (ppm)	Flocculation Size and Rate (1)	Settling Rate (2)
A-2132-A	265	1	1
A-2132-B	250	1	1
A-2132-C	235	1	1
A-2132-D	220	1	1
A-2132-E	200	1	1
A-2132-F	350	1	1
A-2132-G	370	1	1

(1) Flocculation – rated on a scale of 0-5:

0 - no floc
1 - slow growth; small floc
2 - slow growth; larger floc than (1)
3 - faster growth
4 - large floc in less than 1 min.
5 - large floc almost immediately

(2) Settling – rated on a scale of 0-5:

0 - no floc
1 - no settling
2 - very little settling (less than 10%)
3 - 99-100% settled out in 20 min.
4 - 99-100% settled out in 2-3 min.
5 - settles out in less than 2 min.

TABLE 9

Chemical Precipitation with Palmeto Soap Based Wash Water
Aluminum Sulfate Series

Experiment Number	Aluminum Sulfate Dosage (ppm)	Floccula-tion Size and Rate	Settling Rate
A-3341-D-2	160	2	1 (1)
A-3341-C-2	170	2	1 (1)
A-3341-B-2	180	2	1 (1)
A-3341-A-2	190	2	1 (1)

(1) Filtrate was cloudy

TABLE 10

Chemical Precipitation with ML-11 Soap
Based Wash Water

Ferric Chloride Series

Experiment Number	Coagulant $FeCl_3$ (ppm)	Floccula-tion Size and Rate	Settling Rate	Residual Soap Content (ppm)	Percent Soap Removed
A-2136-A	160	0	0	-	-
A-2136-B	170	0	0	-	-
A-2136-C	180	5	4	-	-
A-2136-D	190	5	4	-	-
A-2136-E	200	5	4	67	93.3
A-2136-G	205	5	3	56/63	94.4/93.7
A-2136-H	210	5	3	57/ -	95.4/ -
A-2136-I	220	5	3	48/53	95.2/94.7

TABLE 11

Chemical Precipitation with ML-11 Soap Based Wash Water

Aluminum Sulfate Series

Experiment Number	Aluminum Sulfate Dosage (ppm)	Floccula-tion Size and Rate	Settling Rate
A-2139-A	160	0	0 (1)
A-2139-B	180	0	0 (1)
A-2139-C	200	1	0 (1)
A-2139-D	220	2	1 (1)
A-2139-E	240	2	1 (1)
A-2139-F	260	3	2 (1)

(1) Filtrate was cloudy

TABLE 12

Chemical Precipitation with Miranol JEM Soap Based Wash Water

Ferric Chloride Series

Experiment Number	Ferric Chloride Dosage (ppm)	Floccula-tion Size and Rate	Settling Rate
A-3340-A-1	120	0	0
A-3340-B-1	140	0	0
A-3340-C-1	160	0	0
A-3340-D-1	180	0	0
A-3340-E-1	200	0	0
A-3340-F-1	220	0	0

TABLE 13

Chemical Precipitation with Miranol JEM Soap Based Wash Water

Aluminum Sulfate Series

Experiment Number	Aluminum Sulfate Dosage (ppm)	Floccula-tion Size and Rate	Settling Rate
A-3340-A-2	120	0	0
A-3340-B-2	140	0	0
A-3340-C-2	160	0	0
A-3340-D-2	180	0	0
A-3340-E-2	200	0	0
A-3340-F-2	220	0	0

IV. DETERMINATION OF THE EFFECT OF ANTIFOAMS ON SOAP REMOVAL

There was some concern at the beginning of the program that the use of antifoam agent with wash water would interfere with chemical precipitation of the soap. To determine the effect, if any, we mixed promising antifoams with synthetic wash water, ran chemical precipitation, and analyzed for residual soap.

In our preliminary work under Contract NAS 9-14518, we found that 100 ppm of DB-110 had no adverse effect on the soap removal from an Ivory based wash water; and neither DB-110 nor SWS-211 - both at the 250 ppm level - had an adverse effect on removal with a Palmeto based wash water.

During this program we determined the effect of other antifoams in combination with Ivory and Palmeto as well as ML-11. When 300 ppm of AF-75 was added to Palmeto based wash water there was no significant effect on the degree of soap removal; but as has been evident in other cases, a slightly larger dosage of coagulant was required for effective soap removal (Table 14).

Antifoam AF-93 at a level of 200 ppm in ML-11 based wash water had a detrimental effect on the soap removal (Table 15). Even with ferric chloride dosages as high as 260 ppm, the soap removal was unsatisfactory.

The presence of 200 ppm of SWS-211 had no adverse effect on soap removal from an ML-11 based wash water, however (Table 16). Ferric chloride dosages of from 210 to 220 ppm were sufficient to remove 93-94 percent of the soap from the silicone-containing wash water.

The removal performance was also satisfactory in the presence of 200 ppm of AF-75 antifoam; a dosage of 250 ppm ferric chloride was sufficient to remove almost 96 percent of the soap from an ML-11 based wash water (Table 17).

The effect of antifoam on chemical precipitation was also determined for Ivory soap based wash water. In the presence of 200 ppm of DB-110

antifoam, a dosage of 180 ppm ferric chloride removed over 97 percent of the Ivory soap from the wash water (Table 18).

The effect of AF-75 on removal was also negligible; a dosage of 180 ppm ferric chloride precipitated almost 94 percent of the Ivory soap from the wash water (Table 19).

Both antifoams AF-93 and AF-72 had a detrimental effect on soap removal when used in an Ivory based wash water. Ferric chloride dosages as high as 260 ppm were ineffective in removing the soap (Tables 20 and 21).

In general, most of the silicone antifoams are compatible with the soap removal procedure, the two exceptions being: AF-93 when used with Ivory or ML-11, and AF-72 when used with Ivory.

TABLE 14

Effect of AF-75[1] Antifoam on Chemical Precipitation of Palmeto Soap Based Wash Water

Experiment Number	Ferric Chloride Dosage (ppm)	Floccula-tion Size and Rate	Settling Rate	Actual Soap Content of Filtrate (ppm)	Percent Soap Removed
A-3341-A	180	5	4	-	-
A-3341-B	190	5	4	-	-
A-3341-C	200	5	4	69/73	93.1/92.7
A-3341-D	210	5	4	83/86	91.7/91.4

(1) 300 ppm active solids

TABLE 15

Effect of AF-93[1] Antifoam on Chemical Precipitation of ML-11 Soap Based Wash Water

Experiment Number	Ferric Chloride Dosage (ppm)	Floccula-tion Size and Rate	Settling Rate
A-3342-E-1	170	1	2 [2]
A-3342-F-1	180	2	2 [2]
A-3342-G-1	190	3 - 4	2 [2]
A-3342-A-1	200	4	2 [2]
A-3342-B-1	210	4	2 [2]
A-3342-C-1	220	4	2 [2]
A-3342-D-1	230	4	2 [2]
A-3347-A-1	240	1	2
A-3347-B-1	250	1	2
A-3347-C-1	260	1	2

(1) 200 ppm active solids

(2) Filtrate was cloudy

TABLE 16

Effect of SWS-211(1) Antifoam on Chemical Precipitation of ML-11 Soap Based Wash Water

Experiment Number	Ferric Chloride Dosage (ppm)	Floccula-tion Size and Rate	Settling Rate	Actual Soap Content of Filtrate (ppm)	Percent Soap Removed
A-3343-A-1	190	4	3	-	-
A-3343-B-1	200	4	3	-	-
A-3343-C-1	210	4	3	61	93.9
A-3343-D-1	220	4	4	65/69	93.5/93.1

(1) 200 ppm active solids

TABLE 17

Effect of AF-75[1] Antifoam on Chemical Precipitation of ML-11 Soap Based Wash Water

Experiment Number	Ferric Chloride Dosage (ppm)	Floccula-tion Size and Rate	Settling Rate	Actual Soap Content of Filtrate (ppm)	Percent Soap Removed
A-3343-E	170	0	0	-	-
A-3343-F	180	1	1	-	-
A-3343-G	190	5	2	-	-
A-3342-A-2	200	5	2	-	-
A-3342-B-2	210	5	2	-	-
A-3342-C-2	220	5	3	-	-
A-3342-D-2	230	5	3	-	-
A-3347-A-2	240	5	4	-	-
A-3347-B-2	250	5	4	41	95.9
A-3347-C-2	260	5	4	-	-

(1) 200 ppm active solids

TABLE 18

Effect of DB-110[1] Antifoam on Chemical Precipitation of Ivory Soap Based Wash Water

Experiment Number	Ferric Chloride Dosage (ppm)	Floccula-tion Size and Rate	Settling Rate	Actual Soap Content of Filtrate (ppm)	Percent Soap Removed
A-3346-A-1	180	5	3	25	97.5
A-3346-B-1	200	5	3	-	-
A-3346-C-1	220	5	3	-	-
A-3346-D-1	240	5	3	-	-

(1) 200 ppm active solids

TABLE 19

Effect of AF-75[1] Antifoam on Chemical Precipitation of Ivory Soap Based Wash Water

Experiment Number	Ferric Chloride Dosage (ppm)	Floccula-tion Size and Rate	Settling Rate	Actual Soap Content of Filtrate (ppm)	Percent Soap Removed
A-3343-A-2	180	4	3	62	93.8
A-3343-B-2	200	4	3	-	-
A-3343-C-2	220	4	3	-	-
A-3343-D-2	240	4	3	-	-

(1) 200 ppm active solids

TABLE 20

Effect of AF-72[1] Antifoam on Chemical Precipitation of Ivory Soap Based Wash Water

Experiment Number	Ferric Chloride Dosage (ppm)	Floccula-tion Size and Rate	Settling Rate
A-3344-A-1	170	4	3 [2]
A-3344-B-1	180	4	3 [2]
A-3344-C-1	190	4	3 [2]
A-3344-D-1	200	4	3 [2]
A-3345-A-1	220	4	2 [2]
A-3345-B-1	240	4	2 [2]
A-3345-C-1	260	4	2 [2]

(1) 200 ppm active solids

(2) Filtrate was cloudy

TABLE 21

Effect of AF-93[1] Antifoam on Chemical Precipitation of Ivory Soap Based Wash Water

Experiment Number	Ferric Chloride Dosage (ppm)	Floccula-tion Size and Rate	Settling Rate
A-3344-A-2	170	3	2 (2)
A-3344-B-2	180	3	2 (2)
A-3344-C-2	190	3	2 (2)
A-3344-D-2	200	3	2 (2)
A-3345-D-1	220	2	2 (2)
A-3345-E-1	240	2	2 (2)
A-3345-F-1	260	2	2 (2)

(1) 200 ppm active solids

(2) Cloudy filtrate

V. SOAP AND ANTIFOAM SELECTION

SOAP SELECTION

A summary of the performance of wash waters based on various cleansing agents used throughout our study has been presented in Table 22, which indicates the amount of ferric chloride required for at least 90 percent soap removal, the quantity of antifoam necessary to defoam the given wash water, and the effect of the antifoam, if any, on the soap removal. The precipitation technique appears to work satisfactorily only with fatty acid soaps such as Ivory, Palmeto, and ML-11. The synthetics such as Neutrogena and Miranol JEM are not removed by the coagulants.

As a group, the silicone antifoams are the most effective and are essentially identical in their performance with any given cleansing agent. With the exception of AF-72 and AF-93, the antifoams do not interfere with the soap removal.

In order to keep the options open as to the physical form of the soap to be used, we recommended both a liquid and a bar soap. Unfortunately, only one bar soap gave satisfactory removal performance: that was Ivory. This soap can be defoamed with either AF-75 or DB-110, neither of which has a detrimental effect on the soap removal.

There are two liquid soaps which gave good removal performance, but ML-11 has certain advantages over Palmeto. ML-11 is supplied as a 38 percent solution, twice as concentrated as the Palmeto. The use of ML-11 for space flight would minimize space and weight requirements for soap storage.

Although ML-11 requires slightly larger dosages of ferric chloride for precipitation in the presence of antifoam (210 to 250 ppm versus 190 to 210 ppm), the antifoam dosage required is only one third of that required for Palmeto.

ANTIFOAM SELECTION

The antifoams to be used will be DB-110 with Ivory soap and SWS-211 with ML-11. In both cases these materials gave the best defoaming at the lowest dosage while permitting the highest degree of soap removal.

In the third and fourth quarters of the program, we conducted studies to define operating parameters, using both Ivory and ML-11 soaps. All studies were conducted in the presence of the antifoams of choice (see the following Section VI - Optimization of Subsystem Parameters).

TABLE 22

Matrix Chart

Comparative Performance of Wash Waters Based on Various Personal Cleansing Agents

Soap	Optimum Ferric Chloride Dosage		Promising Antifoams			Effect of Antifoam on Soap Removal		
	ppm (Removal Efficiency)	Reference Number	Material	Dosage (ppm)	Reference Number	Effect	$FeCl_3$ Dosage (ppm)	Reference Number
Palmeto	175-180 (92-95%)	A-3337	AF-75	300	A-2140	Negligible	200-210	A-3341
			SWS-211	300	A-2140	Negligible	200-210	A-3338
			DB-110	300	A-2140	Negligible	190	A-3337
Ivory	170-185 (95-97%)	A-2114	AF-93	100-200	A-2142	Destroys Removal	-	A-3344, -5
			AF-75	200	A-2142	Negligible	180	A-3343
			AF-72	200	A-2142	Destroys Removal	-	A-3344, -5
			DB-110	200	A-2142	Negligible	180	A-3346
Neutrogena	Ineffective (approx. 50%)	A-2137	NA (1,2)	NA	A-2143	NA (1)	NA	NA
ML-11	200-220 (93-95%)	A-2136	AF-93	100	A-2141	Destroys Removal	-	A-3342, 47
			AF-75	200	A-2141	Negligible	250	A-3347
			SWS-211	100	A-2141	Negligible	210-220	A-3343
Miranol JEM	Ineffective	A-3340	AF-75	50	A-2143	NA	-	-
			DB-110	50	A-2143	NA	-	-
			Colloid 680	200	A-2143	NA	-	-

(1) NA - Not Applicable

(2) Neutrogena-based wash water alone gave negligible foam

VI. OPTIMIZATION OF SUBSYSTEM PARAMETERS

Under contract NAS 9-14518, and during the first two quarters of the present program we investigated soap removal agents and antifoams for various candidate personal cleansing agents. The culmination of this work was the selection of two soaps, one liquid and one bar soap, and two antifoam agents for further study. During the last two quarters our efforts were directed toward optimizing the subsystem parameters using both of the candidate soaps and the antifoams.

The two soaps selected were Ivory bar soap and ML-11 liquid soap. To wash waters prepared from these soaps, we added DB-110 and SWS-211 silicone antifoams, respectively.

REPRODUCIBILITY

One important design consideration is the reproducibility of the removal procedure. To investigate this we conducted identical coagulation/flocculation jar experiments in triplicate using identical ferric chloride dosages for each jar; the evaluations were conducted on synthetic wash water containing 0.10 percent soap solids. The experiments were conducted using a gang stirrer and dasher mixer as previously described. The results for both Ivory Soap and ML-11 are summarized in Table 23.

Within the limits of accuracy of the analysis procedure, the removal technique is reproducible for both soaps; reproducibility should present no problem in the design and operation of a removal system based on this concept.

EFFECT OF SOAP CONCENTRATION IN THE WASH WATER ON THE REMOVAL

To determine the effect of concentration, we prepared synthetic wash waters from both candidate soaps at concentrations of 0.05 percent, 0.10 percent, and 0.25 percent. Coagulation and flocculation studies were again

conducted using the gang stirrer. The ferric chloride dosages for each jar were adjusted in proportion to the soap concentration. At each soap concentration we investigated several ferric chloride dosages over a narrow range in the vicinity of what was estimated to be the "optimum" dosage. Promising samples were filtered and analyzed for residual soap using the previously described carbon tetrachloride extraction/IR technique.

The results of these investigations are presented in Tables 24 and 25 for the two soaps. In both cases the residual soap content in the filtrate of the promising samples increased with increasing concentration of soap in the synthetic wash water feed. The increase was not proportional, however, and as a result the percent soap removed tended to increase with increasing soap content of the wash water feed.

The variations in removal are not significant and in all cases the removal is in excess of 90 percent. This should present no problem in the design and operation of a pretreatment system based on this concept since the trace amount of residual soap will be removed by carbon adsorption.

EFFECT OF THE DURATION OF SLOW STIRRING ON THE DEGREE OF SOAP REMOVAL

In conducting our coagulation and flocculation studies over the course of the last two programs we have standardized on a fast mix time of 30 seconds, and a slow mix time of 15 minutes, a time commonly employed in jar water clarification studies.

In order to determine the optimum slow mix time we ran series of identical jar experiments. Soap concentration and ferric chloride dosage were kept constant. Samples were mixed for periods of 0, 2, 5, 15, 30, and 60 minutes, filtered, and analyzed for residual soap content. The results are presented in Tables 26 and 27. For slow mix periods of 0 and 2 minutes the experiments were done in duplicate to provide greater reliability.

With Ivory soap based wash water, maximum soap removal was attained with no slow mixing; with ML-11 based wash water there appears to be a fall-off in soap removal with slow mix periods of less than 5 minutes.

There is not a good explanation as to why those samples mixed for 2 minutes had poorer soap removal than those with no slow mixing. However, this discrepancy will probably be resolved when the optimum slow mix period is determined as part of the Bread Board demonstration under contract NAS 9-15369.

EFFECT OF HIGHER FERRIC CHLORIDE SOLUTION CONCENTRATION

For convenience in all of our coagulation and flocculation work we have used 1 percent solutions of all coagulants. In order to conserve weight and space during missions of long duration, however, it will be necessary to employ more concentrated solutions.

To investigate the effect of higher concentration of ferric chloride on soap removal, we employed a 10 percent solution, and dosages in the range which had already proved to be near optimum. The results are presented in Tables 28 and 29.

For Ivory soap based wash water, a dosage of 175 ppm of ferric chloride applied from a 10 percent solution removed over 98 percent of the soap. This result compares favorably with previous removal results when using 1 percent solution.

For ML-11 based wash water, a dosage in the range of 230 ppm resulted in the removal of approximately 93.5 percent of the soap, comparable with previous results using 1 percent ferric chloride solution.

EFFECT OF FILTER PORE SIZE AND OPERATING PRESSURE ON THE DEGREE OF SOAP REMOVAL, WATER FLUX, AND RATE OF FLUX DECLINE

To evaluate filtration characteristics, we employed a cartridge type pressure filtration housing, Type 1-M (AMF Cuno Division). This housing holds single cylindrical cartridges approximately 25 cm long by 6.7 cm in diameter, supplied in various pore sizes.

In order to process large quantities of water, the filter housing was mounted to the bottom flange of a 38-liter glass-lined reactor, used here as a reservoir and pressure vessel (Figure 1).

Wash water based on ML-11 soap was prepared in 15 Kg batches in the laboratory and was coagulated with ferric chloride at a dosage of 240 ppm using a laboratory stirrer. Coagulated wash water was charged to the reactor through the fill pipe at the top. Nitrogen pressure was applied to the reactor through the top, and water flow rate was controlled by the shut-off valve downstream from the filter housing. To keep the soap sludge suspended, the reactor was stirred for 30 seconds before each filtration experiment.

To measure the flow rate through the filter, samples of water were collected at the desired pressure for timed intervals. The water was weighed and volume was computed from the weight of water.

Since the final system will function on a batch basis and will operate intermittently, we followed the flow rate decline for the filters as a function of cumulative volume rather than time. The tests were terminated when the flow rate fell below approximately 0.5 liters per minute. Water aliquots were sampled occasionally for analysis to determine the residual soap content. Since the filter housing was constructed from clear plastic we were also able to observe the filtering action and note any channeling or plugging in the housing.

The filtrate was also observed for cloudiness or obvious signs of sludge.

Early microscopy work on soapy wash water coagulated with ferric chloride revealed large soap aggregates, 500 to 750 microns in diameter, with smaller fragments measuring 50 to 75 microns. Therefore, our first filtration experiment employed a nominal 50-micron pore depth filter (Micro-Klean G78L8 - AMF, Cuno Division). The flow rate versus cumulative volume data for this filter is presented in Table 30.

The 50-micron filter allowed a large flow rate - nearly 28 liters per minute at 5 psig - but failed to remove most of the sludge from the effluent, even after processing over 40 liters of water.

A closer examination of the sludge under a microscope revealed that the relatively large soap aggregates were actually composed of 5 to 20 micron particles. The aggregates appear to break apart under the relatively high

shear associated with the filtering operation, with the small particles passing through coarse filters.

Next, a nominal 10-micron pore depth filter was evaluated (Micro-Klean G78C8 - AMF, Cuno Division). The initial flow rate was high, with a fairly clear effluent for the first 10 to 12 liters. The residual soap content of the first effluent was high - 94.5 percent - but had dropped to 90.5 percent by the time 13 liters of wash water had been processed (Table 31). By the time 20 liters of water had been filtered, large quantities of sludge were coming through the filter. Because of the poor filtering, the test was terminated after a cumulative volume of 30 liters.

A 5-micron depth filter (Micro-Klean G78B3 - AMF, Cuno Division) was evaluated next at two pressures: 5 and 25 psig. At 5 psig the initial flow rate was again high, with over 94 percent of the soap being removed from the effluent (Table 32). After 16 liters of water had been treated, however, the filtrate became slightly cloudy; soap analysis indicated that the removal had dropped to less than 88 percent.

With subsequent filtering, the cartridge began to blind and the effluent cleared. By the time 25 liters of water had been recovered, the soap removal had returned to over 94 percent.

At 25 psig the 5-micron filter permitted a tremendous flow rate, in excess of 60 liters per minute. Large amounts of sludge came through the filter from the beginning of the test, which was terminated after 22 liters of water had been processed.

A 1-micron depth filter (Micro-Wynd DCCPY - AMF, Cuno Division) was evaluated at two pressures - 10 and 25 psig - and gave consistently high soap removal throughout the evaluations.

A key criteria in evaluating filters is the decline in flow rate versus cumulative volume processed. This information has been presented graphically in Figure 2, as plots of flow rate in liters per minute versus cumulative liters processed. The curves were constructed from the data in Tables 31, 32, 33, and 34.

As was expected, the filters with larger pore diameters allowed higher flow rates, both initially and at low cumulative volumes (i.e., 10 to 30 liters). Because of the relatively large quantity of suspended matter in the water, however, all the filters, regardless of pore size, blinded with suspended matter. As a result, the flow rates tended to converge and approach asymptotically some minimal flow rate. This rate corresponds to that for a "sludge cake" filter, which of course could be the same in each case, regardless of filter type.

Despite the rapid drop in flow rate for all of these filters, the rate remained at an acceptable level - approximately 500 cc per minute for a cumulative volume of greater than 60 liters. This volume of water is equivalent to the requirements for a four-man crew for hand washing for a week assuming a nominal 40 washes per day and 225 cc per wash (0.5 pound per wash).

It should be noted that at no point during the testing did the sludge collected by the filters exceed the capacity of the filter housing, although in the case of the 1-micron filter evaluated at 25 psig with 64 liters of water, the sludge had filled to the wall of the housing in the lower 1/4 of the housing.

A cursory evaluation indicated that at 5 psig the solids content of the sludge was approximately 12 percent; this is equivalent to a potential water recovery in excess of 99 percent for a pretreatment system based on coagulation and flocculation followed by pressure filtration.

To summarize the results of the filtration tests, all of the filters with the exception of the 1-micron filter are too large in pore size and permit at least some sludge to come through into the effluent. The drop in flow rate with cumulative volume is rather severe for all filters investigated. Increased pressure does not have a dramatic effect on the absolute flow rate but does permit a greater cumulative volume before an unacceptably low rate is reached (e.g., 500 cc/minute). A comparison of Tables 33 and 34 illustrates the difference. With 25 psig pressure, 50.3 liters of water was processed before a flow rate of 0.43 liters per minute was achieved, while at 10 psig only 30.1 liters was filtered before a flow rate of 0.42 liters per minute was reached.

TABLE 23

Determination of the Reproducibility of the Soap Removal Using Ferric Chloride Coagulant

Experiment Number	Flocculation Size and Rate	Settling Rate	Actual Soap Content of the Filtrate (ppm)	Percent Soap Removed
Ivory Soap Based Wash Water with: 200 ppm DB 110 Antifoam, 0.10 Percent Soap; 180 ppm Ferric Chloride Dosage				
A-3349-A	5	4	25/25	97.5/97.5
A-3349-B	5	4	25/25	97.5/97.5
A-3349-C	5	4	24	97.6
ML-11 Soap Based Wash Water with: 0.10 Percent Soap, 200 ppm SWS-211 Antifoam; 220 ppm Ferric Chloride Dosage				
A-3347-C	5	4	45/49	95.5/95.1
A-3347-B	5	4	57	94.3
A-3347-A	5	4	56/57	94.4/94.3

TABLE 24

The Effect of Soap Concentration in the Synthetic Wash Water on the Degree of Soap Removal - Ivory Soap Based Wash Water

Experiment Number	Ferric Chloride Dosage (ppm)	Floccu-lation Size and Rate	Settling Rate	Actual Soap Content of the Filtrate (ppm)	Percent Soap Removed
0.05 Percent Soap in the Wash Water					
A-2148-D	85	4	4	15/17	97.0/96.6
A-2148-E	90	4	4	16/12	96.8/97.6
0.10 Percent Soap in the Wash Water					
A-2114-L	175	5	5	37	96.3
A-2114-G	185	5	5	29	97.1
0.25 Percent Soap in the Wash Water					
A-2148-A	425	5	-	45	98.2
A-2148-B	440	5	-	39/41	98.4/98.4

TABLE 25

The Effect of Soap Concentration in the Synthetic Wash Water on the Degree of Soap Removal - ML-11 Soap Based Wash Water

Experiment Number	Ferric Chloride Dosage (ppm)	Floccu-lation Size and Rate	Settling Rate	Actual Soap Content of the Filtrate (ppm)	Percent Soap Removed
0.05 Percent Soap in the Wash Water					
A-2147-A	100	4	1	29/35	94.2/93.0
A-2147-B	105	4	1	36	92.8
0.10 Percent Soap in the Wash Water					
A-2136-H	210	5	3	57	94.3
A-2136-I	220	5	3	48/53	95.2/94.7
0.25 Percent Soap in the Wash Water					
A-2146-A	500	5	3	85/91	96.6/96.4
A-2146-B	525	5	3	72/71	97.1/97.2

TABLE 26

The Effect of Duration of Slow Stirring on the Degree of Soap Removal

Ivory Soap Based Wash Water - 0.10 Percent Soap, With
200 ppm DB-110 Antifoam, 180 ppm Ferric Chloride

Experiment Number	Duration of Slow Mixing (minutes)	Floccu-lation Size and Rate	Settling Rate	Actual Soap Content of the Filtrate (ppm)	Percent Soap Removed
A-6053-A	0	4	4	18/18	98.2/98.2
A-6053-B	0	4	4	19/19	98.1/98.1
A-6053-C	2	4	4	19/21	97.9/98.1
A-6053-D	2	4	4	19/19	98.1/98.1
A-3349-D	5	5	4	25/25	97.5/97.5
A-3349-E	15	5	4	24	97.6
A-3349-F	30	5	4	21/22	97.9/97.8
A-3349-G	60	5	4	25	97.5

TABLE 27

The Effect of Duration of Slow Stirring on the Degree of Soap Removal

ML-11 Soap Based Wash Water - 0.10 Percent Soap With
200 ppm SWS-211 Antifoam, 220 ppm Ferric Chloride Dosage

Experiment Number	Duration of Slow Mixing (minutes)	Floccula-tion Size and Rate	Settling Rate	Actual Soap Content of the Filtrate (ppm)	Percent Soap Removed
A-6062-A	0	5	-	62	93.8
A-6062-B	0	5	-	62/62	93.8/93.7
A-6062-C	2	5	-	91/83	90.9/91.7
A-6062-D	2	5	-	84/83	91.6/91.7
A-3348-A	5	5	4	45/55	95.5/94.5
A-3348-B	15	5	4	47/50	95.3/95.0
A-3348-C	30	5	4	49/48	95.1/95.2
A-3348-D	60	5	4	38/37	96.2/96.3

TABLE 28

The Effect of Ferric Chloride Solution Concentration on the Degree of Soap Removal

Ivory Soap Based Wash Water with 200 ppm DB-110 Antifoam

Experiment Number	Ferric Chloride Dosage from 10% Solution (ppm)	Floccula-tion Size and Rate	Settling Rate	Actual Soap Content of the Filtrate (ppm)	Percent Soap Removed
A-3350-A	175	5	3	16/19	98.4/98.1
A-3350-B	180	5	3	27/28	97.3/97.2
A-3350-C	185	5	3	-	-
A-3350-D	190	5	3	-	-

TABLE 29

The Effect of Ferric Chloride Solution Concentration on the Degree of Soap Removal

ML-11 Soap Based Wash Water with 200 ppm SWS-211 Antifoam

Experiment Number	Ferric Chloride Dosage from 10% Solution (ppm)	Floccula-tion Size and Rate	Settling Rate	Actual Soap Content of the Filtrate (ppm)	Percent Soap Removed
A-6062-E	210	5	4	-	-
A-6062-F	220	5	4	-	-
A-6062-G	230	5	4	64/66	93.6/93.4
A-6062-H	240	5	4	57	94.3

TABLE 30

Flow Rate Vs. Cumulative Volume for Pressure Filtration of Coagulated Wash Water Through a 50-Micron Filter at 5 psig (1)

Cumulative Volume of Water, Liters (Gallons)	Flow Rate, Liters/Min. (Gal./Min.)	Residual Soap Content (ppm)	Percent Soap Removed
9.2 (2.4)	27.6 (7.29)	(2)	-
17.7 (4.7)	25.4 (6.7)	(2)	-
28.8 (7.6)	22.3 (5.9)	(2)	-
40.5 (10.7)	23.4 (6.2)	(2)	-

(1) 0.1 Percent ML-11 soap based wash water coagulated with ferric chloride.

(2) Large quantities of soap/ferric chloride sludge came through the filter.

TABLE 31

Flow Rate Vs. Cumulative Volume for Pressure Filtration of Coagulated Wash Water Through a 10-Micron Filter at 5 psig (1)

Cumulative Volume of Water, Liters (Gallons)	Flow Rate, Liters/Min. (Gal./Min.)	Residual Soap Content (ppm)	Percent Soap Removed
7.2 (1.9)	28.8 (7.6)	55	94.5
13.3 (3.5)	24.5 (6.5)	93/97 (2)	90.7/90.3
20.9 (5.5)	15.1 (4.0)	(3)	-
25.8 (6.8)	9.9 (2.6)	(3)	-
30.3 (8.0)	9.0 (2.4)	(3)	-

(1) 0.1 Percent ML-11 soap based wash water coagulated with ferric chloride.

(2) Small quantities of soap/ferric chloride sludge came through the filter.

(3) Large quantities of soap/ferric chloride sludge came through the filter.

TABLE 32

Flow Rate Vs. Cumulative Volume for Pressure Filtration of Coagulated Wash Water Through a 5-Micron Filter at 5 psig (1)

Cumulative Volume of Water, Liters (Gallons)	Flow Rate, Liters/Min. (Gal./Min.)	Residual Soap Content (ppm)	Percent Soap Removed
6.8 (1.8)	27.2 (7.2)	57/59	94.3/94.1
11.5 (3.0)	18.7 (4.9)	-	-
16.3 (4.3)	9.7 (2.6)	120/127 (2)	88.0/87.3
20.9 (5.5)	4.5 (1.2)	-	-
24.9 (6.6)	4.0 (1.1)	55/56	94.5/94.4
31.0 (8.2)	3.1 (0.82)	-	-
36.9 (9.7)	1.5 (0.40)	-	-
41.9 (11.1)	1.0 (0.26)	-	-
48.9 (12.9)	0.7 (0.18)	-	-
55.1 (14.6)	1.0 (0.26)	-	-
57.7 (15.2)	0.5 (0.13)	54	94.6

(1) 0.1 Percent ML-11 soap based wash water coagulated with ferric chloride.

(2) Filtrate was slightly cloudy.

TABLE 33

Flow Rate Vs. Cumulative Volume for Pressure Filtration of Coagulated Wash Water Through a 1-Micron Filter at 10 psig (1)

Cumulative Volume of Water, Liters (Gallons)	Flow Rate, Liters/Min. (Gal./Min.)	Residual Soap Content (ppm)	Percent Soap Removed
4.7 (1.2)	19.0 (5.0)	42/42	95.8/95.8
7.2 (1.9)	10.0 (2.6)	-	-
9.2 (2.4)	3.8 (1.0)	-	-
12.0 (3.2)	2.8 (0.74)	-	-
16.3 (4.3)	2.1 (0.55)	39/39	96.1/96.1
21.0 (5.5)	1.6 (0.42)	-	-
24.5 (6.5)	1.1 (0.29)	-	-
27.6 (7.3)	0.61 (0.16)	-	-
30.1 (8.0)	0.42 (0.11)	-	-
33.8 (8.9)	0.41 (0.11)	43/47	95.6/95.3

(1) 0.1 Percent ML-11 soap based wash water coagulated with ferric chloride.

TABLE 34

Flow Rate Vs. Cumulative Volume for Pressure Filtration of Coagulated Wash Water Through a 1-Micron Filter at 25 psig (1)

Cumulative Volume of Water, Liters (Gallons)	Flow Rate, Liters/Min. (Gal./Min.)	Residual Soap Content (ppm)	Percent Soap Removed
7.2 (1.9)	28.8 (7.6)	43	95.7
10.1 (2.7)	11.7 (3.1)	-	-
13.3 (3.5)	6.3 (1.7)	-	-
16.9 (4.5)	3.6 (0.95)	-	-
23.0 (6.1)	2.0 (0.53)	-	-
28.4 (7.5)	1.1 (0.29)	-	-
33.5 (8.8)	0.73 (0.19)	-	-
38.1 (10.0)	0.57 (0.15)	-	-
44.7 (11.8)	0.47 (0.12)	-	-
50.3 (13.3)	0.43 (0.11)	-	-
57.5 (15.2)	0.40 (0.11)	-	-
64.2 (17.0)	0.33 (0.09)	44	95.6

(1) 0.1 Percent ML-11 soap based wash water coagulated with ferric chloride.

FIGURE 1

Pressure Filtration Apparatus

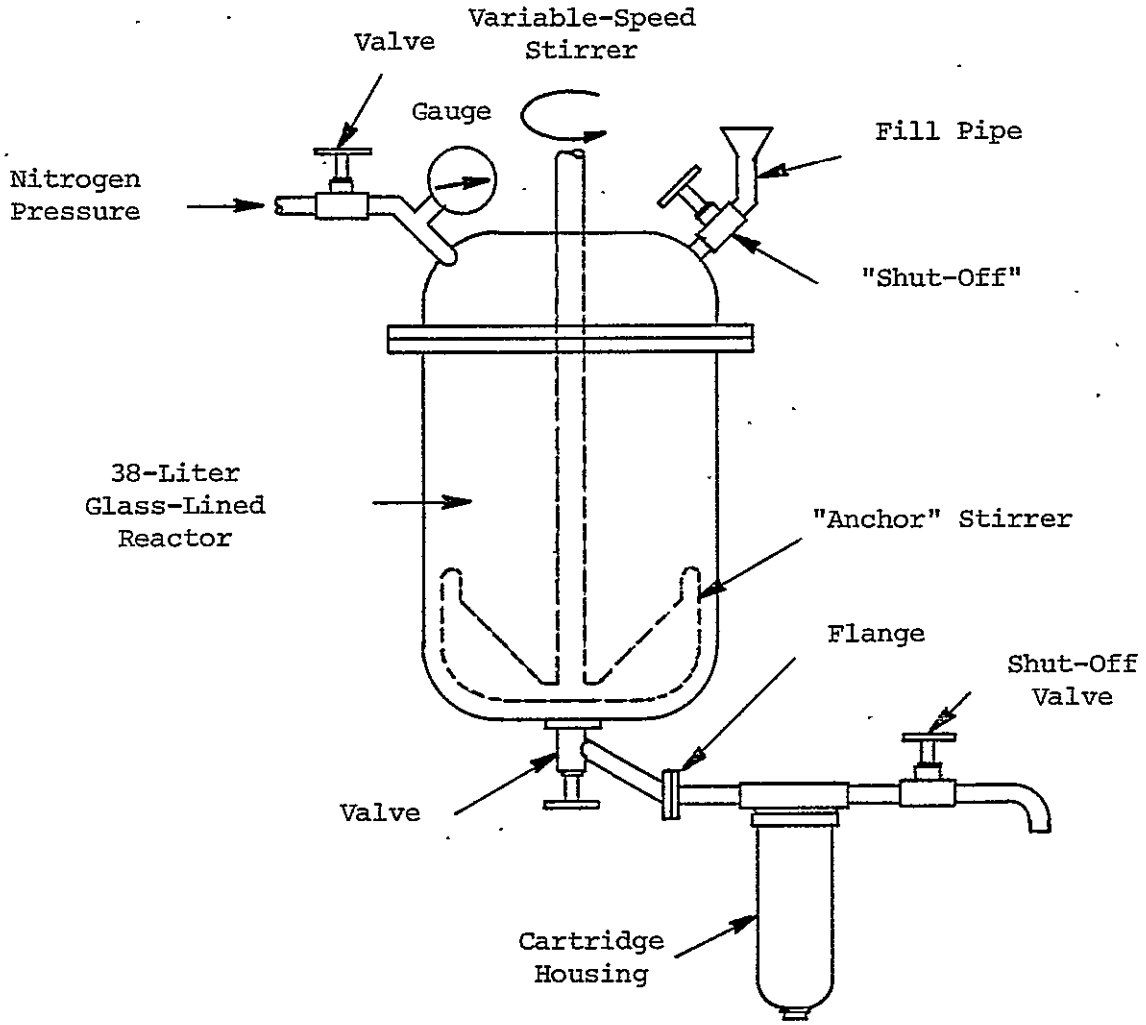

FIGURE 2

Flow Rate Vs. Cumulative Volume of Water Processed

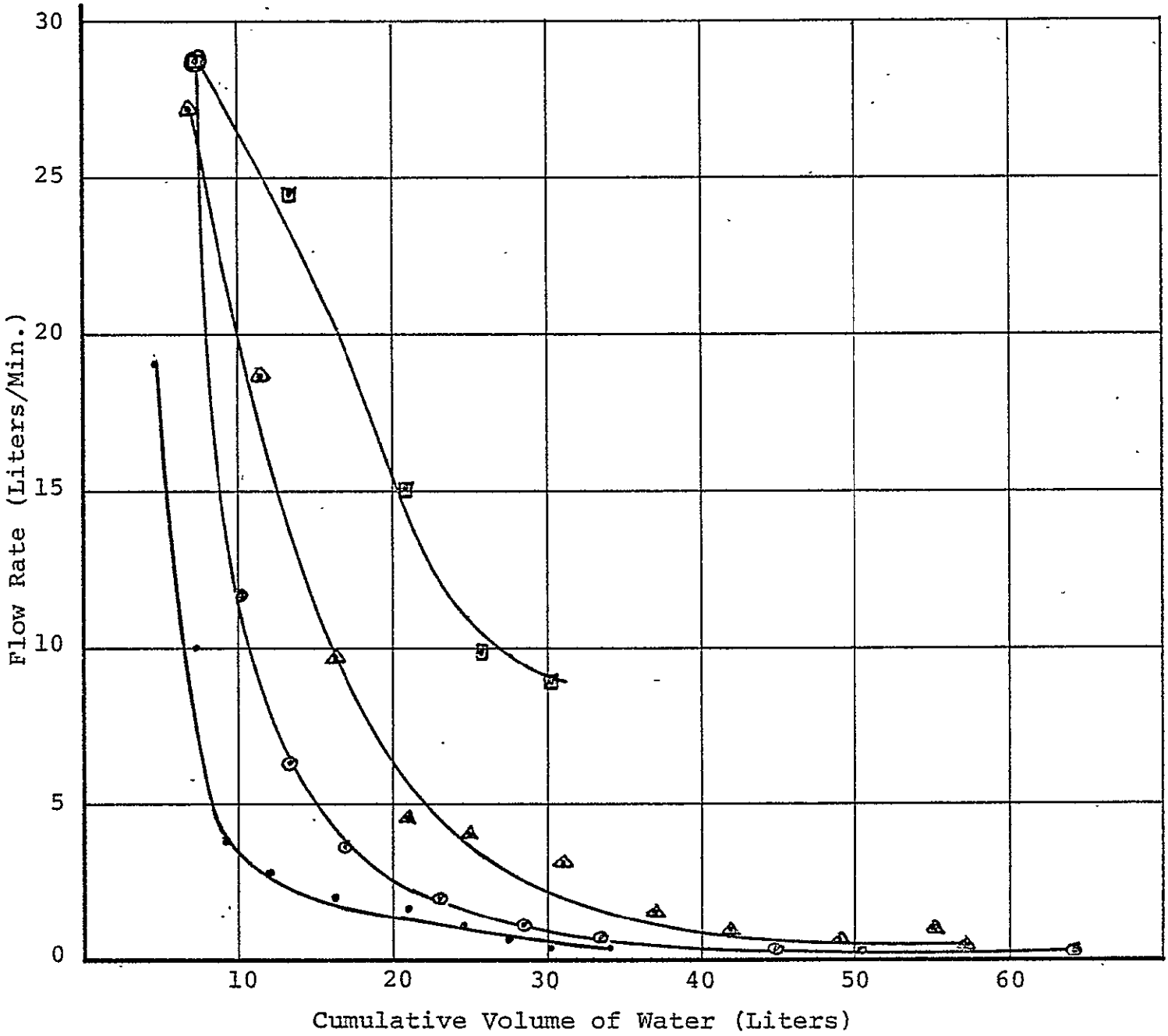

TRADE-OFF ANALYSIS

While this trade-off analysis in a strict sense applies to the present contract, it is really the culmination of three programs covering a four-year period leading up to the design and construction of a breadboard wash water renovation system. Where our analysis bears on previous work the appropriate contracts will be referenced.

The bulk of this analysis will be substantiated by the body of the final report, which has preceded this section. Again, references to pertinent sections will be made to support the analysis.

SOAPS, ANTIFOAMS, AND COAGULANTS

Numerous different cleansing agents have been evaluated as part of the three development programs. These materials can be categorized as either fatty acid soaps or synthetics, as follows:

- Synthetics:

  Miranol JEM (The Miranol Company)
  Neutrogena (Neutrogena Corporation)
  Igepon CN-42 (GAF Corporation)
  Aerosol 18 (American Cyanamid)
  Aerosol MA-80 (American Cyanamid)

- Fatty Acid Soaps:

  Olive Leaf Soap - discontinued (Rochester Germicide)
  Palmeto (Rochester Germicide)
  ML-11 (Rochester Germicide)
  Ivory Soap

The cleansing agents were selected for evaluation on the basis of their apparently good dermatological characteristics; the three main criteria for final selection of a cleansing agent were ability to be removed from wash water by chemical precipitation, ability to be defoamed using antifoam agents, and compatibility of the required antifoam agent with the chemical precipitation process.

Under contracts NAS 9-14518 and NAS 9-14965 a study was conducted to identify coagulants for the candidate soaps. These studies revealed that only the fatty acid soaps are successfully removed by chemical precipitation, while the synthetics are generally unaffected. Aluminum sulfate was surprisingly unsuccessful with the various cleansing agents, but ferric chloride has proved to be effective with all of the candidate fatty acid soaps. This agent will be used for all future work.

As part of the coagulation work, several polymeric coagulants including anionics, cationics, and nonionics were evaluated in conjunction with primary coagulants. None of these materials enhanced the soap removal and therefore will not be employed in future work.

Under contracts NAS 9-14518 and NAS 9-14965 antifoam agents were evaluated for wash waters based on each of the candidate soaps. Antifoams investigated can be categorized as follows:

Material	Manufacturer	Type
Nalco 73C44, 73C37	Nalco Chemical Company	Amides
Nalco 71-D5, 8616, 867, and 4WP126	Nalco Chemical Company	Fatty acid esters
Dow Corning DB-110	Dow Corning Corporation	Silicone
Antifoam 71, AF-72, AF-75, AF-93	General Electric Company	Silicone
SWS-211	SWS Silicones Corporation	Silicone
Foamaster, Foamaster B, VL, AP, G, and TMC	Nopco Chemical Division, Diamond-Shamrock	Proprietaries
Foamex/Pegosperse 100L	Glyco Chemical	Proprietary
Colloid 680, 681F	Colloids, Inc.	Proprietary
Nalco 121	Nalco Chemical Company	Proprietary
Ferric chloride, calcium chloride, aluminum sulfate, and magnesium sulfate		Heavy metal ions

Based on both a NASA-JSC "shake test" and a dynamic test using cascading water, the silicones as a group were far superior to any of the other types of antifoam agents.

The rationale for final soap and antifoam agent selection can be found on pages 33 and 34 of this report, and in Table 22 on page 35, which is a matrix chart comparing the soap removal performance of wash waters based on various personal cleansing agents when used in combination with the more promising antifoams.

NASA-JSC requested that the selection include one liquid and one bar soap; the choices of soap and respective antifoam agent as well as required dosage of ferric chloride for optimum soap removal are as follows:

Soap Type	Soap	Antifoam Agent[1] (dosage, ppm)		Coagulant Dosage Required (ppm Ferric Chloride)
Liquid	ML-11	SWS-211	(100)	210-220
Bar soap	Ivory	DB-110	(200)	180

(1) Assumes a wash water based on 0.1 percent soap

SOAP CONCENTRATION

In a final pretreatment system, it is possible that there would be relatively small variations in the soap concentration of the wash water to be treated.

Within reasonable limits, the percentage of soap removed from wash water is unaffected by the concentration of soap in the wash water when chemical precipitation is used - assuming that the dosage of ferric chloride is in proper proportion to the soap. The removal performance for soap concentrations in the range of from 0.05 percent to 0.25 percent, for both Ivory and ML-11 soaps, is presented on page 36 of this report, and in tables 24 and 25 on pages 43 and 44, respectively.

COAGULANT CONCENTRATION

In a final system it may be necessary to employ the coagulant in a more concentrated form than has been used in the laboratory in order to conserve weight and space. Depending on the quantities of water to be treated, the concentration may have to be as high as 10 percent.

During the current program wash water was treated with 10 percent ferric chloride. There was no adverse effect on removal, with results being essentially the same as those obtained with 1 percent ferric chloride solutions. For details see page 38 of this report, and tables 28 and 29, pages 47 and 48, respectively.

DURATION OF MIXING

In a final system, to minimize the cycle time and therefore reduce turn-around time for the equipment as well as power requirements, it would be desirable to have as short a mix time as possible after the addition of the ferric chloride coagulant.

An investigation of mixing time spanning from "no mixing" up to 60 minutes revealed that mixing for periods longer than 5 minutes does not enhance the soap removal. Mixing time of less than 5 minutes (i.e., 0 to 2 minutes) had no adverse effect on the soap removal with Ivory soap based wash water; but with ML-11 soap based wash water, the removal was somewhat reduced. The data as presented in tables 26 and 27 is not completely convincing for ML-11 based wash water, and a repeat of this investigation using a breadboard model will be required to further define the need for slow mixing.

SOAP REMOVAL

In order to remove the coagulated soap from the wash water, it will be necessary to use some form of filtration. There are numerous types of filtration systems for industrial use - including rotary vacuum, plate-and-frame pressure filtration, batch leaf, regenerable or backflushing, or in-line cartridge filtration using either pleated membrane or depth filter type cylindrical cartridges. Many of these systems - such as rotary vacuum,

plate-and-frame, and batch leaf filters - have large space weight and energy requirements and are overdesigned for the present application.

Regenerable filters are attractive because of their low maintenance requirements, but because of the relatively high level of suspended matter in the coagulated wash water, large quantities of water would have to be used for frequent backflushing.

A simplified pressure filter or in-line cartridge filter is the most promising for the present application. Coagulation of an Olive Leaf Soap based wash water with 170 ppm ferric chloride followed by pressure filtration using an asbestos pad depth filter removed in excess of 95 percent of the soap from the water in investigations conducted under contract NAS 9-13536.

THE EFFECT OF PORE SIZE ON REMOVAL

Investigations were conducted on depth type filter cartridges employing media with nominal pores in the range of from 50 down to 1 micron. Soap analysis and visual results indicate that only the 1-micron filter provides for a consistently high level of soap sludge removal when using both high and low pressures. Filtration work has been discussed on pages 38 through 41.

WATER FLOW RATE AND FLOW RATE DECLINE

The initial flow rates for the various pore sized filter cartridges depend, as might be expected, on the nominal size of the pores. During filtration the rate drops off rapidly, however, as a result of blinding of the filters caused by the relatively high level of suspended matter in the coagulated wash water.

The 1-micron filters are the only ones capable of consistently removing all of the sludge and therefore are the only cartridges of interest here.

Once a cumulative volume of 30-40 liters of water has been processed with these filters, there is little difference in the flow rate between the cartridge when operated at 10 psig versus a 25 psig pressure. Increased

pressure, however, does offer the advantage of allowing a greater cumulative volume of water to be filtered before the flow rate reaches an unacceptably low level.

For a final system, a staging of pressures might be desirable, beginning with a 10-15 psig pressure and gradually increasing the pressure to 50 or 100 psig as the sludge content of the filter housing reaches near capacity. This would permit higher cumulative amounts of water to be processed before a low flow rate required a replacement of the unit.

Based on the work conducted under the present program (see pages 38 through 41, we feel that a 1-micron cartridge, when used in a pretreatment system, would be capable of processing a minimum of one week's requirement of hand wash water for a four-man crew. Rather than rely on the replacement of filter cartridges for such a pretreatment system, we envision the use of several housings in parallel, each containing a fresh cartridge. As one housing became filled, another would be valved into the system to take its place.

Housings are available which can accommodate two or three cylinderical cartridges stacked end to end. Based on our present work, we would estimate that a cluster of eight housings, each containing three cartridges, would be able to process all of the pretreated hand wash water generated by a four-man crew during a six-month mission.

THE CONCEPT FOR A PRETREATMENT SYSTEM

We envision that a typical pretreatment system based on the chemical precipitation concept would be as follows:

Water from a hand washing station would be picked up and passed through a prefilter to remove hair, lint, and other suspended matter. The water sould comprise either Ivory or ML-11 fatty acid soap in a concentration of from 0.05 - 0.25 percent as well as dissolved salts at approximately 150 ppm consisting primarily of the sodium salts of chloride and sulfate.

Following the prefilter, antifoam would be added to the water at the appropriate dosage (e.g., 200 ppm for a 0.1 percent solution of Ivory soap)

using a metering pump. The antifoams, DB-110 with Ivory soap, and SWS-211 with ML-11, would be dispensed from a nominal 4 percent dispersion in water. This concentration provides for a reasonably stable dispersion and control of the dosage amount in the range of interest.

Once the antifoam has been added, the water would enter a centrifugal liquid/air separator. This separator would likely be a small rotating vane type separator such as the one developed by Hamilton-Standard for the Sky Lab program for urine separation. The antifoam in the water should aid in preventing excessive foaming in the separator.

Water exiting from the separator would be picked up by centrifugal pump, which would carry it to a mixing chamber. Prior to the mixing chamber, ferric chloride, the coagulating agent, would be added to the water from a nominal 10 percent solution - again using a metering pump. The dosage would depend on the soap being used and the concentration of that soap in the wash water, but would typically be in the range of from 100-600 ppm. The water, now dosed with ferric chloride, would enter a mixing chamber, where it would be slow-mixed at 25-50 rpm for a period of 2-5 minutes. This mixing chamber would consist of a nominal 10 cm diameter cylinder with a free-floating piston inside to allow an adjustable volume inside the cavity. At the bottom of the chamber would be an impeller to gently agitate the water.

Once the water had slow-mixed, the piston would be driven downward by gas pressure to drive the water out of the cylinder and through a depth type filter cartridge. This cartridge would be a nominal 1-micron pore size filter such as the Micro-Wynd DCCPY (AMF, Cuno Division) or suitable substitute, inside a conventional cartridge housing such as AMF-Cuno Unit Type 1B.

This would comprise the entire pretreatment system; water from this unit might be further processed by multifiltration through a carbon adsorber and deionizer, through a reverse-osmosis unit, through an electrodialysis apparatus or some other combination of the above to remove traces of organics and electrolytes.